# Atomic Force Microscopy of Biomimetic Systems

**Dissertation**

zur Erlangung des Grades

“Doktor der Naturwissenschaften”


am Fachbereich

Chemie, Pharmazie und Geowissenschaften

der Johannes Gutenberg-Universität Mainz

vorgelegt von

**Matthias Janke**

geboren in Backnang


Mainz, 2008

Dekan: Prof. [redacted]

Erster Gutachter: [redacted]

Zweiter Gutachter: [redacted]

Tag der mündlichen Prüfung: 08.05.2008

# Abstract

This thesis was driven by the ambition to create suitable model systems that mimic complex processes in nature, like intramolecular transitions, such as unfolding and refolding of proteins, or intermolecular interactions between different cell components. Novel biophysical approaches were adopted by employing atomic force microscopy (AFM) as the main measurement technique due to its broad diversity. Thus, high-resolution imaging, adhesion measurements, and single-molecule force distance experiments were performed on the verge of the instrumental capabilities.

As first objective, the interaction between plasma membrane and cytoskeleton, mediated by the linker protein ezrin, was pursued. Therefore, the adsorption process and the lateral organization of ezrin on $PIP_2$ containing solid-supported membranes were characterized and quantified as a fundament for the establishment of a biomimetic model system. As second component of the model system, actin filaments were coated on functionalized colloidal probes attached on cantilevers, serving as sensor elements. The zealous endeavor of creating this complex biomimetic system was rewarded by successful investigation of the activation process of ezrin. As a result, it can be stated that ezrin is activated by solely binding to $PIP_2$ without any further stimulating agents. Additional cofactors may stabilize and prolong the active conformation but are not essentially required for triggering ezrin's transformation into an active conformation.

In the second project, single-molecule force distance experiments were performed on bis-loop tetra-urea calix[4]arene-catenanes with different loading rates (increase in force per second). These macromolecules were specifically designed to investigate the rupture and rejoining mechanism of hydrogen bonds under external load. The entangled loops of capsule-like molecules locked the unbound state of intramolecular hydrogen bonds mechanically, rendering a rebinding observable on the experimental time scale. In conjunction with Molecular Dynamics simulations, a three-well potential of the bond rupture process was established and all kinetically relevant parameters of the experiments were determined by means of Monte Carlo simulations and stochastic modeling.

In summary, it can be stated that atomic force microscopy is an invaluable tool to scrutinize relevant processes in nature, such as investigating activation mechanisms in proteins, as shown by analysis of the interaction between F-actin and ezrin, as well as exploring fundamental properties of single hydrogen bonds that are of paramount interest for the complete understanding of complex supramolecular structures.

# TABLE OF CONTENTS

# 1 INTRODUCTION

The creation and understanding of diminutive sophisticated structures come more and more into spotlight of modern research, resulting in the new discipline of nanotechnology that comprises researchers from all fields of science. However, nanotechnology is not a novel conception; it worked quite well in nature for a long time, giving evidence that complex machines on the nanometer scale, e.g. ATPase or flagella, are feasible.[1] Hence, artificial replications of biological concepts are envisioned in many scientific branches. For example, in materials science, the development of self-cleaning surfaces was inspired by the lotus plant that is in Buddhism a symbol for purity. The "lotus-effect", or in other words "superhydrophobicity", is based on a minimized contact area between water droplets and surface due to hydrophobic nanospikes that lead to rolling rather than sliding off the surface and thus absorbing dust particles.[2]

Although the "lotus effect" is a famous mimic of nature's nanotech toolbox, it is merely one out of many examples from biomimetic engineering.

Two strategies are pursued in the field of synthetic biology. In chemistry, biological structures and molecules are used as archetypes for entirely artificial, supramolecular structures with well-defined architectures that yield in chemo-, regio- and stereoselective utilizations. By this means, e.g., artificial catalysts, displaying the same functions as biological enzymes but with a higher stability and accessibility, are highly demanded for industrial applications.[3]

Besides organic synthesis approaches, efforts are made to embed components of natural systems in artificial environments. Recently, Kumar *et al.* investigated the incorporation of aquaporin Z (AqpZ) into the walls of self-assembled polymer vesicles made of amphiphilic triblock copolymers.[4] Such a protein–polymer hybrid membrane with specified levels of water permeability may be useful in water desalting and purification as well as drug delivery applications.

[1] Leifson (1951); Noji *et al.* (1997); Silverman and Simon (1974)
[2] Cheng and Rodak (2005)
[3] Alfonso and Gotor (2004)
[4] Kumar *et al.* (2007)

However, the ambitious enterprise of biomimetic engineering requires a deeper knowledge of molecular biophysics, because only after complete identification and comprehension of the mechanisms in biological processes, a biomimetic model can be implemented in modern applications. Nevertheless, exploiting detailed features of complex natural systems, like living cells, remains a challenge in actual research that is engaged in different strategies. Quantitative, systematic and reliable studies of individual biological phenomena are often only palpable by usage of simplified systems that focus exclusively on the subject of investigation, but with limited degree of complexity that still permits an authentic representation of biological activity.[5] Hence, in actual research there is an ongoing demand for new and innovative biomimetic model systems enabling the investigation and understanding of fundamental processes in biology.

Therefore, this work was driven by the ambition to create suitable model systems to investigate detailed mechanisms ranging from a single molecular level to adhesion processes on a meso- to microscopic length scale. One approach focused on intermolecular interactions between different natural cell components, while the other aimed at intramolecular transitions, using an entirely artificial system (see figure 1). Atomic force microscopy was employed as the main measurement technique, backed up by ellipsometry, epifluorescence microscopy and quartz crystal microbalance measurements and supported by Molecular Dynamics and Monte Carlo simulations.

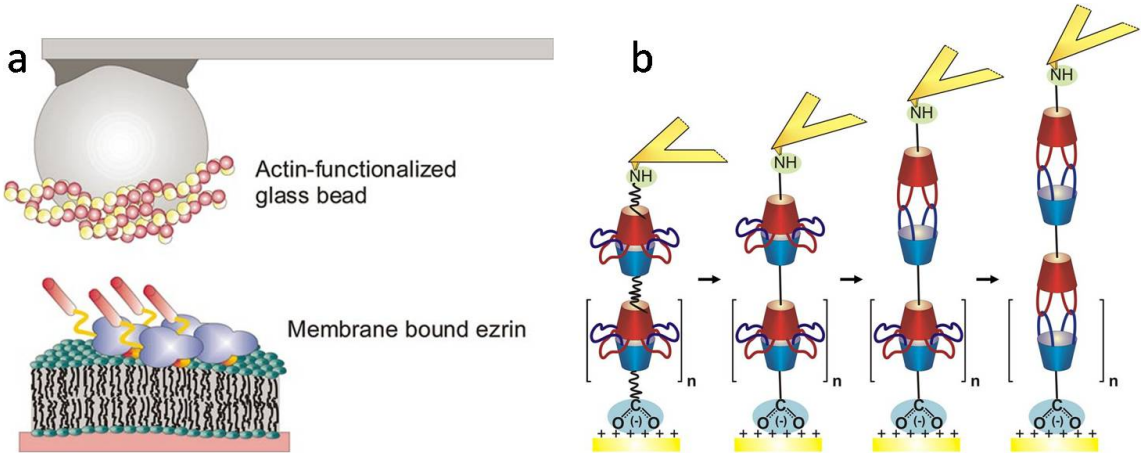


**Figure 1: a)** Schematics showing colloidal spheres equipped with an artificial cytoskeleton composed of firmly attached F-actin filaments for investigation of the interaction with ezrin coated solid-supported membranes. **b)** Schematic representation of single-molecule force spectroscopy on oligomerized calixarene-catenanes.

[5] Doktycz and Simpson (2007); Simpson (2006)

The overall objectives of this work can be summarized as follows:

- Realization and characterization of a suitable hybrid model system that enables the examination of the interaction between the plasma membrane and the actin cytoskeleton.
- Quantification and correlation of the adhesion strength between F-actin functionalized cantilevers and ezrin coated solid-supported bilayers, in order to elucidate the activation of ezrin by $PIP_2$ recognition.
- Characterization of the self-assembly properties of calixarenes via atomic force microscopy
- Investigation of reversible hydrogen bond ruptures inside entangled, oligomerized calixarene-catenanes via force spectroscopy.

# 2 ATOMIC FORCE MICROSCOPY

In the world of science, every day new questions arise that demand new, innovative approaches. By inventing the scanning tunneling microscope (STM) in 1982,[6] Binnig and Rohrer created a novel tool of great importance for the field of surface sciences. In 1986, they received the Nobel Prize for this innovation in physics and in the same year Binnig developed together with Gerber and Quate its most popular offspring, the atomic force microscope (AFM).[7] This rather young technique covers today a huge variety of applications, summarized as topographic imaging, nanolithography,[8] and single molecule force spectroscopy. In this work, AFM was used for imaging and force distance experiments in liquids (mesitylene and aqueous buffer solutions). Due to the enormous versatility of this measurement technique only some important issues concerning particularly the performed experiments are highlighted in this chapter.

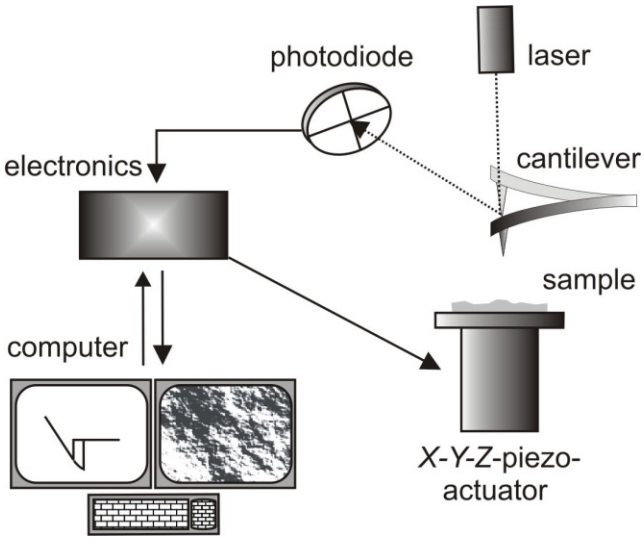


**Figure 2:** Schematic representation of the setup of an atomic force microscope.[9] By focusing a laser beam on the backside of a cantilever and measuring its reflection with a segmented photodiode, the deflection of the cantilever due to the interaction of the tip with the sample can be obtained and used either as a feedback signal for imaging the sample (at constant force) or by its transformation as the recording signal of force distance curves. The movement of the tip or sample is achieved by X-Y-Z piezoelectric actuators that are controlled by an electronic feedback amplifier. In case of dynamic AFM modes, the cantilever oscillation is driven by an additional vibrating piezo-device and a Lock-In amplifier is used to extract the oscillation amplitude and phase shift of the oscillating cantilever.

[6] Binnig and Rohrer (1987)
[7] Binnig *et al.* (1986)
[8] Tang *et al.* (2004)
[9] Adapted from Janshoff *et al.* (2000)

## 2.1 Imaging surfaces

AFM, or with respect to the imaging operation alternatively called scanning force microscopy (SFM), enables a rather simple access to topographical high-resolution images of non-conducting samples under different conditions. Sometimes even a higher spatial resolution than in scanning tunneling microscopy (STM) can be obtained by frequency modulation (FM, or also called non-contact mode) in ultra high vacuum (UHV).[10] Yet, AFM did not become famous due to measurements in UHV, in fact, its biological applications like imaging of living cells or single molecules with high resolution can be claimed as the reason for the tremendous upsurge of this technique.[11] The two established operation modes in aqueous solution are:

***Contact mode.*** As in the original AFM setup, the probing tip is in steady mechanical contact with the sample and is scanning with a rather fast rate of 2 - 4 Hz (typical edge length of 2 – 40 μm), compared to the tapping mode (1 – 2 Hz).
During the imaging process, the applied force (set point) can slowly be decreased until the measurement is conducted in the attractive interaction regime. Due to the minimized nominal forces that are applied on the sample, the topographic information is more reliable compared to the tapping mode. Nevertheless, the height measurements of biological samples can be influenced by electrostatic interactions between tip and sample.[12] In addition, the fast scan direction should be perpendicular to the main symmetry axis of the cantilever (scan angle of 90°), otherwise the vertical and lateral forces are coupled, resulting in a contrast difference between trace and retrace.[13] One main disadvantage of the contact mode is that soft or poorly immobilized samples can be damaged or pushed away due to high lateral forces during scanning, leading to artifacts and a contamination of the tip.[14]

[10] Giessibl (2005); Hembacher *et al.* (2004)
[11] LeGrimellec *et al.* (1998); Müller *et al.* (1999)
[12] Müller and Engel (1997)
[13] Paredes *et al.* (2000)
[14] Benoit *et al.* (1997)

*Tapping mode (intermittent contact mode or AC mode).* In order to decrease the lateral forces between tip and sample, the cantilever is excited at or near its free resonance frequency, resulting in a minimized contact time. A change in the oscillation amplitude in proximity of the sample is used as a feedback parameter to control the vertical displacement of the cantilever. Typically, the setpoint of the amplitude is kept as close as possible (e.g. 80-90%) to the free amplitude to minimize the energy deposited on the sample. To further decrease the repulsive interaction forces between tip and sample the effective quality factor of the oscillating cantilever can be increased by employing an additional feedback circuit (including a variable phase shifter and a variable gain amplifier) that enables an active control of the damping of the dynamic system. This procedure, called Q-Control, enhances the lateral resolution only with accurately adjusted parameters; it is especially recommended for imaging in air.[15] An alternative to improve the image quality in liquids are small sized, particularly short cantilevers featuring a low thermal noise and high resonance frequency like the Bio-Levers™.[16] In liquids, the size of the cantilever has a great importance due to viscous damping that shifts the quality factor and the resonant frequency to lower values.[17] For stable imaging, a resonant frequency of at least 5 kHz is required, therefore, cantilevers longer than about 100 μm are not re commended for applying tapping mode in aqueous solutions, because the fluid mass pushes the resonant frequency too low.

Tapping mode provides not only topographical information about the sample, moreover, material properties of the surface can also be obtained by recording the phase shift between the driving piezo and the oscillating cantilever. However, variations in material properties like adhesion, elasticity and viscoelasticity cannot be quantitatively characterized due to the lack of selectivity to isolate the specific sample property responsible for the phase shift modification. In addition, parameter settings like the drive frequency and drive amplitude have an effect on the phase contrast, so that sometimes a slight change of these parameters leads to a contrast inversion. Furthermore, when operating in air large adhesion differences, caused by deviations in the thickness of the adsorbed water layer can lead to anomalies, even

[15] Holscher and Schwarz (2006); Rainer *et al.* (2001); Rodriguez and Garcia (2003)
[16] Viani *et al.* (1999)
[17] Maali *et al.* (2005)

resulting in negative heights.[18] Consequently, the interaction between tip and sample in tapping mode is rather complex and investigated both theoretically and experimentally to better understand the response of the cantilever amplitude and phase while imaging a sample.[19] Tapping mode is nowadays the most applied imaging operation mode of AFM, a good review article including theoretical analysis, applications and limitations of this technique is written by García and Pérez.[20]

[18] Van Noort *et al.* (1997)
[19] Burnham *et al.* (1997); Krüger *et al.* (1997)
[20] Garcia and Perez (2002)

## 2.2 Force distance measurements

In a force measurement the cantilever is approached vertically to the surface and retracted afterwards with a specific velocity. By recording the cantilever deflection $z_c$ and knowing its spring constant $k$, the force between the tip and sample can be obtained from Hooke's law, valid for small displacements:

$$F = k \cdot Z_c \tag{1}$$

However, the signal of the segmented photodiode has to be calibrated by dividing by the slope of the contact line (Optical Lever Sensitivity or OLS) on a hard surface in order to obtain the deflection of the cantilever in nanometers.

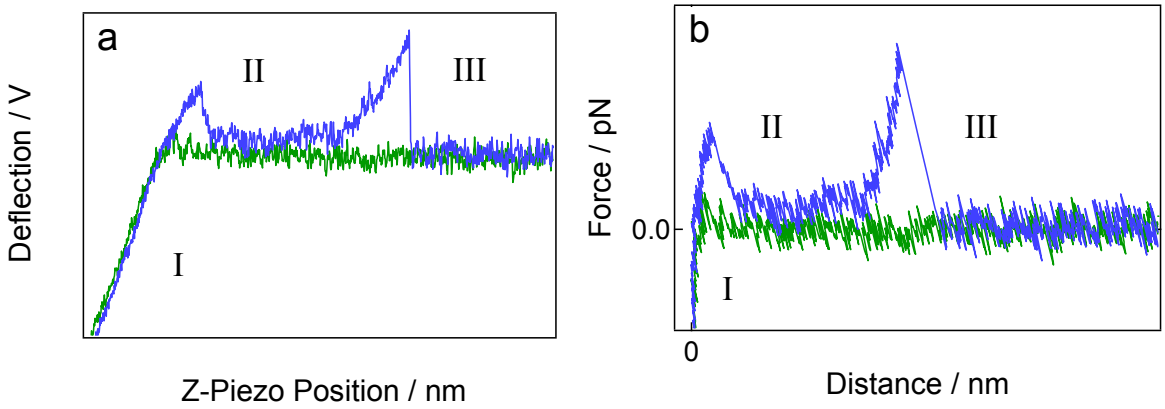


**Figure 3: a)** Cantilever-deflection versus piezo-movement curve, representing the raw data and the corresponding force versus distance curve **b)** after conversion of the photodiode signal into the force (ordinate) and the determination of the contact point on the x-coordinate. Approaching (trace) in green and retraction (retrace) in blue.

As illustrated in figure 3, force distance curves in fluids show different, characteristic regions. The contact regime (I) gives information about the young modulus of a surface in such a way that with a characterized or proper calibrated tip geometry localized elasticity measurements can be performed on soft samples like polymers or even on living cells.[21] When retracting the cantilever, frequently within the first nanometers the tip is still adhering to the surface (II) due to Van der Waals forces or electrostatic attraction between tip and surface. These forces can be summarized as non-specific interaction forces, because no specific, single molecules are involved. In air, very strong capillary forces dominate the retraction curve and preclude any further investigation. Regime (III) in the retrace curve derives typically from single

[21]Kaliappan and Cappella (2005); Radmacher *et al.* (1996); Reynaud *et al.* (2000)

macromolecules that are attached to the tip and are stretched during the retraction. While rupture forces may resemble specific molecular interactions, the shape of these curves displays the elasticity of the molecules and can be determined by fitting with polymer models from statistical mechanics to the data. However, it is often difficult to answer unmistakably whether single or multiple molecules are manipulated during pulling experiments. Sometimes histograms of the distribution of rupture forces show quantized peaks that resemble multiple molecule interactions.[22] In addition, the nonlinearity of the curves can be used as evidence for single molecule stretching, e.g. polypeptide chains exhibit a typical persistence length ($l_P$) of $0.3 - 0.4$ nm.[23] By reason that long-chain molecules of the same type but different length exhibit different elasticities, it is important to characterize single molecules by intrinsic parameters like the persistence length. In order to evaluate "self-similar" properties of force distance curves, the displacement ($x$) has to be normalized at a certain, pre-defined force level or by the contour length ($x^* = x/L$).

The surface concentration of the molecules of investigation is another variable. To increase the possibility of single molecule stretching events, the experiments have to be adjusted by adequate sample dilution and proper tip functionalization. Therefore, correct force distance experiments demand accurate sample and tip preparations. For instance, it is known that commercial cantilevers, usually stored in gel packs made of poly(di-methylsiloxane) (PDMS), are contaminated by a thin layer of silicon oil leading to a possible interference with the experiments.[24] Thus, the cantilevers have to be cleaned either by immersion in a piranha solution ($H_2SO_4/H_2O_2$, 70/30 (v/v)) for several minutes or by exposure to argon plasma or concentrated ozone gas.

***Cantilever calibration.*** An important issue is the exact knowledge of the spring constant that is given by the manufacturer as a first approximation, calculated from the material dimensions (width *w*, length *l* and thickness *t*) and properties (elastic modulus *E*).

[22] Snyder *et al.* (2007), Ratto *et al.* (2006)
[23] Rief *et al.* (1997)
[24] Viani *et al.* (1999)

For rectangular cantilevers the spring constant can be calculated as follows:

$$k_{rect} = \frac{Et^3w}{4l^3} \quad (2)$$

V-shaped cantilevers can be approximated as two rectangular cantilevers with the same dimension in parallel and roughly exhibit the doubled spring constant. However, it should be mentioned that these calculations lack in accuracy because firstly, small variations in the thickness, from coating the cantilevers, show a significant effect and secondly it is difficult to determine the young modulus of a thin layer. As a consequence, numerous methods exist for calibrating cantilever spring constants. Cleveland measured the change of the resonant frequency $\Delta\nu$ before and after adding small end masses like gold or tungsten particles to obtain an accurate spring constant from the slope of the linear calibration plot (added mass versus $2\pi\nu^{-1}$).[25] Sader used the quality factor $Q$ from a thermal noise spectrum and the resonant frequency to obtain the spring constant. The Sader method is more convenient and relies only on the knowledge of width and length, not on the thickness or elasticity of the cantilever; unfortunately, it is restricted to rectangular cantilevers and shows large deviations. Today, most of the commercial AFMs enable the determination of the spring constant by the thermal tune method, first proposed by Hutter and Bechhoefer and later improved by Butt and Jaschke.[26] By using the equipartition theorem, the thermal energy can be related to thermal fluctuations of the cantilever, assuming the behavior as a harmonic oscillator (1 degree of freedom):

$$\frac{1}{2}k_c\langle\Delta Z_c^2\rangle = \frac{1}{2}k_BT \;\Rightarrow\; k_c = \frac{k_BT}{\langle\Delta Z_c^2\rangle} \Rightarrow\; \beta\frac{k_BT}{\langle\Delta Z_c^2\rangle} \quad (3)$$

The spring constant $k_c$ can be obtained by measuring the mean square deflection $\langle\Delta Z_c^2\rangle$ over the whole frequency range, achieved by an integration of a thermal noise power spectrum. Generally, the lowest eigenmode of the cantilever bending motion is fitted to a Lorentzian function and $\langle\Delta Z_c^2\rangle$ is extracted from the fit parameters instead from integration in order to eliminate contributions from white noise and

[25] Cleveland *et al.* (1993)
[26] Butt and Jaschke (1995); Hutter and Bechhoefer (1993)

higher bending modes. As only the first vibration mode is taken into account and the optical lever technique detects incorrectly the tangent of the deflection, a correction factor $\beta$ has to be implemented ($\beta_{rect.} = 0.817$ and $\beta_{V\text{-}shape} = 0.764$).

In this work, the spring constants of the cantilevers were determined exclusively in air by the thermal tune method with various instruments. In some calibration procedures the obtained values from determinations in air were compared with calibrations in liquid (mesitylene), showing a mean difference of ±13.2 % (n = 11), therefore it is quite important to follow consistently a well-defined calibration routine.

AFM Force distance curves have been applied in a broad field of science, hence, the measurement technique has become more and more sophisticated. An excellent overview article, focused slightly more on the theoretical background of force distance curves was written in 1999 by Cappella and Dietler and was refurbished in 2005 by Butt, Cappella and Kappl, highlighting state-of-the-art applications.[27]

***Colloidal probe microscopy (CPM).*** CPM has been first applied by Ducker *et al.* and Butt and Kappl with the goal of studying single particle interactions.[28] In contrast to conventional force experiments with commercially available AFM tips, microspheres of a certain diameter allow the control over both, the minuscule surface forces and the functionalization of the tip which is usually cumbersome with conventional AFM tips due to their high curvature.

In CPM a sphere is approaching a flat surface. By Derjaguin approximation the influence of the arbitrary geometry on the interaction with the surface is reduced to the simple geometry of two planar surfaces. This leads to the following expression for the interaction potential $U$:

$$U(D) = 2\pi R \int_D^\infty U_A(x)\mathrm{d}x \tag{4}$$

with: radius of the sphere $R$, distance to the surface $D$, energy per unit area $U_A$ and the distance for each unit area to the surface $x$.

[27] Butt *et al.* (2005); Cappella and Dietler (1999)
[28] Butt *et al.* (2005); Ducker *et al.* (1991)

By considering: $F(D) = \int f(x)dA$ ; $F = -\mathrm{d}U/\mathrm{d}D$ and $f = -\mathrm{d}U_A/\mathrm{d}x$
following expression can be obtained:

(5) $$U_A = \frac{F}{2\pi R}$$

with: the overall interaction force $F$, and the force per unit area between two flat surfaces $f$.
A larger tip radius results in a higher force and thus an increase in sensitivity per $U_A$. However, improving the force sensitivity by the application of CPM leads to the drawback of reducing the lateral resolution.
As examples for the amenity of CPM in relation to overcome challenges in functionalizing AFM probes, the coating with a lipid bilayer or functionalization with stiff, rod-like polymers like actin-filaments can be mentioned (sections 4.2 & 4.3).

***Hydrodynamic impact on the approach of a sphere to a surface in fluids.*** Hydrodynamic effects have to be taken into account for force distance experiments performed with colloidal probes and considerable high velocities as shown in figure 4. While approaching or retracting a microsphere from a surface, liquid close to the gap has to be squeezed out or filled up. The hydrodynamic force increases proportionally to the velocity and is dependent on the properties of the fluid, probe and surface. In fast-pulling single molecule experiments, the hydrodynamic effect can be minimized by using ultra-small cantilevers with sharp tips.
At low Reynolds numbers [$Re = (\rho \cdot R \cdot v_{\mathrm{tip}} / \eta) < 1$; $\rho$: density, $\eta$: viscosity], where viscous friction forces are dominant (laminar flow), a sphere of radius $R$ retracting from a surface with a velocity $v_{\mathrm{tip}}$ encounters an attractive force at the distance $h$:[29]

(6) $$F(h) = \frac{6\pi\eta R^2}{h} \cdot v_{tip}$$

Derived from the Navier-Stokes equation, this spherical model predicts an infinite force at contact ($h = 0$) which is not consistent with experimental observations. It is valid as an approximation for cantilever microspheres in the case of small distances $h$ compared to the size of microspheres ($h \ll R$). In a more accurate approach, the

[29] Cox and Brenner (1967)

cantilever's geometry is to be taken into account. This extended geometry can be described by the effective cantilever radius $a_{\text{eff}}$ and an effective tip/probe height $h_{\text{eff}}$.[30]

$$F(h) = \frac{6\pi\eta R_{eff}^2}{(h+h_{eff})} \cdot v_{tip} \tag{7}$$

Both parameters can be retrieved by fitting the drag force obtained via low amplitude oscillations of different frequencies at different distances and extrapolated to $h = 0$.[31]

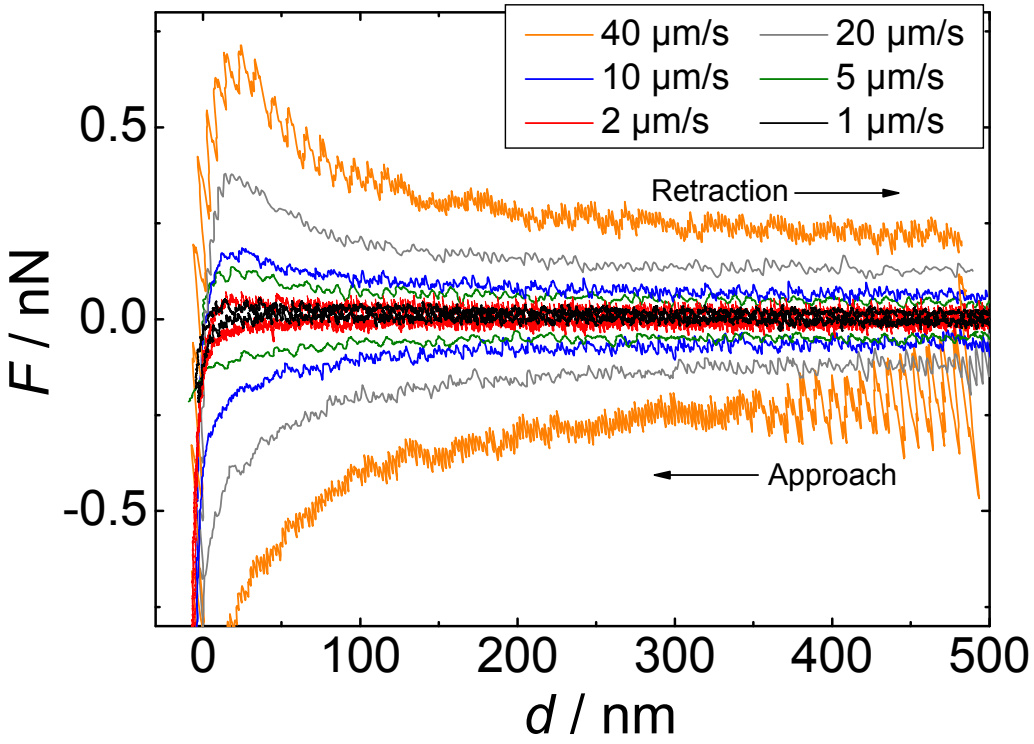


**Figure 4:** Force distance curves of a cantilever microsphere (Ø = 14.5 µm) obtained with different velocities in a buffer solution (substrate: oxidized silicon). Hydrodynamic forces are apparent, increasing with higher velocities and closer to the surface. At the highest velocity of 40 µm/s (orange curves) a transient oscillation from the acceleration of the cantilever can be observed. Zero force was determined by taking the midpoint between trace and retrace at 500 nm distance to the surface.

An important issue in fluid dynamics in proximity to a surface is the hydrodynamic boundary condition between the liquid and solid surfaces. For water on hydrophilic surfaces, almost no slip occurs; this can be explained by the fact that molecules in direct contact to the surface stick to it and do not slide laterally. When the solid

[30] Janovjak *et al.* (2004)
[31] Alcaraz *et al.* (2002)

moves, the liquid molecules respond immediately with the same velocity of the surface. Hence, slippage occurs typically for low fluid-wall interactions, e.g. in case of water for hydrophobic and smooth surfaces. An important parameter to define the slippage is the slip length $b$, the distance behind the liquid-solid interface at which the movement of the liquid molecules extrapolates to zero. The slip length $b$ can also be characterized by the bulk viscosity $\eta_b$ and the viscosity $\eta_s$ close to the solid, at the distance $h$:

$$b = h\left(\frac{\eta_b}{\eta_s} - 1\right) \tag{8}$$

In order to consider the slippage when calculating the hydrodynamic drag force $F(h)$, the scaled spherical theory can be extended by a correction factor $f^*$.[32]

$$F(h) = \frac{6\pi\eta R^2}{(h)} \cdot v_{tip} \cdot f^* \tag{9}$$

$$\text{with } f^* = \frac{(h)}{3b}\left[\left(1 + \frac{(h)}{6b}\right)\ln\left(1 + \frac{6b}{(h)}\right) - 1\right] \tag{10}$$

In the experiments conducted in this work with CPM only aqueous solutions on hydrophilic surfaces were used. Hence, slippage can be neglected and the formula remains as mentioned above (no-slip boundary condition: $f^* = 1$). Furthermore, the usual pulling velocity in the conducted experiments with microspheres was 1 µm/s. As shown in figure 4, the hydrodynamic impact on the measured forces is rather low at such velocities.

[32] Vinogradova (1995)

# 3 EXPERIMENTAL PROCEDURES

The application of AFM requires smooth and clean surfaces and high-grade purified materials. In contrast to classical ensemble measurements (e.g. optical microscopy) only a small section of the sample, sometimes only a single molecule, is addressable. Therefore, artifacts easily lead to misinterpretation of the experimental data and should be avoided in any case. In this chapter, some general aspects concerning substrates for AFM applications are presented at first, followed by explaining the exact preparation procedures for the individual experiments as well as their implementation.

## 3.1 Substrates

Very convenient substrates for AFM applications are mica and highly ordered pyrolitic graphite (HOPG) because of their planar surface and the simple way of preparation by stripping of their top layer. The layer structure of HOPG is spectacularly shown in the following figure.

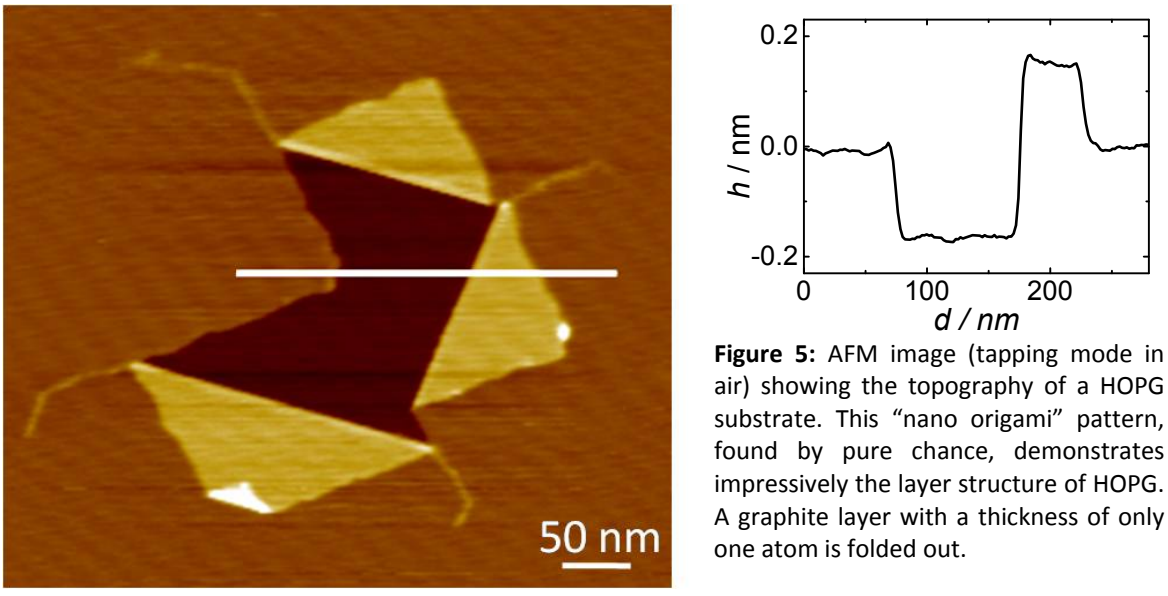


**Figure 5:** AFM image (tapping mode in air) showing the topography of a HOPG substrate. This "nano origami" pattern, found by pure chance, demonstrates impressively the layer structure of HOPG. A graphite layer with a thickness of only one atom is folded out.

Mica features an undesirably high negative surface charge (reported values range from 0.02 and 0.5 $e^-/nm^2$).[33] In the case of solid-supported membranes, this high surface charge of mica perturbs the flip-flop properties of charged lipids, resulting in an inaccurate interleaflet distribution of the lipids. In the presence of calcium ions

[33] Israelachvili and Adams (1977); Pashley (1981)

an enrichment of negatively charged lipids to the mica-facing leaflet of solid-supported bilayers was recently discovered by Richter *et al.*[34]

HOPG is hydrophobic and thus generally not appropriate for the preparation of lipid bilayers, though very useful as substrate for imaging organic compounds like calixarenes as shown in chapter 5.2 (pp 63ff.).

In this work, two materials were mainly used as substrates: gold and silicon dioxide. While $SiO_2$ exhibits a similar smoothness as mica and a lower surface charge, gold substrates provide an enormous variety of surface modifications via thiols or disulfides.

Here, both materials are briefly highlighted with regard to AFM applications.

***Oxidized silicon wafers.*** First, pieces of a silicon wafer (1 × 1) $cm^2$ are thoroughly cleaned with isopropanol and water and then placed in an aqueous solution of 1 % (v/v) HF at room temperature for 15 min to remove the native silicon oxide layer. After intensively rinsing with water, the hydrophobic silicon is incubated in a solution of $H_2O$, $NH_4OH$ and $H_2O_2$ (5 : 1 : 1) at 70 °C for 15 min to grow a new thin hydrophilic silicon oxide layer. If the substrates are not immediately used after this treatment, they can be stored under water for a maximum of one week and treated with oxygen plasma for 10 min prior usage. As shown in figure 6, in rare cases, small, round irregularities with a depth of about 0.5 nm can be observed on the surface of silicon wafers that are treated in such a way. These holes presumably originate from air bubbles that stick to the hydrophobic surface during the treatment, slowing down the growth of the $SiO_2$ layer. Therefore, continuous stirring or the use of a sonification bath during the oxidation procedure is recommended.

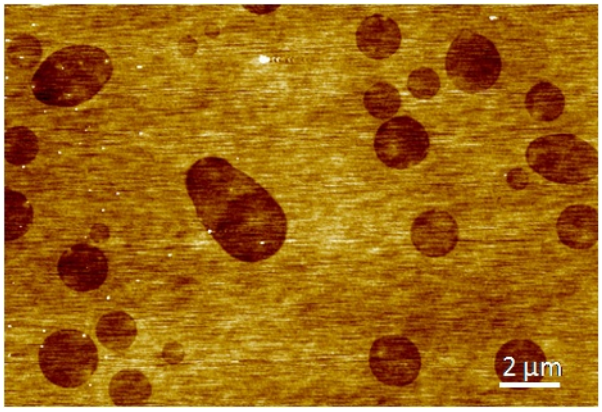


**Figure 6:** AFM image (tapping mode in air) showing the topography of a silicon wafer after standard treatment to obtain a hydrophobic silicon oxide layer. The holes are about 0.5 nm deep and are rarely observed.

[34] Richter and Brisson (2005)

***Ultraflat (mica-stripped) gold.*** Due to the fact that it is easy to functionalize gold surfaces by self assembled monolayers (SAM), the prospects of gold substrates seem to be endless. Unfortunately, gold tends to cluster during its vacuum deposition on surfaces, resulting in an amorphous cauliflower-like structure that is in most cases too rough for AFM applications. A smart way to overcome this problem is the preparation of smooth gold surfaces by template stripping.[35] In this method, gold is deposited first onto mica and afterwards a glass slide is glued on top of the gold surface. Finally the mica layer is cleaved off and a gold surface with a roughness in the subnanometer scale emerges. To ascertain that all mica layers are removed, the conductivity of the surface should be checked before proceeding with further functionalization steps.

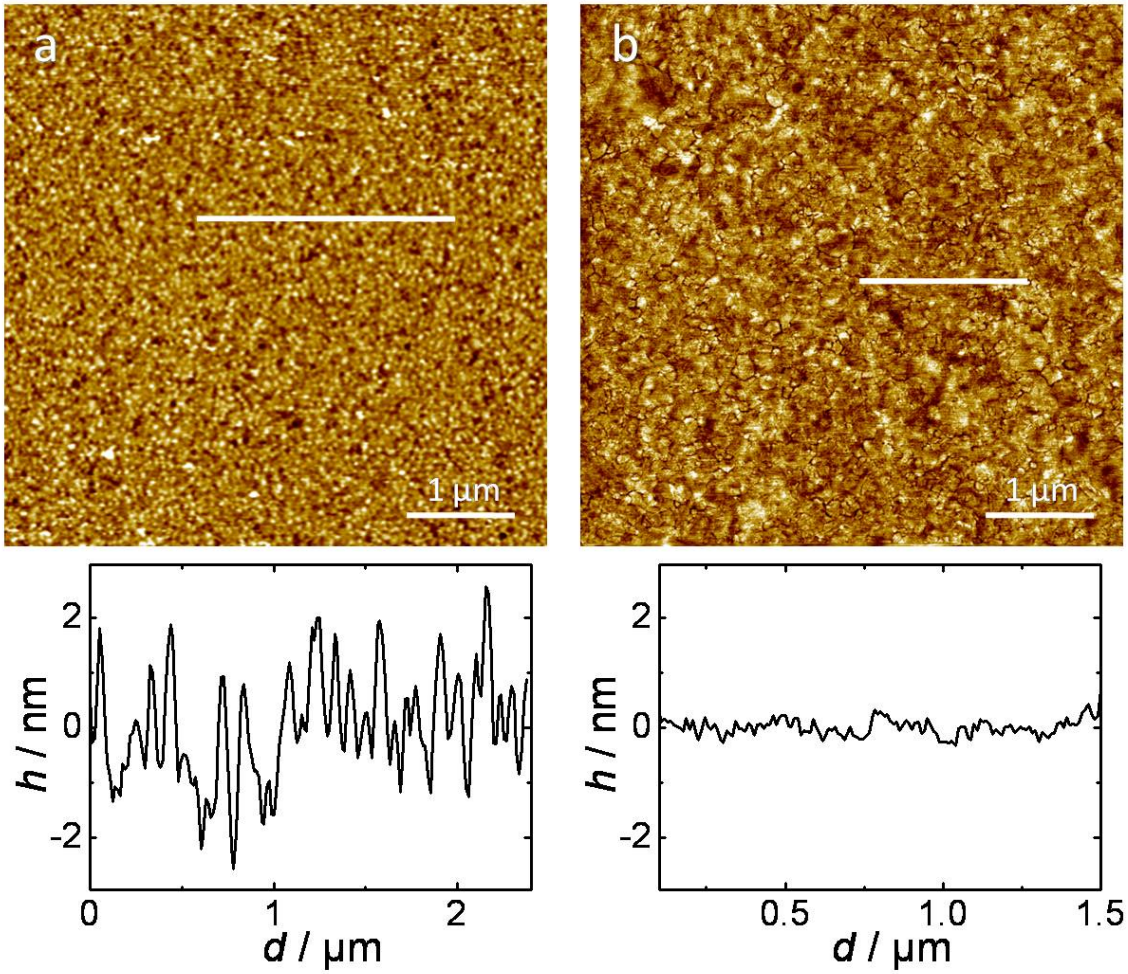


**Figure 7:** AFM height-images (tapping mode in air) of gold surfaces, including corresponding line scans. **a)** Gold on silicon exhibting a root-mean-square (RMS) roughness of 0.8 nm obtained by thermal evaporation in UHV. **b)** Ultraflat, mica-stripped gold exhibiting a RMS roughness of 0.2 nm.[36]

[35] Wagner *et al.* (1995)
[36] Image obtained in collaboration with Marco Tarantola.

## 3.2 Materials and sample preparation: ezrin-actin experiments

***Protein purification.*** Ezrin was recombinantly expressed in *Escherichia coli* cells (strain BL21(DE3)pLysS) and purified as described in detail elesewhere.[37] In brief, protein expression was induced by adding 1 mM isopropyl-β-D-thio galactopyranoside and after 3 hours the cells were harvested by centrifugation (5,000 × *g*, 10 min, 4 °C) and resuspended in lysis buffer (50 mM Tris/HCl, 20 mM imidazole/HCl, 300 mM NaCl, 1 mM EDTA, 10 mM β-mercaptoethanol, 1 mM PMSF, 10 µM leupeptin, pH 7.5). Lysis of the cells was achieved by sonification and the lysate was centrifuged for 1 hour and 100,000 × *g* at 4 °C. The supernatant was applied to a Ni-NTA agarose column (Qiagen, Hilden, Germany) equilibrated in lysis buffer. After washing the column with lysis buffer containing 25 mM imidazole/HCl, pH 7.5 and 35 mM imidazole/HCl, pH 7.5, ezrin was eluted at 300 mM imidazole/HCl, 10 mM β-mercaptoethanol, 1 mM PMSF, pH 7.5. The full-length protein with the His-tag at the N-terminus was stored at 4 °C.

***Preparation of solid-supported membranes and ezrin adsorption.*** Thin lipid films consisting either of POPC/$PIP_2$ (different molar ratios with a maximum proportion of 9:1) or DOPC/DOGS Ni-NTA (9 : 1) were formed on the wall of a glass flask by solvent evaporation under a stream of nitrogen, followed by drying the thin film for 3 h under vacuum at room temperature and storage at 4 °C.[38] Multilamellar vesicles (MLVs) were obtained by swelling the lipid films in buffer solution (20 mM Tris/HCl, 50 mM KCl, 2 mM $CaCl_2$, 1 mM $NaN_3$, pH 7.4) for 30 min and vortexing the suspension 3 times (30 s every 5 min). MLVs were transformed into large unilamellar vesicles (LUVs) by forcing the vesicle solution through a polycarbonate membrane with average pore diameters of 100 nm using a mini-extruder (LiposoFast™, Avestin, Canada).

Bilayer formation was achieved by mounting pieces of freshly oxidized silicon wafers onto a sample holder, followed by incubating with LUVs (0.3 mg/ml) for 1 h

[37] Koltzscher *et al.* (2003)

[38] Abbreviations: POPC: 1-Palmitoyl-2-oleoyl-*sn*-glycero-3-phosphocholine. $PIP_2$: L-α-Phosphatidylinositol-4,5-bisphosphate. DOPC: 1,2-Dioleoyl-*sn*-glycero-3-phosphocholine. DOGS-Ni-NTA: 1,2-Dioleoyl-*sn*-glycero-3-{[N(5-amino-1-carboxypentyl) imino-diacetic-acid] succinyl} (nickel salt).

and subsequently flushing with 20 mM Tris/HCl, 50 mM KCl, 0.1 mM EDTA, 1 mM $NaN_3$, pH 7.4. If bilayers containing DOGS-Ni-NTA were prepared, the same buffer without EDTA was used for rinsing.
Thereafter, ezrin was injected to a final concentration of 0.5-1 µM and incubated for 12 h at 4 °C. Afterwards the sample was gently flushed with F-buffer (20 mM Tris/HCl, 50 mM KCl, 2 mM $MgCl_2$, 1 mM ATP, 1 mM $NaN_3$, pH 7.4).

***Ellipsometry.*** Bilayer formation on silicon wafers and ezrin binding to planar bilayers immobilized on silicon supports were monitored by time-resolved ellipsometry employing an EL-X-02C (DRE, Ratzeburg, Germany) ellipsometer equipped with a HeNe-laser ($\lambda = 632.8$ nm). The angle of incidence of the incoming light was 70 °. With a rotating polarizer and a quarterwave plate elliptically polarized light is generated that is reflected from the sample surface resulting in linearly polarized light. A rotating analyzer is then set to zero intensity and from the rotational positions of polarizer and analyzer the ellipsometric angles Delta and Psi are calculated. Layer thicknesses of the lipid bilayer and the protein monolayer were calculated by using the following refractive indices for silicon ($n_{Si} = 3.8816$), silica ($n_{SiO2} = 1.4571$), lipid bilayer ($n_{Mem} = 1.4840$), protein ($n_{Protein} = 1.5000$) and water ($n_{H2O} = 1.3328$).

***Atomic Force Microscopy – imaging of the ezrin adsorption.*** To elucidate the influence of the $PIP_2$ concentration on ezrin binding to a membrane, the molecular organization was visualized by AFM. Measurements were carried out with a commercial scanning force microscope (Dimension 3100, Veeco Digital Instruments, CA, USA) and $Si_3N_4$ cantilevers (OMCL-TR 400 PSA, Olympus, Japan). All topographs were measured in tapping mode in buffer solution with a scan speed according to the scan size (frame size 3 - 40 µm) between 1 and 2 Hz.

***Actin polymerization.*** Purified non-muscle G-actin (monomer), exhibiting an isotype composition of 85 % β-actin and 15 % γ-actin, was purchased from Cytoskeleton (Denver, CO, USA). For polymerization, the concentrated G-actin solution (10 mg/ml in 5 mM Tris/HCl, 0.2 mM $CaCl_2$, 0.2 mM ATP, 5% (w/v) sucrose and 1 % (w/v) dextran) was diluted to 1 mg/ml in F-buffer (20 mM Tris/HCl, 50 mM KCl, 2 mM $MgCl_2$,

1 mM ATP, 1 mM $NaN_3$, pH 7.4) and kept at 4 °C overnight. To perform fluorescence microscopy, 0.05 µM Alexa Fluor® 488 phalloidin (Invitrogen, CA, USA) was added.

***Fluorescence Microscopy.*** Actin labeling was performed using 0.05 µM Alexa Fluor® 488 phalloidin which binds selectively and with high affinity to F-actin. Fluorescence images were obtained with an epifluorescence microscope (BX 51, Olympus, Japan) equipped with 10×, 40×, 100× water-immersion objectives. Fluorescence light was detected using filter set U-MNB2 (Olympus, Japan) with following settings: excitation filter: 470 − 490 nm (blue light), dichromatic filter: 500 nm and emission filter: 520 nm.

***Colloidal Probe Microscopy: Cantilever-bead preparation and functionalization.*** To perform force distance experiments, silica microspheres (Ø: 14.5 µm, Bangs Laboraties, USA) were glued with epoxy heat resin (Epikote 1004, Shell) to the ends of AFM cantilevers (MLCT, type C, $k \approx 10$ pN/nm, $f_0 \approx 8$ kHz, Veeco, CA, USA). After cleaning in water, isopropanol and argon plasma for 60 s (Plasma Cleaner, Harrick, NY, USA) the cantilevers were coated with 3 nm chromium and 30 nm gold on both sides to prevent them from bending. In the next step the cantilever-beads were immersed in 1 mM trimethyl ammonium undecanthiol ($AUT^+$, ProChimia, Poland) dissolved in isopropanol for 12 h and finally rinsed with isopropanol. The cantilevers were then immersed for 12 h at 4 °C in a 0.02 mg/ml F-actin solution and subsequently washed with F-buffer. Successful functionalization of the colloidal probes with a sufficient coverage with F-actin was verified by fluorescence microscopy (see chapter 3.3).

***Atomic Force Microscopy / Colloidal Probe Microscopy (CPM).*** AFM measurements concerning the interaction between actin and ezrin were carried out with a MFP-3D microscope (Asylum Research, CA, USA) at 20 °C in F-buffer. Bilayer formation and protein coverage were confirmed and characterized by AFM imaging in tapping mode. Only those samples exhibiting complete coverage of the bilayer with ezrin were used for CPM. In this case cantilevers were changed and force distance experiments with F-actin functionalized colloidal probes were performed. Formation of protein-protein ties was enhanced by setting a 1 s dwell time of the cantilever on

the substrate before retracting. Load forces did not exceed 200 pN and no significant impact of the load force on the adhesion forces was found. The exact spring constants of the cantilevers were determined by the thermal noise method.[39] A typical loading rate of 1000 pN/s was used throughout all experiments and the force distance curves were corrected for hydrodynamic drag as reported elsewhere.[40]

## 3.3 Materials and sample preparation: Calixarene experiments

The bis-loop tetra-urea calix[4]arene-catenanes (force distance experiments) and the bis tetraurea calix[4]arenes (scanning force microscopy) were synthesized and oligomerized by Dr. Yuliya Rudzevich and Dr. Ganna Podoprygorina.[41]

***Synthesis overview.*** To give a description of the keen efforts to accomplish the complex synthesis of the bis-loop tetra-urea calix[4]arene-catenanes, a brief overview of the 28-step synthesis is given here. These entangled macromolecules were used to perform single-molecule force distance experiments as presented experiments in section 5.4.

The important synthesis steps for the design of oligomerized bis-loop tetra-urea calix[4]arene-catenanes is illustrated in figure 8.

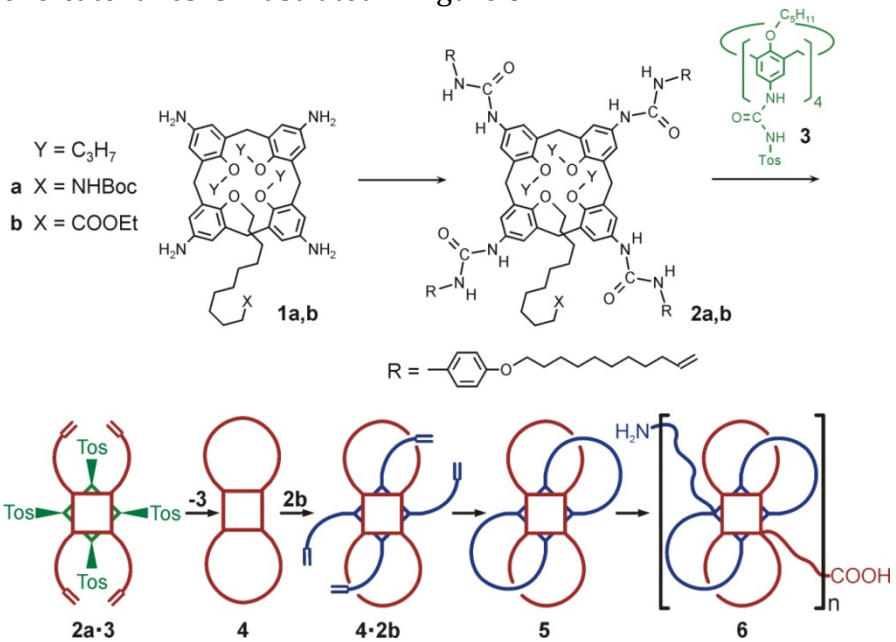


**Figure 8:** Synthesis of the oligo-bis[2]catenane **6**. In the schematic representations of the compounds **2-5** alkyl residues at the narrow rim are omitted.

[39] Butt and Jaschke (1995); Hutter and Bechhoefer (1993)
[40] Janovjak *et al.* (2004)
[41] Group of Prof. Dr. V. Böhmer, Institute of Organic Chemistry, Johannes-Gutenberg University of Mainz.

In brief, the tetraureas **2 a**,**b** were synthesized by acylation of the tetra-aminocalix[4]arenes **1 a**,**b** with isocyanate freshly prepared from the respective aniline.[42] In the following step the alkenyl urea residues of **2 a** were reorganized for the ring-closing metathesis by heterodimerization with the tetratosyl urea **3**, which prevents undesired trans-cavity bridging. After the neighbouring urea groups were connected, the dimer with **3** was destroyed and the formed double bonds were hydrogenated to give the bis-loop compound **4**. Importantly, homodimerization of tetra-urea **4** is excluded because of a sterically unfavorable overlapping of the loops. Therefore, the stoichiometric mixture with tetra-ureas of type **2** contains exclusively the heterodimers **4·2** since the small urea groups of **2** can easily pass through the loops. The alkenyl urea groups within the heterodimer **4·2 b** are again well pre-organised for the metathesis reaction, which leads to the bis-[2]catenane **5**. Cleavage of the protective Boc and ester groups, followed by oligomerisation in the presence of the PyBOP afforded the target compound **6** with 4-6 dimers on average.

*Imaging of self-assembled bis-tetra-urea calix[4]arenes.* Submonolayers of bis-calix[4]arene derivatives were prepared by spin coating. The bis-calix[4]arenes were dissolved in either pure chloroform or a mixture of 95/5 vol% chloroform / p-difluorobenzene resulting in a concentration of $10^{-2}$ to $10^{-4}$ mg/ml. A droplet of 30 µl was deposited on a freshly cleaved highly oriented pyrolytic graphite (HOPG; purchased from Plano GmbH, Germany) surface and the sample was spun at 1000 rpm for 30 s. Samples were imaged at room temperature with a commercial AFM (Nanoscope IIIa, Veeco Digital Instruments, CA, USA) in tapping mode using rectangular silicon cantilevers (Nanoworld NCH). To control and enhance the range of the attractive interaction regime, the instrument was equipped with a special active feedback circuit, called Q-control (Nanoanalytics, Germany), as described previously. The quality factor Q of this oscillating system is increased by one order of magnitude. Consequently, the sensitivity and lateral resolution are enhanced, preventing the onset of intermittent repulsive contact and thereby allowing to operate the SFM constantly in the attractive interaction regime.

[42] Rudzevich *et al.* (2005)

*Single molecule force distance experiments.* Single-molecule force measurements with bis-loop tetra-urea calix[4]arene-catenanes were carried out either with a custom-built AFM equipped with a low noise AFM detector head (Veeco Metrology group, CA, USA) and a high-resolution piezoelectric stage (Physik Instrumente, Germany) or with a conventional MFP-3D microscope (Asylum Research, Santa Barbara, CA, USA). Cantilevers (Bio-Lever, BL-RC150VB, Au coated from both sides, Olympus, Japan) and evaporated gold coverslips (substrate) were cleaned in an argon plasma for 60 s (Plasma Cleaner, Harrick, NY, USA) and subsequently immersed in solutions of 1 mM dithio bis(succinimidyl undecanoate) (Dojindo, Japan) in chloroform (cantilever) and 1 mM trimethyl ammonium undecanthiol (ProChimia, Poland) in isopropanol (substrate) for 12 h, followed by rinsing with pure solvent. The bis-loop tetraurea-calix[4]arene-catenanes were dissolved in mesitylene to a concentration of 0.3 mg/ml with 1 % (v/v) triethylamine as an additive to enhance the anchoring of the molecules. During the stretching experiments, the molecules were connected to the tip via covalent coupling between the terminal amino group and the (amine-reactive) succinimidyl ester groups of the functionalized cantilevers. While being stretched, the molecules stayed linked to the surface by electrostatic interaction between the dissociated terminal carboxyl group and the positively charged , functionalized gold substrate. In all experiments, the exact spring constant of the cantilever was determined by the thermal noise method. The force distance curves were performed with a loading rate between 60 and 30000 pN/s in mesitylene at room temperature.

# 4 Interaction of Ezrin with $PIP_2$ Containing Membranes and F-Actin

This chapter presents the results of a project driven by the ambition to create a suitable model system that mimics the plasma membrane and the actin cytoskeleton with the objective to examine their interaction mediated by ezrin. To become acquainted with the protagonists of this study, their properties and roles in biology are briefly reviewed at first. In the second part of this chapter the consecutive steps in establishing and scrutinizing a proper model system are presented. Consistently, in the experimental section, the formation of solid-supported membranes and the investigation of ezrin adsorbing on $PIP_2$-doped membranes, are presented at first. Finally, the functionalization of cantilever probes with actin filaments and force distance experiments on ezrin-covered membranes are presented and discussed.

## 4.1 Fundamentals

***The lipid phosphatidylinositol 4,5-bisphosphate ($PIP_2$).*** $PIP_2$ is the major polyphosphate inositide in mammalian cells. Even though its function is manifold, $PIP_2$ comprises only 1 % of the phospholipids in the plasma membrane, allocated asymmetrically between the extracellular (20 %) and cytoplasmic (80 %) site.[43] Compared to other phospholipids, $PIP_2$ features an extraordinary big head group that is 3-fold negatively charged under physiological conditions.

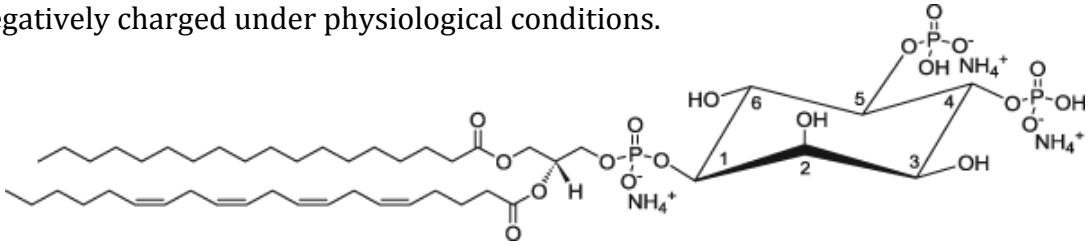


**Figure 9:** Structure of 1-stearoyl-2-arachidonoyl-*sn*-glycero-3-[phosphoinositol-4,5-bisphosphate] (triammonium salt).

As shown later in section 4.2, $PIP_2$ is spatially distributed in artificial lipid membranes that consist mainly of POPC. However, it is assumed that in the plasma membrane temporarily $PIP_2$-enriched domains exist on a submicroscopic scale due to interactions with proteins. For example the protein MARCKS (myristoylated alanine-

[43] Gascard *et al.* (1991); Zahowski (1993)

rich C kinase substrate) exhibits a basic effector domain that accumulate $PIP_2$ lipids by electrostatic interaction.[44]

Besides its well known function as precursor for the two second messengers diacylglycerol (DAG) and inositol-1,4,5-triphosphate ($IP_3$), in recent years $PIP_2$ has been distinguished to fulfill a number of other different functions in the cell. It is involved in endo- and exocytosis, membrane organization, enzyme activation and cytoskeletal attachment.[45] Corresponding to the cytoskeleton-membrane interaction $PIP_2$ recently emerged from the role as passive anchor lipid, via the ability to attract a variety of actin binding or controlling proteins, to a potential keystone in the activation mechanism of proteins.[46] The function of $PIP_2$ as activator of proteins was first conceived in the activation mechanism of the actin polymerizing regulatory protein N-WASP (neuronal Wiskott-Aldrich syndrome protein) by Prehoda and coworkers.[47] They showed that N-WASP can be triggered by $PIP_2$ alone without a second activation step; however, in co-stimulation with Cdc42 (a small GTPase of the rho-subfamily) the activation of N-WASP is enhanced. Furthermore, Janmey proposed that phosphatidylinositols and $Ca^{2+}$ are the main antagonists in regulating the assembly and disassembly of the cytoskeleton.[48] Using optical tweezers, Raucher *et al.* showed that enzyme catalyzed hydrolysis of $PIP_2$ in the plasma membrane decreases the cytoskeleton-to-plasma membrane adhesion energy considerably.[49]

Concerning the interaction with ezrin, $PIP_2$ remains in an ambiguous situation. Its function as specific anchor lipid is unquestionable,[50] whereas the contribution to the activation of ezrin is still under observation and represents a central issue of this work.

***Ezrin and the ERM-protein family.*** The plasma membrane-cytoskeleton interface is a dynamic structure, participating in a variety of cellular events. Nevertheless, only a few proteins have been identified that provide a direct link between components of

[44] Gambhir *et al.* (2004); Wang *et al.* (2001)
[45] Liu and Fletcher (2006); McLaughlin *et al.* (2002)
[46] Niggli (2005)
[47] Prehoda *et al.* (2000)
[48] Janmey and Lindberg (2004)
[49] Raucher *et al.* (2000)
[50] Blin *et al.* (2008); Herrig *et al.* (2006); Niggli *et al.* (1995)

the cytoskeleton and the plasma membrane. Among these, ezrin, radixin and moesin, belonging to the ERM protein family, have been proposed to function as linkages between the plasma membrane and F-actin in the cortex of cells.[51]

Characteristically, proteins of the ERM family are organized in two distinct domains, called N-terminal ERM association domain (N-ERMAD) and C-terminal ERM association domain (C-ERMAD). The C-terminal domain of ERM proteins harbors a F-actin binding site, whereas the N-terminal domain mediates the binding to membrane proteins and lipids.

Due to the high analogy in the structure, it is often difficult to associate an individual protein of the ERM family to a specific function in nature. Their correlating assignments in cell processes were shown impressively in experiments conducted with moesin-knock-out mice that showed no disparity to wild-type mice.[52] In addition, experiments with antisense-oligonucleotides confirmed a partial overlapping function of ERM-proteins in the formation process of microvilli.[53] However, unique roles for ERM proteins have been identified recently in genetic studies in model organisms.[54] Tamura *et al.* investigated adult ezrin-knock-out mice that suffered from severe achlorhydria (loss of gastric acid secretion). The mice exhibited stomachs decreased to $<5$ % of the wild-type levels without a compensatory up-regulation of radixin or moesin. Furthermore, increased cytoplasmic tubulovesicles and decreased apical plasma membrane infoldings called canaliculae were observed by immunofluorescence and electron microscopy.[55]

These findings show the importance of ezrin and the necessity to know more about its structure and characteristics. Ezrin, also called cytovillin or p81, consists of 586 amino acids with an overall molecular weight of ~64 kDa. It is primarily localized in the apical membrane of epithelial cells and was first isolated and purified as a cytoskeletal component of intestinal microvilli.[56] Its structure is characterized by a N-terminal (roughly 300 amino acids) and C-terminal domain (roughly 100 amino acids). The N-terminal domain is known to harbor, besides others, a binding site for

[51] Bretscher *et al.* (2002); Mangeat *et al.* (1999); Polesello and Payre (2004); Tsukita and Yonemura (1999)
[52] Doi *et al.* (1999)
[53] Takeuchi *et al.* (1994)
[54] Hughes and Fehon (2007)
[55] Tamura *et al.* (2005)
[56] Bretscher (1983)

$PIP_2$.[57] Mutagenesis experiments within the N-terminal domain revealed that the amino acids 63-72 and 253-263 are responsible for $PIP_2$ binding.[58] Furthermore, under physiological conditions, ezrin discriminates between $PIP_2$, phosphatidylinositol-4-monophosphate, phosphatidylinositol and phosphatidylserine. [59] The C-terminal domain contains an F-actin binding site consisting of 34 amino acids,[60] which makes the protein capable of directly linking the membrane to the actin cytoskeleton. However, in its dormant conformation, both domains are self-associated by a head-to-tail joining. In this conformation, the F-actin binding site is masked by the amino terminal domain, and ezrin seems to require separation of the N-and C-termini to expose the potential N-terminal membrane association site and the C-terminal F-actin binding site. To release the F-actin binding site, the phosphorylation of a threonine residue (T567) located in the C-terminal domain as well as binding to $PIP_2$ appears to be crucial.[61] Fievet *et al.* mimicked the phosphorylation of the threonine residue T567 by its replacement with glutamate (T567D mutation) and abolished the ability of $PIP_2$ binding by exchanging two lysine residues in the N-terminal domain by asparagines ($PIP_2^-$ mutation). By comparison of these two mutations with the wild type ezrin they were able to analyze the synergy between these two events in the conformational activation of ezrin *in vivo*. They demonstrated that $PIP_2$ is the primary requirement in the conformational activation of ezrin followed by the threonine phosphorylation.[62] The major role of $PIP_2$ is also manifested by experiments of Auvinen *et al.* who showed that overexpression of PIPK$\alpha$, an enzyme that catalyzes the production of $PIP_2$, relocates endogenous ezrin partially to adherens junction, suggesting opening of its dormant state.[63] However, it has not yet been proved that $PIP_2$ binding of ezrin alone is sufficient to induce a conformational switch releasing the F-actin binding site. Hence, this question will be dealt with in section 4.3.

[57] Bretscher *et al.* (2002)
[58] Barret *et al.* (2000)
[59] Niggli *et al.* (1995)
[60] Gary and Bretscher (1995); Turunen *et al.* (1994)
[61] Matsui *et al.* (1998); Simons *et al.* (1998)
[62] Fievet *et al.* (2004)
[63] Auvinen *et al.* (2007)

***Actin: structure and function.*** Monomeric globular actin (G-actin) features the ability to polymerize under certain conditions (high protein and salt concentrations) into noncovalent double-helical filaments (F-actin). In eukaryotic cells G-actin amounts to more than 5 % of all proteins, yielding to a local concentration up to several hundred µM, stabilized by regulating proteins.[64] Three main actin isotypes (alpha, beta and gamma) exist which show up to 90 % amino acid homology and up to 98 % homology within members of a specific isotypic group. While α-actin makes up a central component (~20 %) of muscle cells, β- and γ-actin are located in the cytoplasm of non-muscle cells. Without stabilizing proteins, globular actin polymerizes under physiological conditions spontaneously to actin filaments by hydrolyzing adenosine 5'-triphosphate (ATP). Due to the high affinity to polymerize, a crystallization of pure G-actin has not yet been achieved to analyze its structure. Since many actin-binding proteins inhibit a polymerization, it was possible to conduct structure analysis on crystalline actin-hybrids, resulting in about 25 publications in this field, so far.[65] The structure of actin resembles a four-leaved cloverleaf, consisting of the "small domain" with two sub-domains and the "big domain" including sub-domain 3 and 4. A cavity, located between sub-domain 2 and 4, harbors a nucleotide (ATP or ADP) in direct association with $Ca^{2+}$ or $Mg^{2+}$. The Mg-ATP-actin exhibits a faster hydrolysis and a faster elongation rate than Ca-ATP-actin, thus, Mg-actin filaments are more dynamic.[66]

Actin polymerization follows a sigmoidal growth behavior. At first, in the "lag-phase" a polymerization nucleus of three actin monomers has to be formed. It is the time-dominating step since actin-dimers are non-stable and tend to dissociate rapidly.[67] In the "growth-phase" the actin-oligomers rise until in the "steady-phase" no overall growth of the filaments occurs any more.

An important feature is the intrinsic polarity of the filaments leading to the so-called "treadmilling" mechanism under equilibrium conditions: at one end of the filament association of monomers occurs, while at the other end monomers dissociate.[68] Inspired by the arrowhead pattern created when myosin binds actin filaments, the

[64] Pollard *et al.* (2000)
[65] Reisler and Egelman (2007)
[66] Cooper *et al.* (1983)
[67] Wegner and Engel (1975)
[68] Neuhaus *et al.* (1983)

rapidly growing end of a filament is called the barbed- or plus end. The slowly growing end is called the pointed- or minus end. The capability to polymerize is dependent upon different parameters like the concentration of monomers, the salt concentration and temperature. In the presence of 2 mM $Mg^{2+}$, 50 mM KCl and 1 mM ATP non-muscle actin needs a critical concentration of 0.15 mg/ml at 4 °C to polymerize. If $Mg^{2+}$ and KCl are replaced by $Ca^{2+}$, the critical concentration increases to nearly 10 mg/ml. Actin filaments exhibit a diameter of 6-10 nm and a length of several µm.[69] Besides microtubules and intermediate filaments, (actin) microfilaments are a central part of the cytoskeleton in cells. The persistent polymerization and depolymerization of the filaments provides both stability and the ability to move. Hence, non-muscle actin plays a major role in cell migration and is in combination with other cell components involved in many cellular processes like endo- and exocytosis or the localization of cell organelles. Due to its versatile functions and the propensity to be in the filamentous form under physiological conditions, several actin-binding proteins influence the polymerization dynamics and cross-linking behavior of actin in the cell. In order to maintain the dynamic aspect, the activity of the controlling proteins is stimulated by $Ca^{2+}$, phosphorylation and negatively charged phospholipids. Hence, in non-muscle cells, actin filaments are formed near membrane surfaces and are fine-tuned by a complex combination of many controlling proteins. In consideration of trying to understand the role of each individual actin-binding protein, a strategy to build up a model system that focuses on the components of interest seems to be reasonable. Thus, a setup consisting of an artificial membrane, the actin-binding protein ezrin and actin-filaments was developed and characterized to investigate the ezrin—actin interaction by atomic force microscopy, as presented in the next sections.

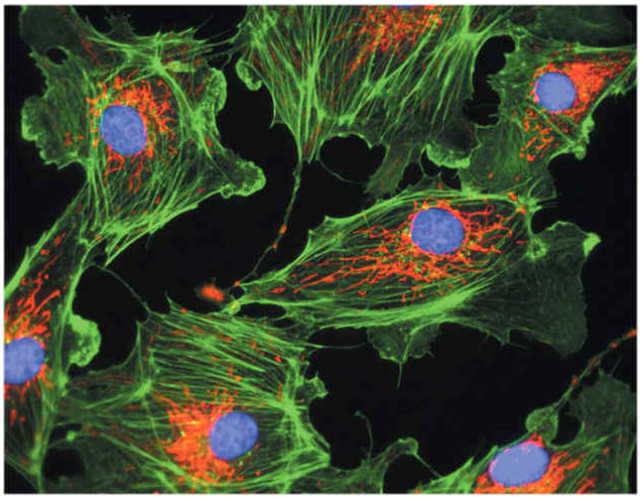

**Figure 10:** Fluorescence image showing bovine pulmonary artery endothelial cells with labeled microtubules in red, nuclei in blue and F-actin in green. The actin stress fibers are easily to identify. The image is taken from the invitrogen image gallery.

[69] Milligan *et al.* (1990)

## 4.2 Experimental results & discussion: Adsorption of ezrin on solid-supported membranes (SSM)

Before the ezrin−F-actin interaction can be scrutinized, the formation and characterization of solid-supported membranes containing $PIP_2$ or DOGS Ni-NTA as anchor lipids and their interaction with ezrin have to be investigated in detail.

***Formation of solid-supported membranes.*** Vesicles, composed of a mixture of POPC and $PIP_2$, were spread on oxidized silicon wafers to form a lipid bilayer. The formation process was monitored by ellipsometry via calculating the thickness of the new layer from a readout of delta and psi as described previously.[70]

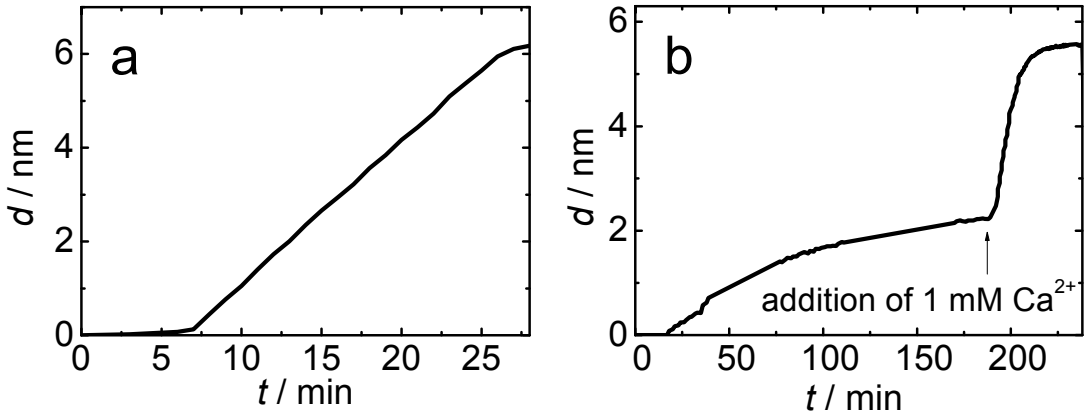


**Figure 11:** Ellipsometry measurements showing the formation of lipid bilayers on oxidized silicon by spreading vesicles (0.3 mg/ml) under stirring in 20 mM Tris/HCl, 50 mM KCl, 1 mM $NaN_3$, pH 7.4 as a function of time. **a)** Lipid composition of POPC/$PIP_2$ (99 : 1 mol%) without $CaCl_2$. **b)** Lipid composition of POPC/$PIP_2$ (97 : 3 mol%) starting without $CaCl_2$, after 190 min 1 mM $Ca^{2+}$ was added enhancing the spreading process.

Figure 11 demonstrates the effect of $Ca^{2+}$ ions on the spreading process of POPC/$PIP_2$ liposomes. Without the presence of $Ca^{2+}$ ions a formation of a defect free bilayer is possible until an amount of 1 mol% of $PIP_2$. A total increase in thickness of about 5 nm is in good accordance to the theoretical height of a lipid bilayer. At higher $PIP_2$ amounts repelling interactions between the 3-fold negatively charged $PIP_2$ molecules and the partially negatively charged $SiO_2$ surface dominate, leading to an incomplete formation of a bilayer. As shown in figure 12 a), defects in the bilayer are unwanted as intact vesicles can stick into the defect area, even after washing with buffer, resulting in a disturbance of the consecutive measurements. In order to obtain a complete bilayer, positively charged calcium ions had to be used as

[70] Faiss *et al.* (2008)

mediating agents. Figure 11 b) strikingly shows the acceleration of the bilayer formation by adding $Ca^{2+}$ ions to the vesicle suspension. It has to be noted that in the ellipsometry measurements the vesicle suspensions (0.3 mg/ml) were stirred. Without stirring the process takes longer, e.g. up to 8 h in the absence of $Ca^{2+}$ with a $PIP_2$ amount of 1 %. Thus, with respect to equal treatment, every solid-supported bilayer was prepared by adding $CaCl_2$ (final concentration: 2 mM) to the vesicle suspension just before incubating on the substrate. The vesicle suspension (lipid concentration 0.3 mg/ml) was incubated 1–2 h on the substrate and afterwards rinsed with buffer solution containing 0.1 mM EDTA. If bilayers containing DOGS-Ni-NTA were prepared, the same buffer without EDTA was used for rinsing.

After preparation of the solid-supported membranes, the surface was visualized by AFM to confirm the uniform coverage without scores of defects or stacked vesicles (see figure 12 b). If no defects were present, a scan window was scratched by scanning a small area in contact mode, applying high forces at a high scan velocity. For both lipid compositions (DOPC/DOGS Ni-NTA and POPC/$PIP_2$), the smoothness of the measured bilayer indicated a homogeneous distribution of the lipids, yet no formation of lipid domains. This conclusion is reasonable as lipids in the liquid crystal phase exhibit a high diffusion rate. FRAP (fluorescence recovery after photobleaching) measurements of phosphatidylinositols determined a diffusion constant of $\sim 0.5\ \mu m^2 s^{-1}$.[71]

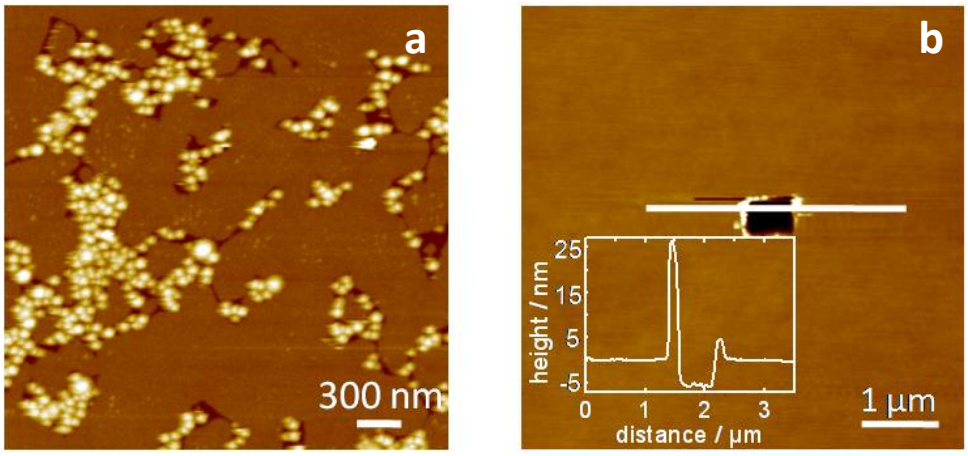


**Figure 12: a)** An AFM height-image (tapping mode) of a membrane exhibiting defects. Intact vesicles with a height of 10 nm are attached to the gaps. **b)** AFM height image of a solid-supported membrane (DOPC/DOGS Ni-NTA, 9 : 1). The scratched area exhibits a depth of 5.2 nm. This is in good accordance with the theoretical height of a bilayer.

[71] Haugh *et al.* (2000)

To perform adhesion experiments between actin filaments and an ezrin-covered bilayer or vice versa, an approach with the objective to create a cantilever probe covered with a stable lipid bilayer had to be achieved. Thus, for successful vesicle-spreading, glass microspheres were used instead of commercial AFM-tips. As shown in figure 13 covering a cantilever-bead with a bilayer composed of POPC, stained with Texas Red, was feasible.

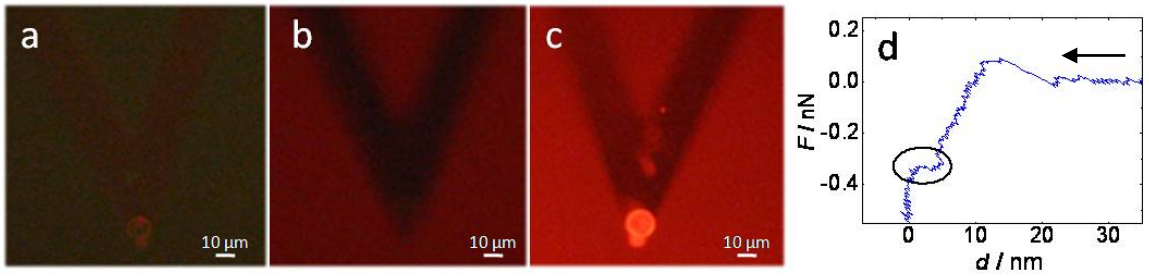


**Figure 13: a)** Glass microsphere attached to a cantilever illuminated with blue light (470 – 490 nm, 3.2 s exposure time) in buffer (20 mM Tris/HCl; 50 mM KCl; 2 mM $Ca^{2+}$; pH : 7,4) **b)** The same cantilever-bead illuminated with green light (530 – 550 nm, exposure time 4 s). **c)** After 30 min of incubation in a droplet of a vesicle suspension (1 mg/ml, POPC/Texas Red, 99 : 1 mol%), followed by rinsing with buffer. Green light, 0.25 exposure time. **d)** A $SiO_2$ substrate was carefully installed and force distance curves were performed. In the depicted approach curve a breakthrough event with a jump-in distance of 4.3 nm was observed, confirming the existence of a bilayer.

However, the number of force distance repeats with an intact bilayer-coating of the microsphere were strongly limited. This inhibited reliable adhesion experiments between actin-filaments and ezrin adsorbed on bilayer-coated cantilevers.

Therefore, in this work, CPM was mainly employed with F-actin functionalized spherical probes to provide direct information about the possible adhesive properties on samples, coated with bilayers and covered by ezrin. The tedious preparation of colloidal probes was rewarded by reliable force experiments on a meso- to microscopic length scale.

***Cooperative adsorption of ezrin on $PIP_2$ containing membranes.*** In order to study the influence of the PIP2 content in the membrane upon ezrin binding and its reversibility, QCM (quartz crystal microbalance), ellipsometry and AFM measurements were conducted.[72] Richter *et al.* have already shown that a combination of QCM and AFM allows a thorough analysis of the formation process of lipid bilayers and protein adsorption.[73] While AFM imaging provides detailed information about the arrange-

[72] Herrig *et al.* (2006)
[73] Richter *et al.* (2006); Richter and Brisson (2005)

ment of ezrin molecules on the surface, QCM measurements allow the determination of kinetic and thermodynamic parameters of the adsorption process. The QCM measurements were performed with the collaboration partner Dr. Alexander Herrig and the summarized results are briefly presented in figure 14 a).[74]

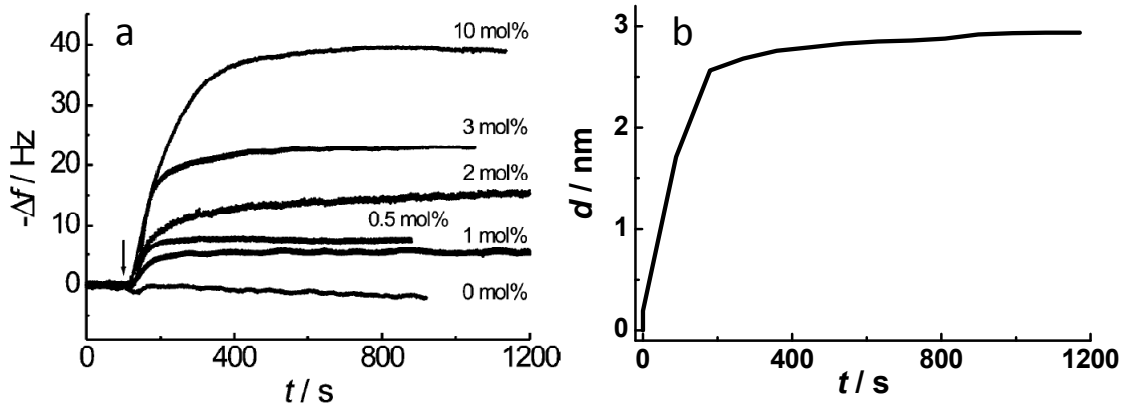


**Figure 14: a)** Representative QCM measurements of the adsorption of 0.1 µM ezrin on solid-supported membranes composed of POPC and various amounts of $PIP_2$ in ezrin-buffer. The frequency shifts (-Δ*f*) of the time courses represent the amount of ezrin molecules deposited on the surface. Unfortunately, a conversion into the height of the adsorbed proteins is not possible due to the viscoelastic properties of the proteins. However, ellipsometry measurements give direct access to the height of the protein layer. In **b)** a representative ellipsometry measurement of the ezrin adsorption (0.2 µM) on a $PIP_2$ containing SSM is shown. In comparison to QCM measurements the ellipsometry lacked in time resolution and suitability. Thus, ellipsometry was only used as an auxiliary technique to compare the thickness of saturated protein layers with AFM height measurements.

To perform AFM measurements the adsorption of protein was initiated by injecting ezrin into the solution at a final concentration of 0.5-1 µM. At various adsorption times, AFM images were taken at room temperature as shown later in figure 18 (page 37). Because the adsorption process was diffusion-limited, coverage increased rather slowly compared to the kinetics monitored by QCM or ellipsometry where the solution was in constant flow.

[74] Herrig (2007)
Group of Prof. Dr. C. Steinem, Institute of Organic and Biomolecular Chemistry, University of Göttingen.

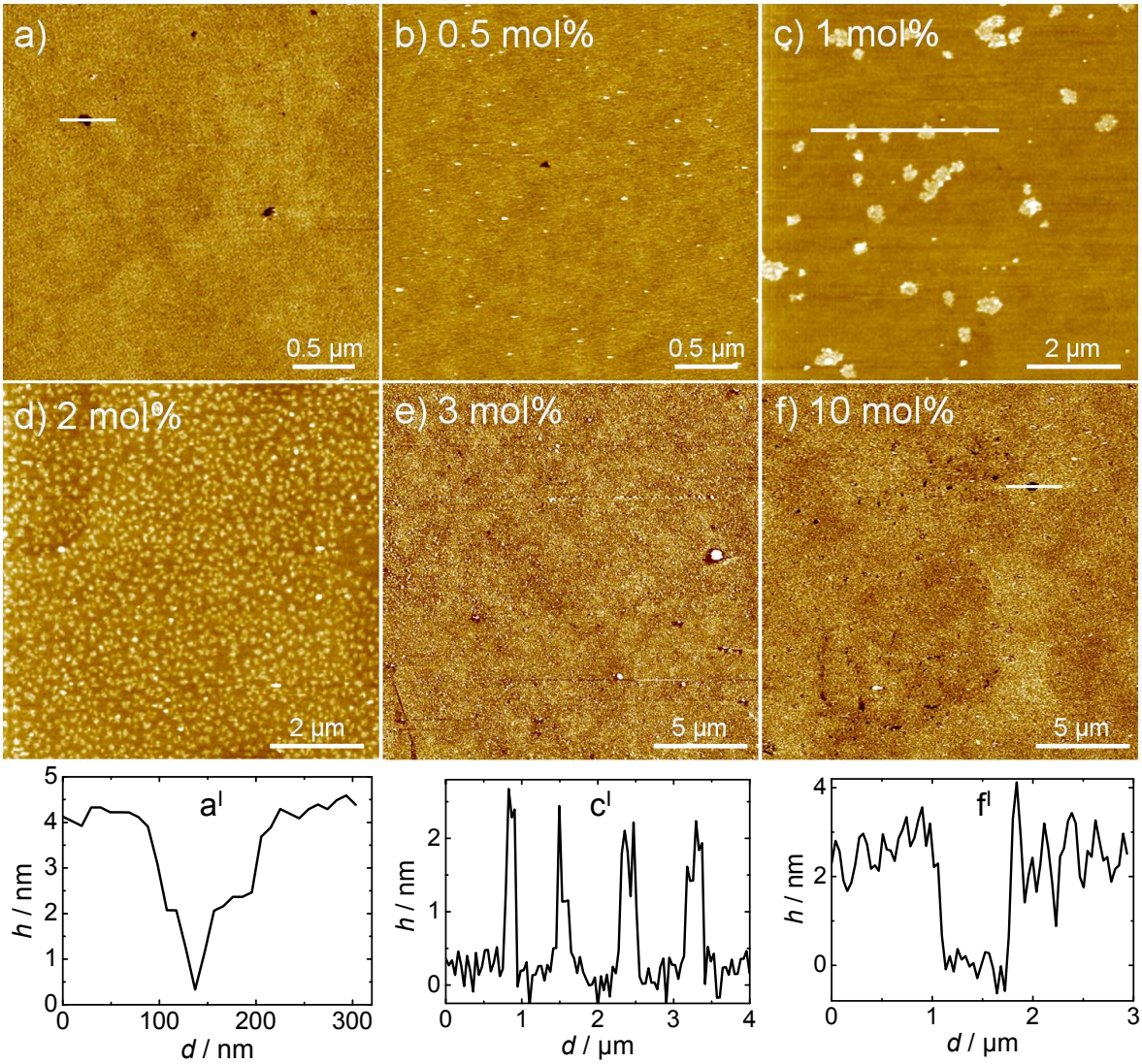


**Figure 15:** AFM images showing the topography (tapping mode) of solid-supported membranes with different amounts of $PIP_2$ in 20 mM Tris/HCl, 50 mM KCl, 0.1 mM EDTA and 1 mM $NaN_3$ at pH 7.4. **a)** Membrane containing 3 mol% $PIP_2$ before the addition of ezrin. **a')** Cross-section along the line shown in a). Membranes containing **b)** 0.5 mol% $PIP_2$, **c)** 1 mol% $PIP_2$, **d)** 2 mol% $PIP_2$, **e)** 3 mol% $PIP_2$, and **f)** 10 mol% $PIP_2$ after the addition of 1 $\mu$M ezrin. In **c')** and **f')**, the corresponding cross-sections along the lines shown in c) and f) are presented.

Adsorption was called complete if no further binding was observed by AFM. Representative topographic images of membranes after adsorption of ezrin are depicted in parts b) – f) of figure 15 as a function of the $PIP_2$ concentration. At low $PIP_2$ concentrations, only a small area of the surface was covered by ezrin. Small protein aggregates with a height of 1.8 ± 0.2 nm as deduced from histogram analysis were observed which could be attributed to attractive lateral interactions between ezrin molecules, i.e., positive cooperative binding of ezrin to the membrane. An increase in surface coverage was observed with an increasing $PIP_2$ concentration which was in agreement with the QCM results. At a $PIP_2$ concentration of 3 mol% an almost complete surface coverage was monitored. A further increase in the $PIP_2$ concentra-

tion up to 10 mol% resulted in a complete protein coverage, consistent with the QCM results that showed a saturation at 10 mol%. In addition, the average thickness of the protein layer was analyzed by ellipsometry. After flushing with buffer a mean thickness increase of (2.4 $\pm$ 0.8) nm for ezrin bound to POPC/$PIP_2$ (10 mol%) was obtained. This confirmed the AFM height measurements from linescans over defect areas in the ezrin layer (e.g. the height profile depicted in figure 15 f[l]) shows ~2-3 nm thickness of the protein layer). From these height measurements a monomolecular protein layer can be inferred. In figure 16 the protein coverage as obtained by pixel analysis from the topography images is given as a function of the $PIP_2$ concentration in the membrane and then compared with the QCM measurements. The results are in good agreement with those of the QCM measurements shown in figure 16 b). Almost identical protein coverage at a $PIP_2$ concentration of 0.5 and 1 mol% in the solid-supported membrane is found with both techniques. With an increasing $PIP_2$ concentration, the surface coverage increases up to a maximum protein coverage of about 70 %.

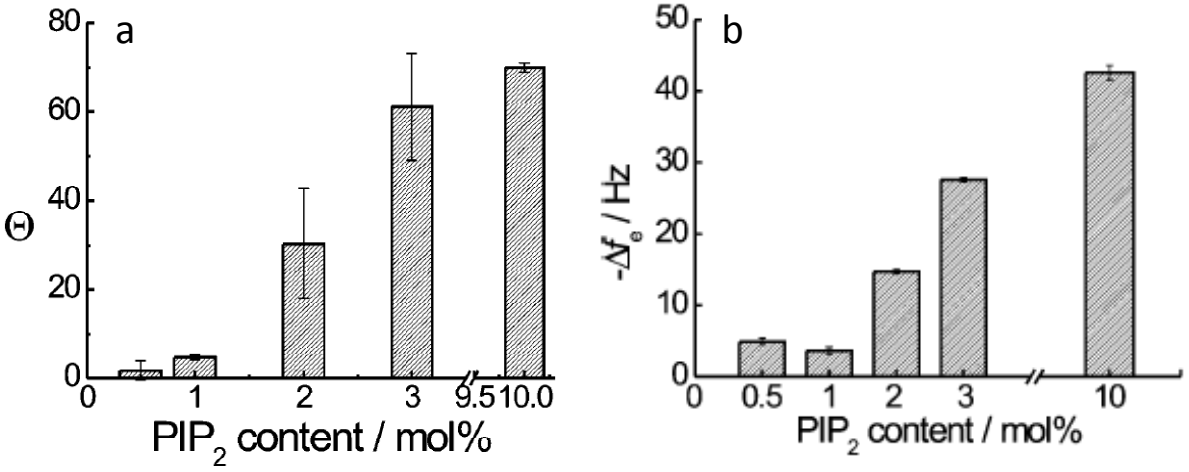


**Figure 16: a)** Mean values of the protein coverage as obtained from pixel analysis of the AFM images depending upon the $PIP_2$ content in the solid-supported membranes. The values are averages of at least four images. **b)** Mean (-Δ*f*) values of equivalent QCM measurements. Both techniques show a correlation in the results of $PIP_2$-dependent binding of ezrin to a SSM.

***Reversibility of ezrin adsorption.*** As a mediator between the plasma membrane and the cytoskeleton, ezrin appears to play a crucial role in the dynamics of actin formation. To function as such, reversibility of binding is of major importance. The reversibility of ezrin adsorption and the lateral distribution of proteins after desorption was investigated in detail by means of QCM and AFM. Figure 17 c) shows the time-resolved adsorption and desorption of ezrin on and from a membrane containing 3 mol% $PIP_2$ obtained by the QCM technique (upper image) and in the lower part a Monte-Carlo simulation, using a kinetic model, developed by Minton.[75] Beyond doubt, experiments and simulations were in good accordance. The decrease in surface coverage, beginning at 1750 s, indicates the desorption process initiated by flushing with pure buffer. The observed desorption process indicates that ezrin remains partly bound to the membrane.

To further elucidate the desorption process, AFM measurements were performed. Figure 17 a) shows an image of a POPC/$PIP_2$ (9 : 1) lipid bilayer on which ezrin had been adsorbed before the specimen was rinsed thoroughly with buffer. Prior to flushing with buffer, the surface was completely covered with protein. After flushing with buffer, some large defect areas with a depth of ~2 nm were clearly discernible, while most of the protein still remained bound to the surface. Apparently, the protein desorbed preferentially in certain areas, while in others, it remained completely membrane-bound, which might be ascribed to lateral protein-protein interactions increasing the overall affinity of the protein to the membrane considerably.

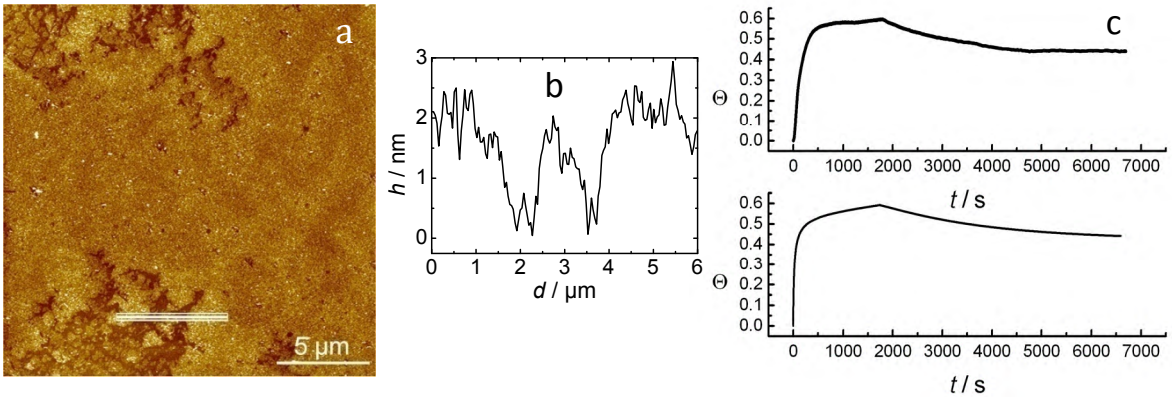


**Figure 17: a)** AFM height-image (tapping mode) of a solid-supported membrane (10 mol% $PIP_2$) after the adsorption of ezrin and after rinsing the sample thoroughly with buffer. **b)** Cross-section along the line shown in a).**c)** Representative time course of the adsorption of 0.3 µM ezrin to a solid-supported POPC/$PIP_2$ (97 : 3) membrane measured with QCM (upper part). After 1750 s the desorption process was initiated by flushing with pure buffer. Simulated data points are shown in the lower part. All QCM measurements and simulations were performed by Dr. Alexander Herrig.

[75] Minton (2000); Minton (2001)

The hypothesis of a cooperative lateral interaction or oligomerization was further confirmed by time-elapsed AFM images of a $PIP_2$-containing membrane after the addition of ezrin. As shown in figure 18, the ezrin monolayer grows starting from a few nucleation sites, governed by attractive lateral interactions of the proteins on the membrane.

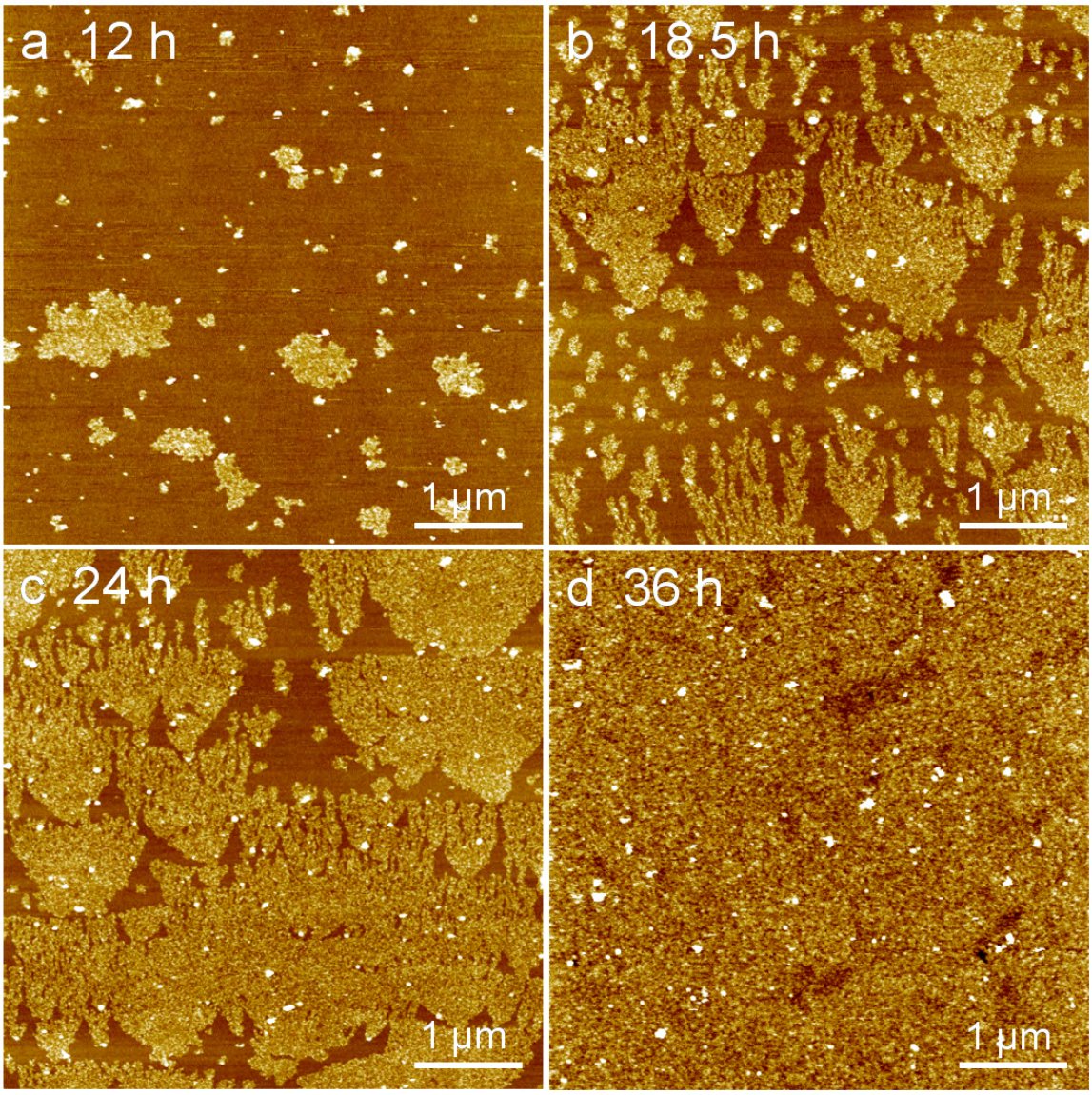


**Figure 18:** Time-elapsed AFM images showing the topography (tapping mode) of a solid-supported membrane (3 mol% $PIP_2$) after the addition of ezrin. **a)** 12 h after the addition of ezrin ($c_{ezrin}$ = 0.35 $\mu$M) and **b)** after 18.5 h, **c)** 24 h, and **d)** 36 h incubation time with ezrin ($c_{ezrin}$ = 1.5 $\mu$M).

***Discussion.*** In combination with the QCM technique, AFM was employed to gather information about the interaction of ezrin with $PIP_2$-containing solid-supported membranes. AFM measurements provided detailed conclusions about the lateral arrangement of membrane-bound ezrin and its dependence on the $PIP_2$ content in the membrane. Based on the results presented above, a positive cooperative binding process of ezrin to $PIP_2$-doped membranes is proposed. When ezrin is bound to the lipid membrane, attractive lateral protein-protein interactions occur, resulting in monolayer ezrin clusters on the surface, as proven by AFM. In comparison to the height of approximately 4 nm of the crystalline N-terminal domain of ezrin,[76] the measured height of the clusters is about half of that. This may be a result of mechanical deformation caused by the AFM tip.[77] The formation of these clusters only occurs after binding to $PIP_2$ and is not initiated in solution. It has been reported by others as well that ezrin does not form oligomers ($n > 2$) in solution,[78] but exhibits the propensity to form oligomerized assemblies on surfaces.[79] Higher ordered adducts of ezrin have been found in extracts of placental microvilli and in gastric parietal cells. In addition, it has been shown that epidermal growth factor (EGF) stimulation of human epidermoid carcinoma cells induces the rapid formation of ezrin oligomers.

The $PIP_2$-binding motif of ezrin contains several lysine residues, which are crucial for the $PIP_2$ interaction.[80] Binding of an ezrin molecule to $PIP_2$ may induce a recruitment of additional $PIP_2$ molecules towards the protein which would result in a $PIP_2$ depletion of the residual membrane. It has been shown that binding of basic peptides to membranes leads to the formation of lateral domains enriched in $PIP_2$.[81] Because of this process, it is likely that not all $PIP_2$ molecules are accessible for further ezrin adsorption. At $PIP_2$ concentrations of 3 mol% and larger, an almost complete coverage of the surface is observed by AFM. If one calculates the surface coverage of ezrin, assuming that one $PIP_2$ molecule occupies an area of 70 Å$^2$ and binds one ezrin molecule, which covers an area of about 5000 Å$^2$,[82] a maximum coverage

[76] Smith *et al.* (2003)
[77] Bayburt *et al.* (2000); Menke *et al.* (2005)
[78] Bretscher *et al.* (1995); Chambers and Bretscher (2005)
[79] Berryman *et al.* (1995); Bretscher *et al.* (1995); Chambers and Bretscher (2005); Zhu *et al.* (2005)
[80] Barret *et al.* (2000)
[81] Denisov *et al.* (1998)
[82] Hamada *et al.* (2000); Smith *et al.* (2003)

is expected at a $PIP_2$ amount of 2 mol%. However, the statistical evaluation of the AFM data shows that at 2 mol% of $PIP_2$ of the surface coverage is only around 30 % which is around half of that expected from the calculation. Besides experimental uncertainties, an explanation for this discrepancy might be found in a preferential localization of $PIP_2$ molecules underneath an ezrin molecule.Based on these conclusions, the QCM data could be modeled, employing a kinetic model developed by Minton that includes the formation and subsequent growth of monolayer surface clusters of adsorbed molecules.[83] Noteworthy, it was not possible to use a Langmuirian kinetic to describe the QCM data properly, affirming the observation of a complex positive cooperative adsorption behavior.

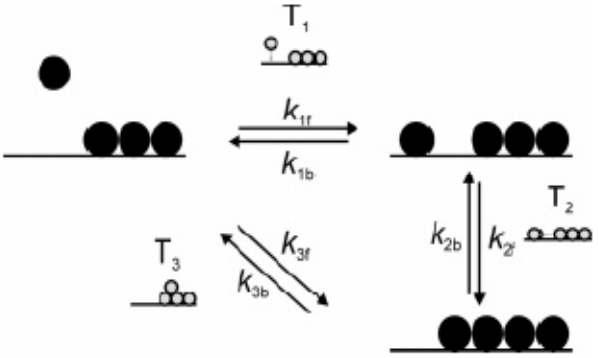


**Figure 19:** Schematic illustration of the kinetic model adapted from Minton showing the kinetic pathways and the corresponding transition states. The growth of protein clusters on the surface can either occur through direct deposition (T1) followed by accretion (T2) or by piggyback deposition (T3) and incorporation into the cluster.

***Adsorption of ezrin on DOGS Ni-NTA containing membranes.*** Ezrin contains a hexahistidin-tag (6x His-tag) at its N-terminal domain in order to facilitate an easy and rapid purification during the isolation process. The histidin groups bind with a high affinity to Ni-NTA (nitrilo-tri-acetate) by exchanging two water molecules of the octaedric $Ni^{2+}$ complex. Thus, it can be purified by affinity purification using a column that contains Ni-NTA agarose to bind specifically the His-tagged ezrin, washing the column to remove proteins that do not specifically interact with $Ni^{2+}$-ions, and eluting afterwards with a buffer containing 150-300 mM imidazole that binds with a higher affinity to $Ni^{2+}$.

[83] Minton (2000); Minton (2001)
Modelling of the QCM data was performed by Dr. Alexander Herrig and is not shown in this work.

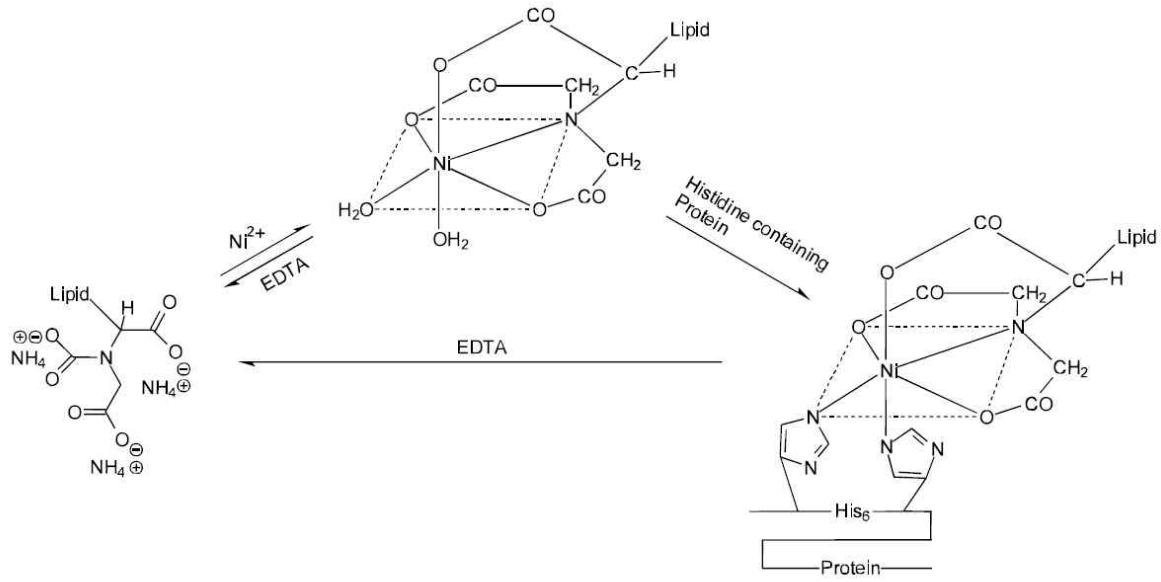


**Figure 20:** Triggering the interaction between lipids with covalently bound Ni-NTA and His-tagged proteins by EDTA and $Ni^{2+}$.

In this work ezrin was bound via its His-tag to a lipid bearing Ni-NTA at the headgroup (DOGS Ni-NTA). This non-natural manner of binding to a membrane was used as a comparative experiment to investigate the influence of $PIP_2$ on the activation of ezrin as described extensively in chapter 3.3. The successful binding of ezrin to a DOPC/DOGS Ni-NTA (9 : 1 mol%) membrane was verified by AFM and ellipsometry. AFM images indicated a thickness of the ezrin layer of $(2.5 \pm 0.2)$ nm and ellipsometry measurements (performed with an $EP^3$, Nanofilm, Germany) showed a mean thickness increase of $(3.4 \pm 0.8)$ nm. Thus, the ezrin layer was slightly higher than the ezrin-layer bound via $PIP_2$. This difference in height could be attributed to different conformations of ezrin by binding either via its His-tag or via its natural binding site. Binding to $PIP_2$ might induce conformational changes, leading to a more open configuration, resulting in a smaller thickness.

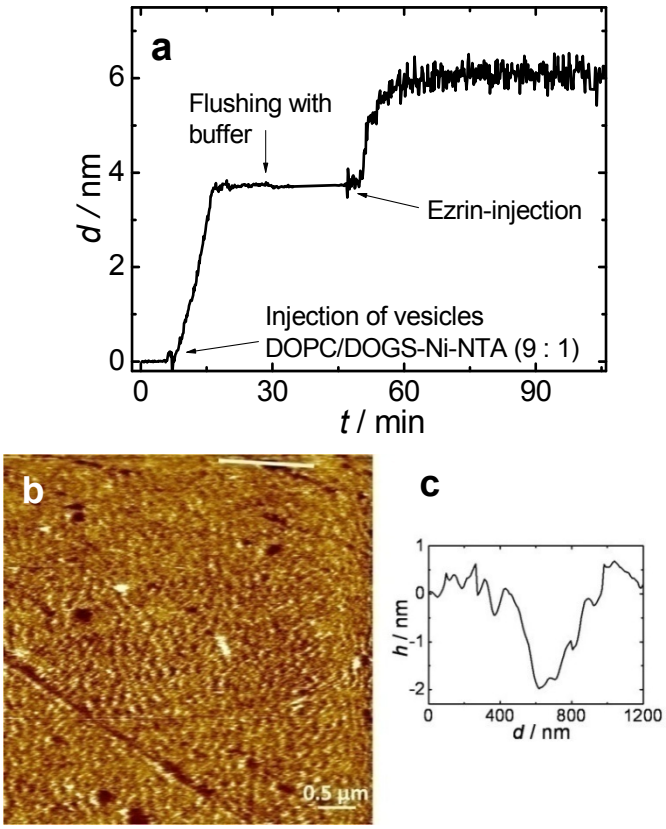


**Figure 21:** Binding of ezrin to DOPC/DOGS Ni-NTA-bilayers measured by two independent techniques. In both cases oxidized silicon was used as substrate. **a)** Ellipsometry measurement showing the formation of a SSM, followed by the adsorption of ezrin. **b)** An AFM height-image (tapping mode) of a membrane completely covered by ezrin. The height and structure indicates a monolayer of ezrin and no signs of further protein accumulations. **c)** Corresponding cross-section along the line shown in b).

## 4.3 Experimental results & discussion: Interaction between membrane-bound ezrin and actin filaments

The motivation for the following experiments originates from the question, whether binding of ezrin to $PIP_2$-containing membranes alone leads to a conformational switch from the dormant to the active state. While in the dormant state, ezrin is folded in a way that it is unable to attach to F-actin, the actin-binding site is accessible only in its active state allowing the protein to firmly bind to the actin cytoskeleton. To create ezrin-monolayers in a dormant conformation and a putative active conformation, ezrin was adsorbed on solid-supported membranes (SSMs) in two different ways. In one scenario, ezrin was attached via its N-terminal His-tag to a solid-supported lipid bilayer equipped with Ni-NTA bearing lipids leading to proteins bound in the dormant conformation. In the second scenario, ezrin was bound to the lipid $PIP_2$. The native binding site for $PIP_2$ is known to be located at the N-terminal domain.

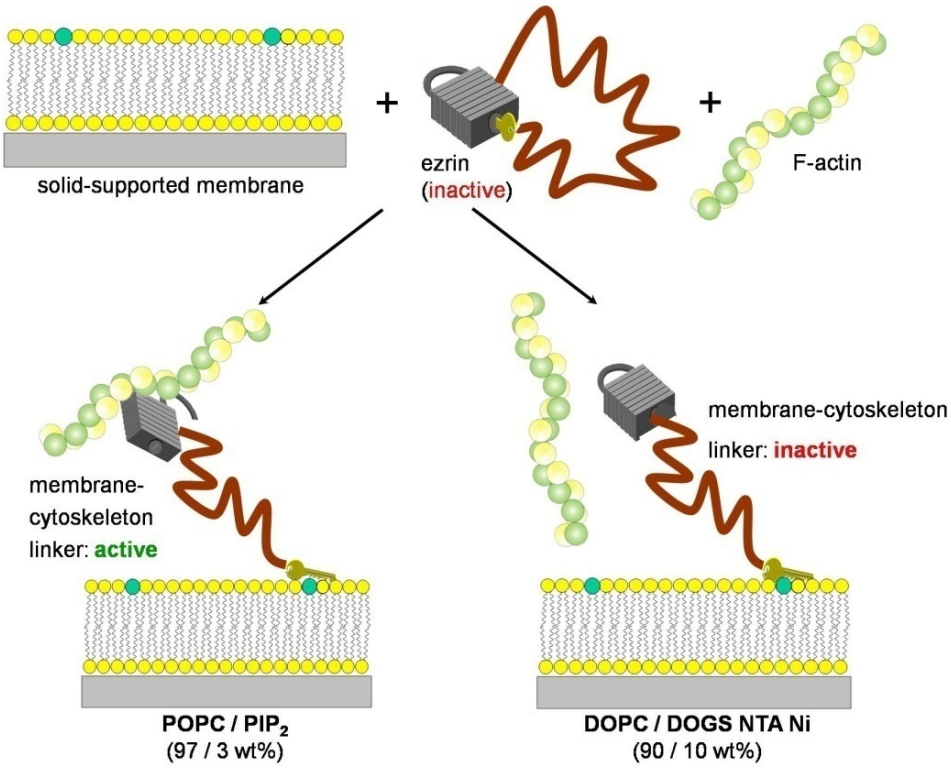


**Figure 22:** Illustration of the two binding mechanisms of ezrin to a solid-supported membrane that potentially lead to different activation states of ezrin.

The prerequisite for a quantitative determination of the adhesiveness of the ezrin – F-actin interface is a complete ezrin monolayer with only a small number of defects formed on solid-supported membranes. Therefore, both, the formation of supported

lipid bilayers and the adsorption of ezrin were monitored by ellipsometry and atomic force microscopy (AFM) providing information on the mesoscopic and microscopic length scale as already described in chapter 4.2.

***Investigation of F-actin binding to ezrin-monolayers on SSM by epifluorescence microscopy.*** By means of epifluorescence microscopy, the capability of membrane-bound ezrin to bind F-actin was investigated as shown in figure 23.
Polymerized F-actin labelled with Alexa Fluor® 488 phalloidin was added in a concentration of 50 µg/mL to membrane-bound ezrin in F-buffer. After an incubation time of 2 h, non-bound F-actin was removed by carefully rinsing the surface with F-buffer and fluorescence images were taken. The images clearly reveal that a green fluorescence is only observed if ezrin is bound to $PIP_2$-containing membranes, originating from F-actin coupled to ezrin. The surface coverage with F-actin is heterogeneous. While in some areas an almost full coverage with F-actin is observed (figure 23 a), other regions show predominantly individual F-actin filaments with an average length of about 1-2 µm (figure 23 b). Control experiments, in which either fluorescently labeled F-actin, or only the fluorophor AlexaFluor® 488 phalloidin was added to a pure POPC/$PIP_2$-membrane showed no detectable fluorescence demonstrating that non-specific binding of F-actin and AlexaFluor® 488 phalloidin to the membrane can be ruled out. Also, no fluorescence was observed if AlexaFluor® 488 phalloidin was added to POPC/$PIP_2$-bilayers, on which ezrin was adsorbed on, confirming that the fluorophor itself does not bind to $PIP_2$-bound ezrin. Images obtained from samples, where ezrin was bound to the membrane via DOGS-Ni-NTA, did not display any significant fluorescence which suggests that ezrin remains in its dormant conformation and is thus, incapable of binding F-actin. In some areas, as shown in figure 23 d), some small fluorescent spots were discernable which demonstrate the validity of the control measurement. On average, the mean surface coverage, as obtained from pixel analyses, was found to be $(24 \pm 18)$ % for ezrin bound via $PIP_2$ and almost negligible $(0.3 \pm 0.2)$ % for ezrin bound via DOGS Ni-NTA. The rather large error is a result of the heterogeneous distribution of bound F-actin.

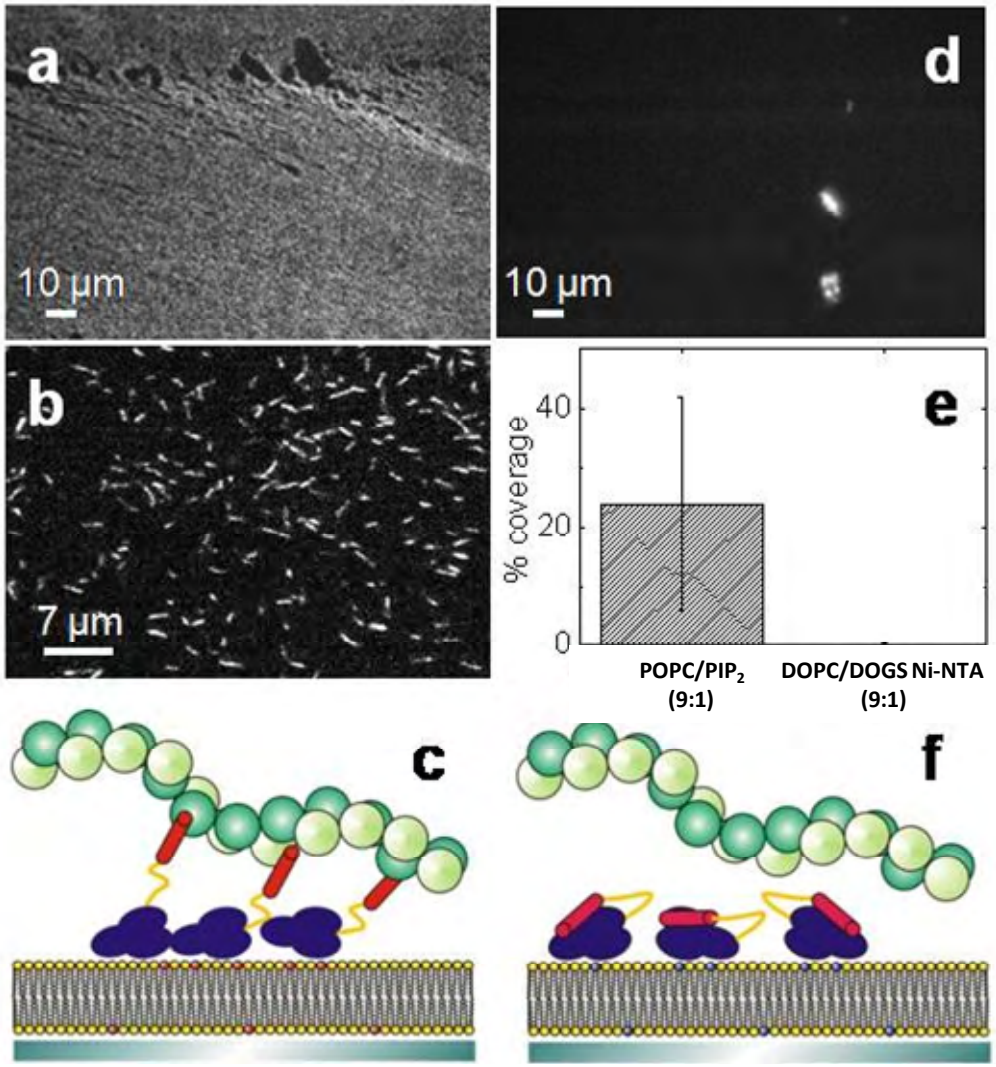


**Figure 23: a)** and **b)** Typical fluorescence images of ezrin bound to POPC/$PIP_2$ (9:1) SSMs, incubated with fluorescently-labeled F-actin. All measurements were performed in F-buffer (20 mM Tris/HCl, 50 mM KCl, 2 mM $MgCl_2$, 1 mM ATP, pH 7.4). **d)** Fluorescence image of a DOPC/DOGS Ni-NTA (9:1) solid-supported membrane, to which ezrin was adsorbed on and incubated with fluorescently-labelled F-actin. **e)** Mean values of F-actin coverage on membrane-bound ezrin calculated by pixel analysis based on light intensity differences. The depicted results for the DOPC/DOGS Ni-NTA (9:1) membrane are taken from 4 independent measurements ($n$ = 15), while for the POPC/$PIP_2$ (9:1) membranes the mean value is based on 5 independent measurements ($n$ = 60). The rather large error is due to the heterogeneous distribution of the F-actin filaments.
Based on these experimental results activation of ezrin due to binding to $PIP_2$ can be assumed as illustrated in **c)**, while binding to DOGS Ni-NTA preserves the inactivated state, leading to a low attraction to actin filaments **f)**.[84]

[84] Epiluorescence measurements were performed and analyzed by Dr. Alexander Herrig and could be reproduced qualitatively in this work.

In relation to the activation mechanism of ezrin, the fluorescence experiments indicated that adhering to $PIP_2$ is sufficient to unmask the actin-binding domain – at least partially. To verify this assumption in a quantitative manner, force distance measurements were conducted.

***Functionalization of the cantilever microspheres with F-actin.*** Adhesion measurements can be carried out with pN resolution using an atomic force microscope. Either an AFM-tip or a colloidal probe can be approached to and retracted from a surface resulting in force distance curves. In this work the cantilever probe had to be functionalized with actin filaments because the yield of successfully functionalized probes was substantially larger if colloidal probes instead of AFM-tips were used. The moderate curvature of the spherical colloidal probes as compared to rather sharp AFM tips allows the unperturbed deposition of fairly stiff macromolecules such as filamentous actin and thus, provides a more reliable and controllable surface functionalization. With a persistence length of 6-17 μm,[85] F-actin can be considered as a rather stiff, rodlike macromolecule. Moreover, as the aim of this work was more focused on mimicking the situation of the cytoskeleton interacting with the bilayer rather than in the mechanics of individual molecules, F-actin coated colloidal probes are more suited for this purpose than conventional AFM-tips.
The different preparation steps of functionalized colloidal probes, detailed in experimental procedures, are depicted in figure 24. A microsphere, glued on the cantilever, was gold-covered to allow for chemisorption of positively charged monolayers of trimethyl ammonium undecanthiol ($AUT^+$). Under physiological conditions, actin is negatively charged (pI ~5.4). Hence, AlexaFluor® 488 phalloidin labeled F-actin was immobilized on the microsphere, by electrostatic interaction. This was confirmed by fluorescence microscopy prior to each force distance experiment (figure 24 d). Figure 24 e) shows an AFM image of actin filaments immobilized on $AUT^+$ functionalized ultraflat (mica-stripped) gold after flushing with buffer solution. A network of actin filaments is observed, confirming that the functionalization procedure using electrostatic interaction between a positively charged self assembled monolayer and negatively charged actin filaments is successful.

[85] Gittes *et al.* (1993); Liu and Pollack (2002); Ott *et al.* (1993); Yanagida *et al.* (1984)

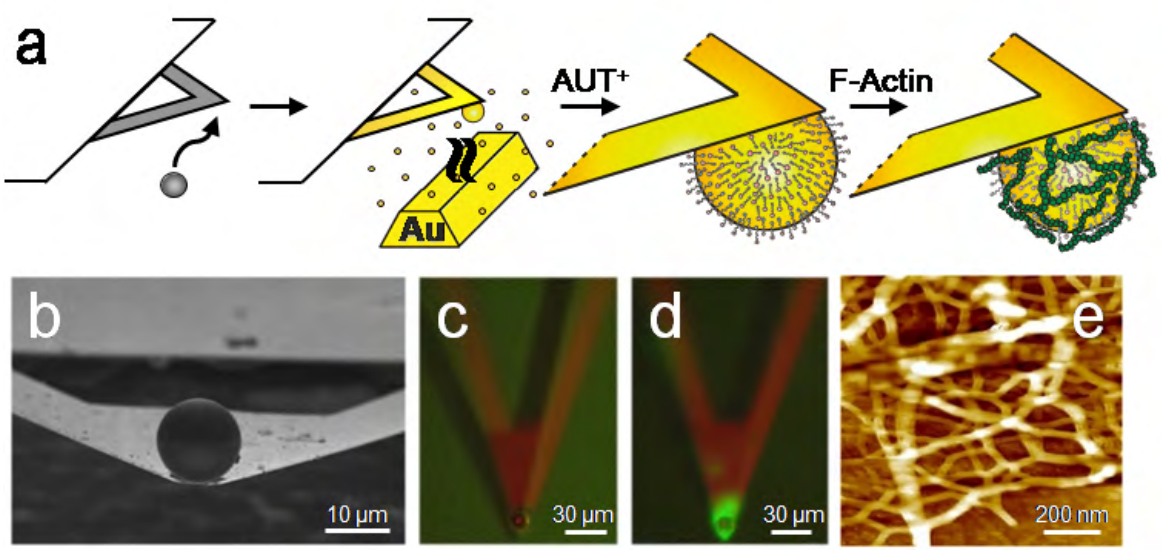


**Figure 24: a)** An illustration of the preparation and functionalization procedure of cantilever-beads. In the first step, a silica microsphere is glued at the end of a cantilever with a micromanipulator. Then, the cantilever-bead is prepared by evaporation with Cr/Au. After functionalization with $AUT^+$ (trimethyl ammonium undecanthiol), actin filaments are attached to the cantilever-bead. **b)** SEM image of a microsphere glued on a cantilever.[86] **c)** Fluorescence image of a gold-covered cantilever-bead before and **d)** after F-actin functionalization. **e)** AFM image showing the topography (tapping mode) of actin filaments on $AUT^+$-functionalized mica-stripped gold in F-buffer solution. The filaments exhibit a height of ~7 nm.

[86] SEM measurements were conducted by Gunnar Glasser (EMZM, MPI-P Mainz).

***Adhesion measurements performed by colloidal probe microscopy.*** Force distance experiments were performed in order to examine the resulting forces of the interaction between actin filaments and membrane-bound ezrin. To obtain a maximum surface coverage with ezrin, solid-supported membranes equipped with 10 mol% of the receptor lipid (POPC/$PIP_2$ 9:1 or DOPC/ DOGS Ni-NTA, 9 : 1) were prepared on hydrophilic, oxidized silicon substrates by fusion of large unilamellar vesicles. Afterwards, ezrin was applied to the bilayer in a concentration of 0.5-1 µM. The colloidal force probes were prepared and functionalized with F-actin as described in the previous section. Prior to force distance experiments, the functionalization of the cantilever-beads were confirmed by fluorescence microscopy and the ezrin-covered membranes were checked by AFM-imaging to ensure a full protein surface coverage of each sample.

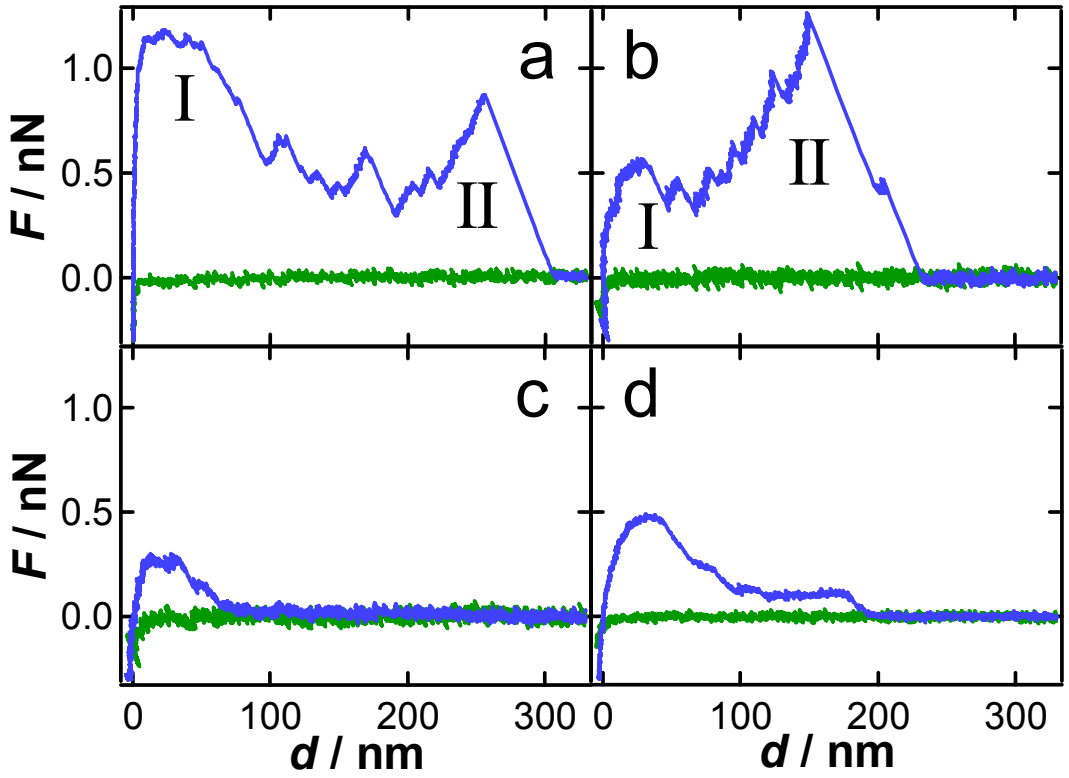


**Figure 25:** Representative force distance curves (green: trace, blue: retrace) for a F-actin functionalized cantilever-microsphere on various surfaces. All measurements were performed in F-buffer, applying a loading rate of 1000 pN/s and a contact loading force of about 200 pN. To enhance the formation of protein-protein interactions, the cantilever remained on the surface for 1 s before retracting. **a/b)** Ezrin bound to a POPC/$PIP_2$ (9:1) SSM. The curves show generally two pronounced maxima, marked as I and II, including single rupture events in the second force maximum. **c/d)** Ezrin associated via its His-tag to a DOGS Ni-NTA containing bilayer. In general, these curves exhibit only maximum very close to the surface, followed by a weak long-range attraction at a constant force level, which abruptly breaks off.

Figure 25 shows typical force distance curves for colloidal probes functionalized with F-actin touching $PIP_2$-bound ezrin monolayers (a, b) and ezrin monolayers coupled via its His-tag to DOGS-Ni-NTA doped SSMs (c, d). The retraction curves (blue) display adhesion phenomena caused by an interaction between the F-actin functionalized colloidal probe and membrane bound ezrin.

Dependent on how ezrin is bound to the membrane, the retraction curves differ in the maximal force, the number of observed rupture events per curve and the cumulative adhesion energy, which is obtained by integrating the force distance curves with respect to the tip-sample distance. Retraction curves obtained from experiments, in which ezrin bound via its His-tag to DOGS Ni-NTA was brought in contact with the colloidal probe typically exhibit the maximum adhesion force close to the surface, followed by a weak long-range attraction at a constant force level, which abruptly breaks off when contact of the molecular bridges is lost. In contrast, retraction curves acquired from ezrin monolayers, bound via $PIP_2$ to the membrane, reveal a large maximum adhesion force in a regime ranging from close to the surface up to 100 nm away from it (I) followed by a sawtooth regime extending beyond $> 100$ nm (II) building up to a substantial adhesion peak. This signature of force distance curves upon retraction is not found for ezrin bound via its His-tag to the DOGS Ni-NTA-containing membrane.

The sawtooth pattern in regime II is characterized by prominent force peaks that are reminiscent of protein unfolding events as observed in single molecule stretching experiments.[87] It is conceivable that in this regime the proteins, most likely ezrin molecules, are stretched until they suddenly unfold and the force immediately decreases as the molecular handle relaxes.

In order to verify and support this assumption, single molecule experiments were intentionally carried out using a conventional AFM tip functionalized with F-actin rather than the microsphere retracting from a $PIP_2$-bound ezrin monolayer (figure 26 a). Single stretching events could be observed as frequently as expected for unfolding of proteins with the typical signature of the nonlinear worm like chain (WLC) model. Fitting an elastic WLC model to the data provides a persistence length of approximately 0.3 - 0.4 nm and is in good agreement with the typical persistence

[87] Janshoff *et al.* (2000)

length found for polypeptide chains.[88] The same model with the same fitting parameters except for the contour length was used to describe the sawtooth events we observed in the force distance curves obtained from functionalized colloidal probes (figure 26 b). The elastic WLC model fits the data well, supporting the hypothesis that in regime II individual ezrin molecules unfold.

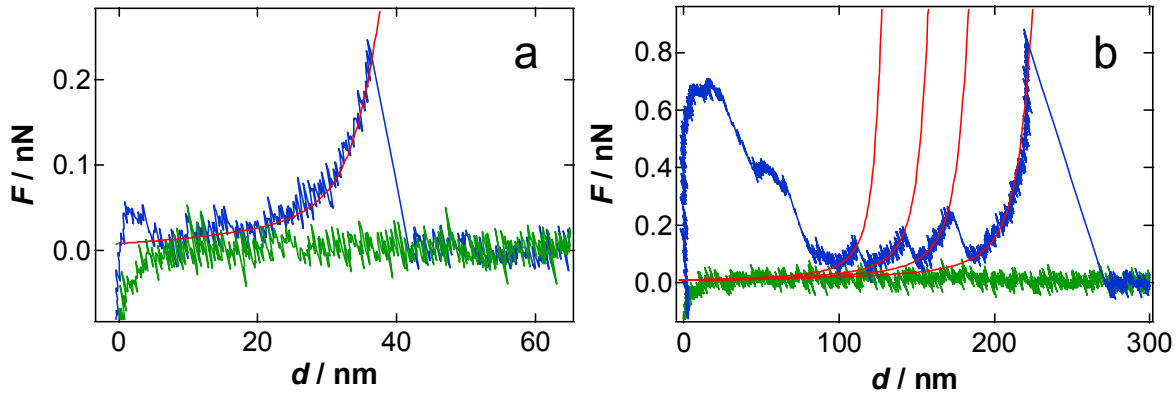


**Figure 26:** Force distance curves (green: trace, blue: retrace, red: elastic worm-like chain fits) for F-actin functionalized probes on an ezrin covered POPC/PIP2 (9:1) SSM. **a)** By using a conventional functionalized AFM tip single non-overlapping adhesion events with a persistence length of 0.3 nm could be observed. **b)** In experiments using functionalized microspheres in some cases non-overlapping peaks could be distinguished, exhibiting a mean persistence length of 0.35 nm. These peaks can be elucidated as single ezrin-actin rupture events.

Figure 27 envisions the possible scenario that might occur if an F-actin coated microsphere is separated from a monolayer of activated ezrin molecules bound to $PIP_2$. Regime I comprises the detachment of the microsphere within the contact area mainly governed by breakage of specific and non-specific non-covalent bonds (figure 27 a). This leads to a sudden relaxation of the cantilever after the first force maximum (figure 27 b). After relaxation, the remaining bonds between actin and ezrin are stronger than the intramolecular forces that are responsible for the folded structure of ezrin, which inevitably leads to stretching followed by unfolding of individual proteins that form bridges between the tip and the substrate (figure 27 c). This gives rise to the observed WLC/sawtooth signature in regime II.

[88] Rief *et al.* (1997)

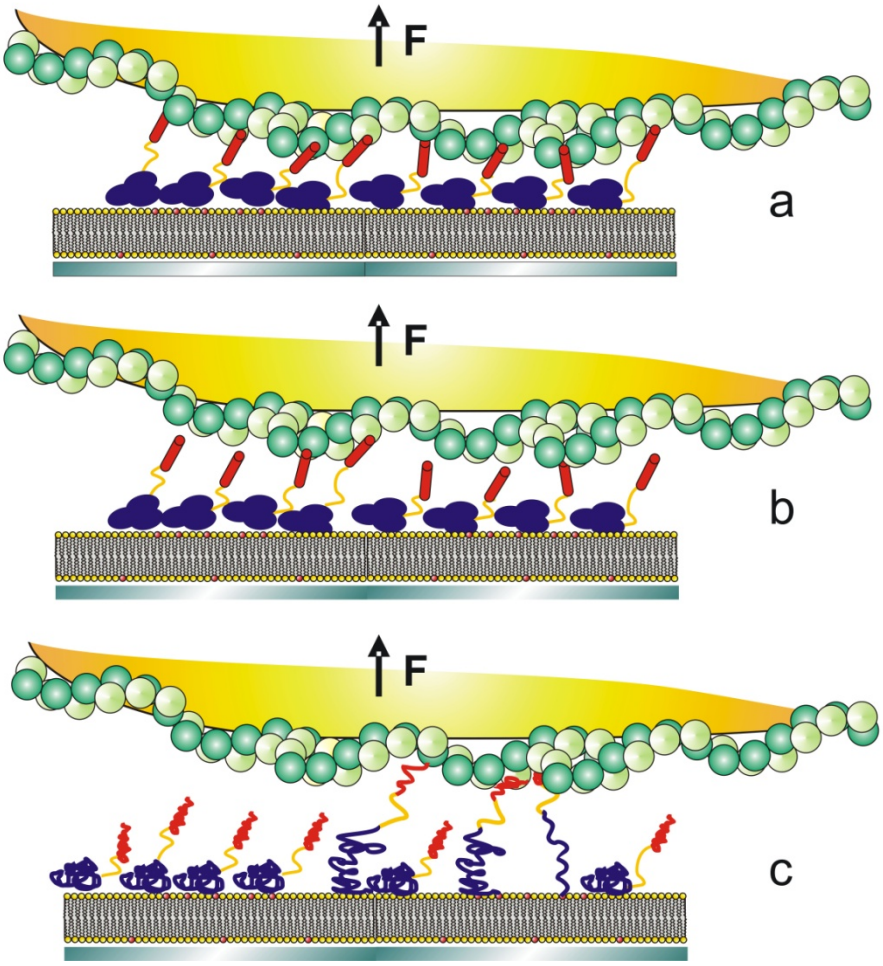


**Figure 27:** Schematic drawing of the adhesion mechanism when retracting a microsphere functionalized with actin filaments from an ezrin covered bilayer containing $PIP_2$ as lipid-anchor.

The retraction of an F-actin coated colloidal probe from a monolayer of ezrin bound via its His-tag to an SSM does only rarely show stretching events that can be attributed to unfolding of individual proteins. The signature of adhesion resembles more on typical desorption curves obtained for peeling off polymers attached to a surface,[89] a behavior that is found for weakly attached macromolecules.

Due to the sharp curvature of the commercial tips, a proper functionalization with F-actin was not highly reproducible and had to be regarded with caution. Still, beyond doubt, the elasticity of ezrin molecules was obtained, whereas information concerning the adhesion strength i.e. the maximal force or cumulative adhesion energy, were refrained due to unsafe functionalization of the tip. However, this information is necessary to reveal the differences in binding capability of ezrin either adsorbed on $PIP_2$ or DOGS Ni-NTA containing SSMs. Hence, only experiments with

[89] Hugel *et al.* (2001)

functionalized microspheres were employed to gather quantitative data on the adhesion strength of F-actin attached to surface bound ezrin.

***Adhesion analysis.*** A comprehensive quantitative analysis of adhesion forces and cumulative adhesion energies of F-actin coated microspheres in contact with monolayers of ezrin either attached to $PIP_2$- or DOGS-Ni-NTA-containing membranes was carried out. Figure 28 summarizes histograms of maximum adhesion forces (figure 28 a-d) and cumulative adhesion energies (figure 28 e-h) found for different surface treatments. Figure 28 a) and e) show the results obtained from retracting F-actin microspheres attached to monolayers of ezrin bound to $PIP_2$ containing membranes on silicon. A broad distribution of maximum adhesion forces with an average value of $(1.32 \pm 0.44)$ nN and cumulative adhesion energies with an average value of $(40 \cdot \pm 18.6) \cdot 10^3$ kT are found. Both average values are significantly larger than those found for experiments, in which F-actin microspheres were retracted from an ezrin monolayer bound to DOGS-Ni-NTA containing bilayers (figure 28 b and f). In this case, the average maximum adhesion force amounts to $(0.45 \pm 0.15)$ nN and the average cumulative adhesion energy reads only $(10.9 \pm 5.9) \cdot 10^3$ kT. Notably, the same F-actin functionalized bead was used for both experiments. Moreover, experiments were conducted in reverse order to ensure that wearout of the actin-coated probe can be ruled out.

Control experiments in the absence of protein-protein-interactions employing non-functionalized microspheres (figure 28 c and g) or a $PIP_2$-doped solid-supported membrane without bound ezrin (figure 28 d and h) resulted in considerably lower adhesion forces and cumulative adhesion energies.

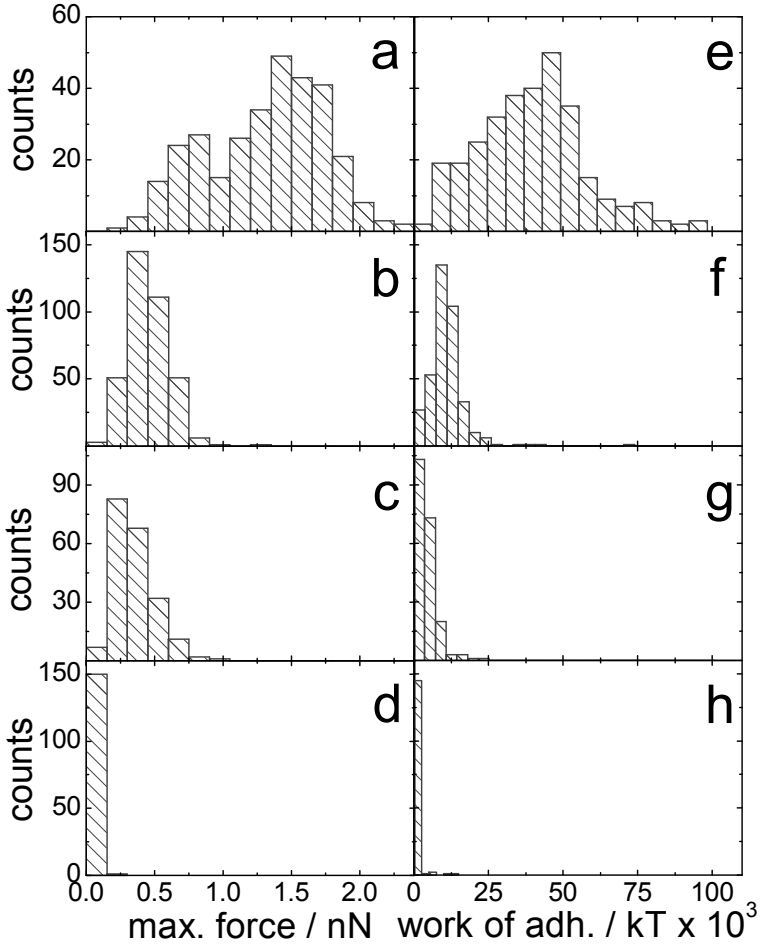


**Figure 28:** Distributions of the maximum adhesion forces **(a-d)** and the cumulative adhesion energies **(e-h)** caused by the interaction between F-actin-functionalized microspheres and different surfaces. **a)** F-actin versus $PIP_2$-bound ezrin (average: (1.32 ± 0.44) nN, *n* = 313). **b)** F-actin versus DOGS-Ni-NTA-bound ezrin (average: (0.54 ± 0.15 nN), *n* = 369). **c)** Non-functionalized microsphere versus $PIP_2$-bound ezrin (average: (0.35 ± 0.01) nN, *n* = 204). **d)** F-actin versus POPC/$PIP_2$-bilayer without ezrin (average: (0.06 ± 0.01) nN, *n* = 151). **e)** F-actin versus $PIP_2$-bound ezrin (average: $(40 \cdot \pm 18.6) \cdot 10^3$ kT, *n* = 313). **f)** F-actin versus DOGS-Ni-NTA-bound ezrin (average: $(10.9 \cdot \pm 5.9) \cdot 10^3$ kT, *n* = 369). (g) Non-functionalized microsphere versus $PIP_2$-bound ezrin (average: $(4.4 \pm 1.1) \cdot 10^3$ kT, *n* = 204). **h)** F-actin versus POPC/$PIP_2$-bilayer without ezrin (average: $(0.3 \pm 1.6) \cdot 10^3$ kT, *n* = 151).

Figure 29 shows a cluster diagram (maximum adhesion force as a function of distance from the surface), which visualizes the conceptual differences observed for force distance curves measured on ezrin monolayers attached either to the membrane via the His-tag to DOGS Ni-NTA lipids or to $PIP_2$. While for $PIP_2$-bound ezrin two force maxima are found, referred to as regime I (open blue dots) and II (open red dots), only one prominent adhesion peak was usually found, if ezrin is bound via its His-tag to DOGS Ni-NTA (solid black dots). Moreover, if ezrin was bound to $PIP_2$, the maximum adhesion forces for both regimes - I and II - as a function of the tip-sample distance are generally higher than those obtained in experiments, in which ezrin was bound via its His-tag to DOGS Ni-NTA, as expected from histogram analy-

sis. Interestingly, regime I is confined to distances below a tip-sample distance of 100 nm and shows a bimodal distribution, while regime II is spread to tip-sample distances of up to 400 nm and does not exhibit any substructure in the force distribution.

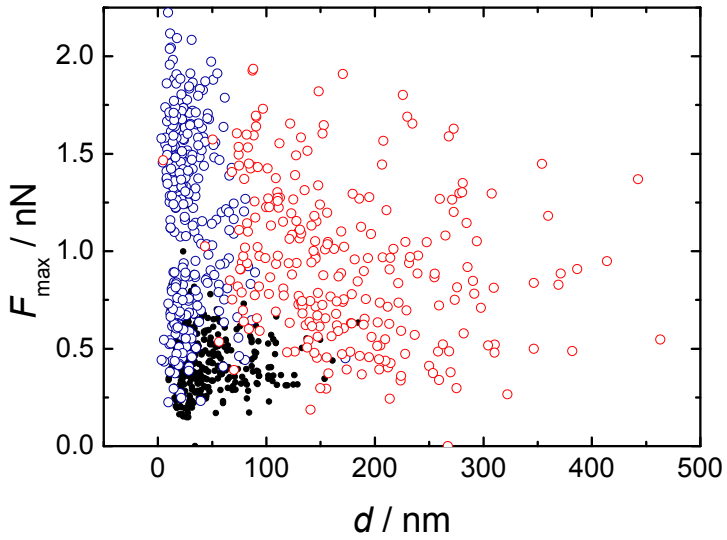


**Figure 29:** Cluster analysis of the force maxima $F_{max}$ as a function of the distance $d$ to the surface. Experiments performed with F-actin versus $PIP_2$-bound ezrin exhibit a force maximum occurring close to the surface, presented as blue circles, with an average maximum force of (1.18 ± 0.48) nN at an average distance of (28.2 ± 19.4) nm. The red circles correspond to dominant force peaks after the first force maximum at greater distances to the surface, exhibiting an average maximum force of (0.94 ± 0.41) nN and a mean distance of (174.7 ± 86.4) nm. Such force peaks are not observed in force distance curves of F-actin versus DOGS-Ni-NTA bound ezrin. These curves only exhibit a maximum adhesion force rather close to the surface, presented as black dots, with an average maximum force of (0.45 ± 0.15) nN at a distance of (45.6 ± 30.8) nm.

***Discussion.*** Ezrin, as a member of the ERM family, is known as a direct linker of the plasma membrane and the actin cytoskeleton. The activation of ERM proteins, resulting in the unmasking of their functional bindings sites, is discussed to occur through conformational changes triggered by events including the binding to $PIP_2$ and the phosphorylation of a conserved threonine in the active binding site of the C-ERMAD (T567 in ezrin). The synergy between these two events in the conformational activation of ezrin is, however, still a matter of debate. While ERM proteins phosphorylated at T567 are localized in membrane extensions rich in actin,[90] cell experiments using ERM mutants, which should mimic the phosphorylated form, gave ambiguous results.[91] *In vitro*, phosphorylation of the C-ERMAD weakens its in-

[90] Hayashi *et al.* (1999); Nakamura *et al.* (1996)
[91] Chambers and Bretscher (2005); Gautreau *et al.* (2000)

teraction with the N-ERMAD.[92] However, even though phosphorylation appears to be required, it is not sufficient for the association of ERM proteins with F-actin *in vitro*.[93] Binding of $PIP_2$ has also been proposed to play an essential role in the conformational activation of ERM proteins. It has been shown that an overexpression of phosphatidylinositol-4-phosphate-5-kinase, responsible for the biosynthesis of $PIP_2$, in mouse fibroblasts and in humane HeLa cells results in a accumulation of ezrin at the plasma membrane and at microvillis.[94] Auvinen *et al.* reported that an upregulation of PIP-kinase leads to a colocalization of activated ERM-proteins and F-actin.[95] Moesin and F-actin cosediment in the presence of $PIP_2$ but not in presence of phosphatidylinositol.[96] The cumulative experimental *in vitro* results of this work provide direct evidence that $PIP_2$ not only serves as a membrane anchor, but in fact is capable of activating ezrin presumably by a conformational switch, which unmasks the F-actin binding site at the C-terminus. In contrast, ezrin is not able to bind F-actin if the protein is attached to a bilayer via DOGS Ni-NTA, in agreement with the notion that the protein remains in its dormant conformation.

To elucidate the specific interaction and adhesion of F-actin with membrane bound ezrin in a quantitative manner, force distance measurements were conducted using colloidal probes. Integration of the force distance curves leads to cumulative adhesion energies that include specific as well as nonspecific interactions between the proteins as well as their elastic behavior. It can be assumed that the nonspecific interactions are discernable very close to the surface (regime I) and partly intermingled with those produced by specific ezrin-actin interactions that occur in both regimes but predominately take place in regime II (Figure 25, page 47) .

Regime I is rather unstructured and it can be assumed that a substantial number of specific and non-specific bonds are formed within the contact area and ruptured upon pulling. The presence of a second regime (regime II) suggests that bridging occurs between probe and sample surface that reflects both bending of actin filaments and stretching of proteins, i.e. ezrin.

[92] Matsui *et al.* (1998); Simons *et al.* (1998)
[93] Nakamura *et al.* (1996)
[94] Auvinen *et al.* (2007); Matsui *et al.* (1999)
[95] Auvinen *et al.* (2007)
[96] Huang *et al.* (1999)

It is, however, unclear how many bonds are formed and strained in either regime. Parallel bonds enhance the effective binding force not only by the shear addition but also by rendering rebinding more probable as pointed out by Li and Leckband.[97] It is conceivable that in the first regime the adhesion force/energy builds up due to many relatively weak parallel bonds that are not sufficiently strong to withstand the unfolding of ezrin molecules. In the second regime only few but stronger bonds are strained giving rise to a sawtooth pattern, which can be attributed to stretching (partly in parallel) of polypeptide chains. When being peeled off from the substrate, proteins such as actin or ezrin usually exhibit a different signature,[98] but it might also contribute to the force distance curve.

Single molecule experiments with conventional AFM-tips functionalized with F-actin display forces > 100 pN (see figure 26 a), which suggest that less than 10 bonds are strained in parallel during the CPM experiments. Considering that F-actin is very stiff, exhibiting persistence lengths far beyond 1 µm, and G-actin does not bind to ezrin, it can be concluded that ezrin is unfolded in the second force regime.

From the histogram analysis it is most obvious that the adhesion energies as well as the maximum adhesion forces are significantly larger if ezrin is bound via $PIP_2$ to the lipid bilayer than nonspecifically attached via its His-tag. This is consistent with the idea that specific interactions between ezrin and F-actin are formed, when the colloidal probe comes in contact with the protein monolayer. These specific interactions can only occur, if a conformational switch of the protein releases the F-actin binding site at the C-terminus. This hypothesis is further backed up by the significant difference in height of the ezrin monolayer depending on the mode of interaction. Ezrin, attached to its native receptor $PIP_2$, displays a smaller height than ezrin bound via the His-tag. This might be indicative of a different conformation, in which ezrin bound to $PIP_2$ is less compact than ezrin attached via the His-tag, as expected from the molecular structure.

While scrutinizing the stability of protein-protein interactions in model systems, side-effects, like extraction of lipid molecules from the membrane have to be considered. Evans *et al.* determined the extraction forces of single biotinylated lipids from 1-stearoyl–2-oleoyl-phosphatidylcholine (SOPC) membranes with a biomem-

[97] Li and Leckband (2006)
[98] Hugel *et al.* (2001)

brane force probe (BFP) decorated with streptavidin.[99] With loading rates similar to those used in this study, they measured forces of about 40 pN per lipid. Here, several thousand $PIP_2$ molecules are underneath the contact radius of the microsphere, assuming a molar ratio of POPC/$PIP_2$ of 9 : 1 and an average molecular area per lipid of 70 $Å^2$. Thus, a concerted extraction of several lipid molecules appears to be unlikely. Another possibility could be the detachment of actin filaments from the microsphere. Control experiments performed with F-actin-coated microspheres on a positively charged trimethyl ammonium undecanthiol functionalized gold substrate showed the largest observed cumulative mean adhesion energy $(60.3 \pm 16.1)\cdot 10^3$ kT. This value is most probably a lower bound of the attachment force between F-actin and an $AUT^+$ functionalized surface, since the F-actin used for probing is already attached to a positively charged surface, i.e. the gold covered colloidal probe. Thus, most of the molecular bonds have already been established and only a minor amount of attachment sites, the negatively charged amino acids, remain for further binding to the planar $AUT^+$ surface. Together with the observation that 100-200 force experiments can be carried out without losing binding strength between the ezrin covered bilayer and the F-actin functionalized bead, it is very likely that indeed the interaction force between ezrin and F-actin has been measured. Notably, even if the adhesion forces are partly diluted by rupture of weaker F-actin – $AUT^+$ bonds, it is safe to say that the adhesion forces between ezrin and F-actin are extremely high and activation of the protein by $PIP_2$ recognition took place. The strength of the F-actin – ezrin contact is further enhanced by the previously described attractive lateral intermolecular interactions of ezrin molecules adsorbed on $PIP_2$-containing bilayers (see chapter 4.2). The ezrin monolayer attached to $PIP_2$ can be regarded as a protein carpet that provides additional strength for the cytoskeleton attachment.

[99] Evans and Ludwig (2000)

# 5 UNFOLDING AND REFOLDING OF NANOCAPSULES AS A NEW PATHWAY OF BIOMIMETIC MODELING

The mechanical properties of macromolecules are an important aspect often neglected in traditional chemistry and biochemistry of bulk solutions. Nevertheless, mechanical stress is involved in many general biological processes like cell adhesion, DNA replication or the motion of muscles.[100] In all these mechanisms, forces act upon single proteins and influence their structural behavior, down to the single bond level. For instance, Fernandez and co-workers investigated the effect of force on the thiol/disulfide exchange, which is an important reaction in the regulation of protein functions. They found that the kinetics of the reduction of disulfide bonds in a modified titin domain is dependent on the applied mechanical force and predicted that any chemical reaction that results in bond lengthening will be force dependent.[101]

Due to the variety and complexity of proteins, the impact of an external load on processes like protein folding and unfolding remains a challenge in current research. One way to address these questions is single-molecule force spectroscopy that enables a detailed view into specific processes of macromolecules like force-induced intramolecular transitions.[102] The central motive for conducting force spectroscopy is assessing information about kinetic and thermodynamic parameters of both, unfolding and refolding processes, influenced by the applied load. To comprehend these conformational transitions more deeply, the mechanisms for breaking and rejoining have to be analyzed in conjunction with each other on single bond level.

Prominent examples of biologically relevant structures that have been studied in the past are the mechanical properties of polysaccharides, nucleic acids, and proteins.[103] Famous research studies were conducted with the oligomerized proteins titin, spectrin, ankyrin, and tenascin. In contrast to other proteins, their functions

[100] Bao and Suresh (2003); Kruse (2007); Maier *et al.* (2000); Sackmann (2004); Welte *et al.* (1998); Wuite *et al.* (2000)
[101] Wiita *et al.* (2006)
[102] Force distance experiments with different loading rates (increase in force per second) are usually referred as (dynamic) force spectroscopy.
[103] Janshoff *et al.* (2000)

could be directly associated with stress induced processes in biology.[104] However, these molecules are still under investigation and their transition processes, occurring during stretching and relaxing, cannot yet be described entirely by theoretical models. Inherently, in most force distance experiments rupture events occur under nonequilibrium conditions, i.e. the probability of rebinding is extremely small if the binding partners are substantially separated.

Noteworthy, the unfolding and refolding kinetics of RNA hairpins were successfully investigated by using optical tweezers.[105] The experimental data could be related to thermodynamic parameters like free-energy differences by the application of fluctuation theorems, based on Jarzynski's equation.[106] Thereby, an experimental bridge between equilibrium and non-equilibrium processes, providing a test bed for fundamental physics, was established on single-molecule level.[107]

In single protein unfolding/refolding studies, however, the refolding process is not distinguishable in a sufficient manner for further interpretation due to the natural asymmetry of the potential and the limited time range of the experiments.

Furthermore, correct data interpretation of force spectroscopy experiments of a protein, which exhibits a natural heterogeneous mixture of mechanically active modules, can be difficult. Even elementary assignment of individual domains of a protein to the characteristic sawtooth pattern in the experimentally obtained force curves is complicated.

Hence, an understanding of the rupture and rebinding mechanisms on single bond level is hardly possible due to the multiplicity and complex interplay of the molecular interactions. So far, only a few examples are known, which provided a detailed view into the mechanism of force induced transitions of modular proteins.[108]

In the case of a small protein, named ubiquitin, the refolding trajectory was, for the first time, successfully monitored by force-clamp spectroscopy at low forces (10-40 pN) over a time range of about 5-8 s. Instead of a sudden all or none reaction, as observed in classical chemical denaturation experiments, refolding was characterized

[104] Lee *et al.* (2006); Oberhauser *et al.* (1998); Rief *et al.* (1997); Rief *et al.* (1999)
[105] Manosas *et al.* (2006); Onoa *et al.* (2003)
[106] Crooks (1999); Jarzynski (1997); Karevski (2006)
[107] Collin *et al.* (2005)
[108] Dietz and Rief (2004); Li *et al.* (2005); Mickler *et al.* (2007); Schwaiger *et al.* (2002)

as a continuous process, marked by large fluctuations, which led to a still ongoing debate.[109]

Therefore, simplified model systems are needed to investigate the fundamental physics behind breaking and rebinding of single bonds in a supramolecular environment subject to external mechanical load. Of special interest are hydrogen bonds, because they play an essential role in secondary structure formation of proteins and in molecular recognition processes. So far, only few model systems are available to approach these issues, e.g. Vancso and co-workers investigated the complementary recognition of hydrogen bonded supramolecular 2-ureido-4[1H]-pyrimidinone (Upy) polymers by means of force spectroscopy. They measured rupture forces of single Upy−Upy complexes but could not detect the rebinding due to the irrevocable distinct separation of the binding partners.[110]

In the present work, breaking as well as rebinding of intramolecular hydrogen bonds could be scrutinized with the help of a novel biomimetic system, displaying a rationally designed and mechanically interlocked molecular architecture. Hence, oligomerized bis-loop tetra-urea calix[4]arene-catenanes were designed by Dr. Yuliya Rudzevich exclusively for AFM force distance experiments to mimic the concerted unfolding and refolding processes of more complex structures like proteins.[111] Rebinding of the "unfolded" nanocapsules into dimers was only possible due to the entangled structure that kept the capsules intact in an elongated state after the breakage of the intramolecular hydrogen bonds between urea-functions. The loop length of this entanglement was adjustable during the synthesis and was optimized for the detection of reversibility on the timescale of experimental observation via AFM.

The experimental data was supported by molecular dynamics (MD) simulation and mathematical modeling, based on Kramers' theory,[112] performed by Dr. Thorsten Metzroth and Prof. Dr. Gregor Diezemann, In order to better understand the me-

[109] Fernandez and Li (2004)
[110] Zou *et al.* (2005)
[111] Dr. Y. Rudzevich, group of Prof. Dr. V. Böhmer, Institute of Organic Chemistry, Johannes-Gutenberg University of Mainz.
[112] Kramers (1940)

chanism of hydrogen bond rupture.[113] By using this combination of experiment and theory, a model of the energy landscape of a calixarene dimer, held together by hydrogen bonds, could be proposed.

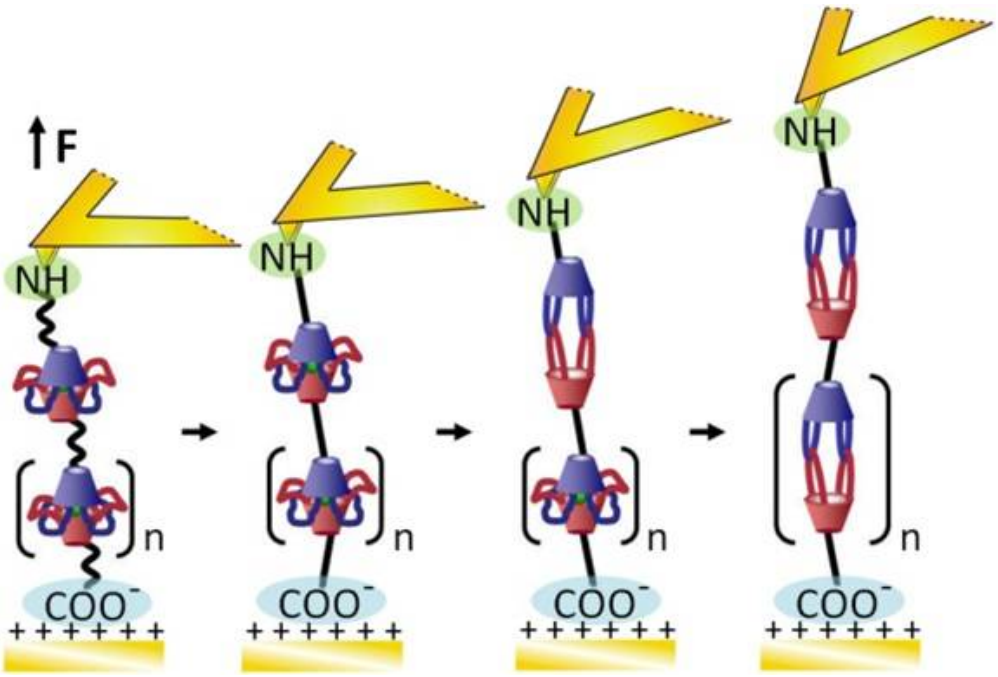


**Figure 30:** Schematic representation of the single-molecule AFM experiment.

To become acquainted with calixarenes, first their properties and functions are highlighted in this chapter, followed by an experimental example of their capability to self-associate. In this example, non-covalently bridged calixarene-polymers were visualized by AFM to prove their capability to self-assemble via intermolecular hydrogen bridges, as shown in section 5.2.

The main subject of this chapter consists of theory of single bond rupture under external load, force distance experiments and simulations of stretching and contraction of bis-loop tetra-urea calix[4]arene-catenanes.

[113] MD simulations were performed by Dr. T. Metzroth and the stochastic modeling was conducted by Prof. Dr. G. Diezemann, both are members of the group of Prof. Dr. J. Gauß, Institute of Physical Chemistry, Johannes-Gutenberg University of Mainz.

## 5.1 Calixarenes: Properties & Functions

***Basic aspects of calixarenes.*** Cyclic oligomers in which four, six or eight phenol units are joined by methylene bridges are called calix[4, 6 or 8]arenes. Inspired by the cup-like shape of these macrocycles, the first part of the name "calixarene" originates from the latin "calix", or "chalice", and the latter part, "arene", derives from the benzene containing scaffolds.

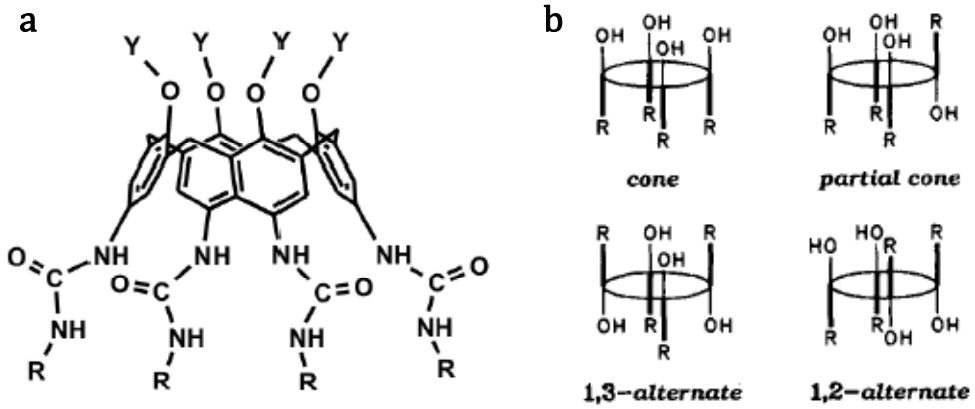


**Figure 31: a)** A calix[4]arene derivative exhibiting urea functions at the wider rim. The cup-like structure is clearly visible. **b)** Basic conformations of a calix[4]arene.

When not sterically hindered, calixarenes exist in different conformations due to rotation around the methylene bridges. E.g., in calix[4]arenes four up-down conformations exist: cone, point group $C_{2v}$,$C_{4v}$, partial cone $C_s$, 1,2 alternate $C_{2h}$, and 1,3 alternate $D_{2d}$.[114]

Usually, the cone conformation is stabilized by hydrogen bonding between hydroxyl groups at the rim of the macrocycles as illustrated in figure 31. Calixarenes exhibit very high melting points (often above 300 °C, sometimes even above 400 °C) and a low solubility in standard solvents.[115] However, these properties can be changed by implementation of functional groups at the wide "upper rim" and narrow "lower rim".

Driven by intermolecular hydrogen bond formation, calixarenes tend to self-assemble into dimers, consisting of two bridged calixarene-units. The internal volume and environment of the cavities inside the capsules can be adjusted by adequate synthesis to accommodate specific small molecules or ions. Thereby access to a huge variety of host-guest complexes is granted, paving the way to artificial, bio-

[114] Böhmer (1995); Gutsche (1989)
[115] Danil de Namor (1993)

mimetic catalysts that are efficient to synthesize, highly stable and exhibit similar catalytic functions as enzymes by providing preorganization of the catalytic group. Calixarenes are suitable for biochemical recognition and separation by binding selectively amino acids, peptides, proteins, saccharides, and other guests.[116] Thus, these compounds can be used in sensor techniques, as catalysts in industrial synthesis, and as HPLC column material.[117]

Today, the propensity to form host-guest complexes as well as the tendency to arrange into self-associated assemblies are of special interest and represent the current challenges in the broad research field of calixarenes which ranges from novel synthesis approaches to innovative ways of their analysis for a better comprehension of superstructures. E.g. Eckel *et al.* investigated the dissociation of different ammonium derivatives from resorc[4]arene-complexes by single molecule atomic force microscopy, finding binding constants between $10^{-5}$ M (ammonium) and $10^{-7}$ M (trimethylammonium).[118]

In this work, calixarenes are of particular interest as they represent simplified analogues of natural proteins and enzymes. Intramolecular transitions like protein folding can be mimicked and better understood by the application of structural model systems like calixarene-derivates, as described in chapter 5.4.

Besides intramolecular mechanisms, intermolecular interactions that induce self-assembly processes are of special interest. Hence, in another synthesis approach, calixarenes were designed to be able to self-associate into supramolecular polymers by the formation of intermolecular hydrogen-bridges. This concept of noncovalently bridged calixarene-polymers could be imposingly confirmed by scanning force microscopy in chapter 5.2.

[116] Ludwig (2005); Zadmard and Schrader (2006)
[117] Purse *et al.* (2005); Thallapally *et al.* (2005)
[118] Eckel *et al.* (2005)

## 5.2 Experimental results & discussion: Imaging of self-assembled bis-tetra-urea calix[4]arenes

The intramolecular self-organization of macromolecules (e.g. the folding of peptides) as well as the intermolecular self-assembly of smaller molecules into highly ordered structures are major subjects in supramolecular chemistry.[119]

As an example for intermolecular self association via hydrogen bonding, the formation of tetra-urea calixarene dimers in apolar solvents has already been studied in detail previously.[120] These dimers are based on a belt of intermolecular hydrogen bonds of the urea residues that are attached to the wide rims of the calixarene counterparts. The cavity of the capsule-like dimers contains usually a solvent molecule as a guest. The only example in which linked bis-calixarenes formed a discrete assembly via their wide rim was described by Rebek *et al.*[121] These connected calixarenes formed unimolecular capsules by intramolecular dimerisation in apolar solvents, as shown by complexation studies.

However, when two tetra-urea calix[4]arenes are connected via their wide rims by a rigid spacer group, their intramolecular dimerisation can be prevented entirely and self-assembly in apolar solvents might result in the formation of supramolecular polymers. Like single tetra-urea dimers, the polymers formed from bis-calixarenes are able to include adequately sized molecules or cations. The inclusion of neutral guests like para-difluorobenzene (F-Ph-F), which is known to be a "better" guest for tetra-urea dimers than chloroform, potentially stabilizes the capsules and hence the formation of supramolecular assemblies.

Here, AFM imaging was implemented to determine the arrangement of self-assembled bis-tetra-urea calix[4]arenes in detail.[122] The molecules under investigation were synthesized by Dr. Ganna Podoprygorina and spin-coated on HOPG for AFM imaging as described in chapter 2.3.[123]

[119] Menger (2002)
[120] Davis and Spada (2007); MacGillivray and Atwood (1997); Vickers and Beer (2007)
[121] Brody *et al.* (1999)
[122] Podoprygorina *et al.* (2008)
[123] Dr. G. Podoprygorina, group of Prof. Dr. V. Böhmer, Institute of Organic Chemistry, Johannes-Gutenberg University of Mainz.

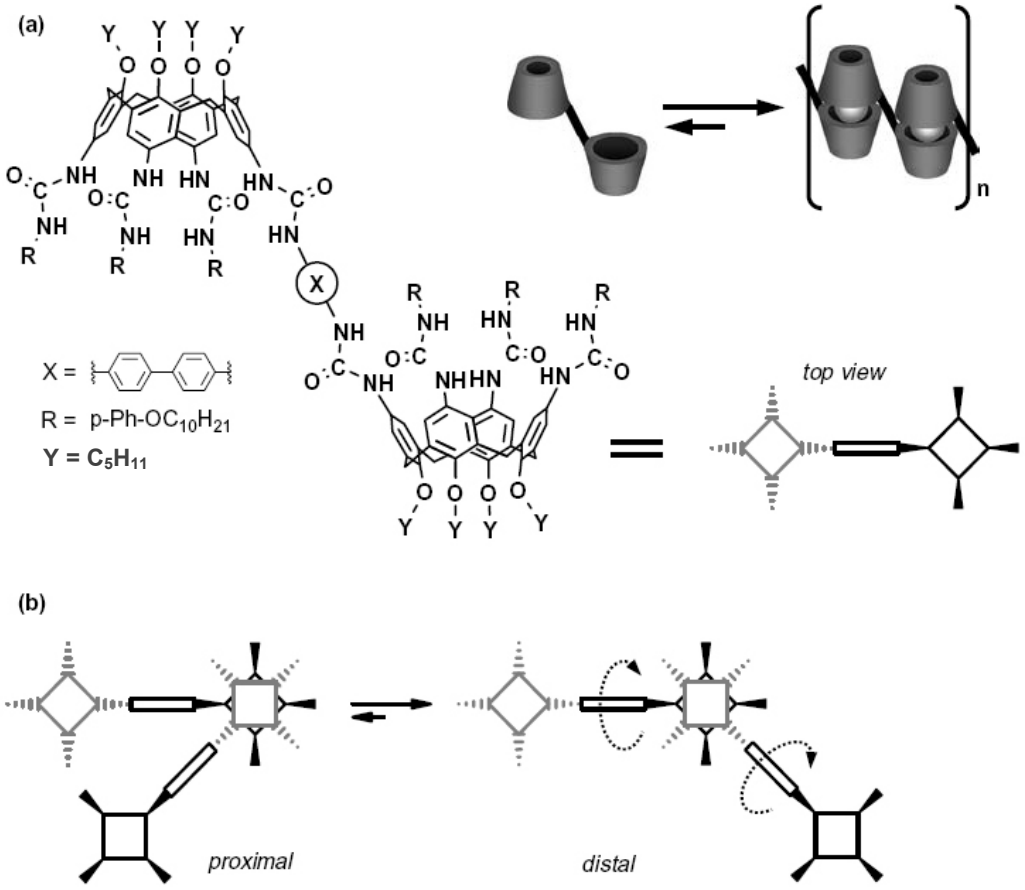


**Figure 32:** Schematic of the dimerisation of bis-tetra-urea calix[4]arenes.

As illustrated in figure 32 b), in a dimeric assembly of two bis-calixarene molecules, the hydrogen bonded tetra-urea counterparts are turned by an angle of 45 ° around their common axis with respect to each other. Thus, the other two dimerisation sites are arranged at an angle of 45 ° (proximal) or 135 ° (distal), as illustrated schematically in Figure 32 b). From these possibilities, the distal arrangement should be strongly favored, since it is sterically less hindered than the proximal one. If by additional reversible intramolecular interactions one direction for this 135 ° kink could be favored, the formation of helical segments (figure 33 b), instead of a stretched conformation (figure 33 a), could occur in an ideal case.

In order to visualize the self-assembly of these calixarenes into polymers and to determine their exact structure, AFM imaging was conducted.

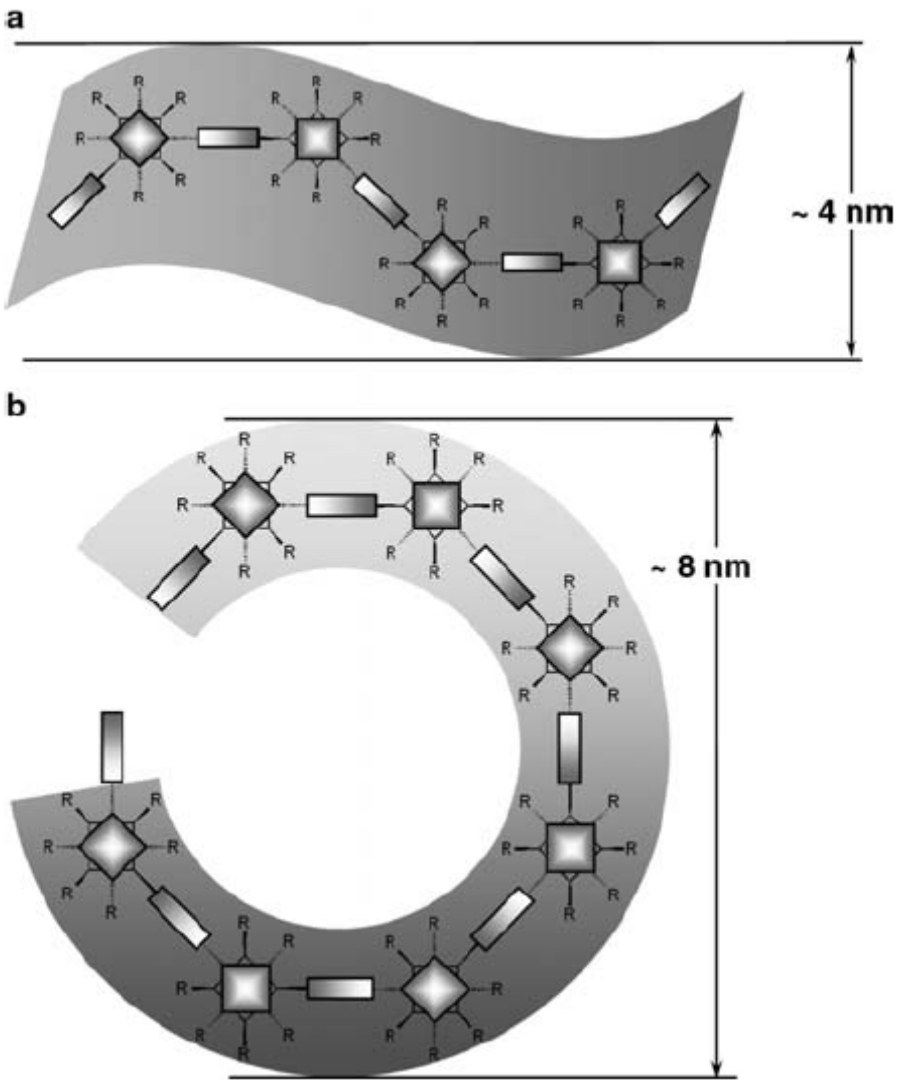


**Figure 33:** Idealised representation of a polymeric assembly. **a)** in a "stretched" arrangement, with alternating 135 ° kinks, or **b)** in a 'helical' arrangement with 135 ° kinks in one favored direction.

The formation of self-assembled calixarene superstructures was confirmed by AFM imaging of calixarene samples as shown in figure 34. The images revealed a coexistence of rod-like and amorphous structures, probably representing highly as well as less-ordered bis-calixarene arrangements. According to average cross sections of AFM height images, the fibers exhibited a width of 16 $\pm$ 2 nm and a height of 1.8 $\pm$ 0.2 nm for the pure chloroform solution and a width of 13 $\pm$ 2 nm and a height of 2.5 $\pm$ 0.2 nm for chloroform solution containing 5 % p-difluorobenzene as an additive. This finding is particularly interesting since it is known that difluorobenzene is a preferred guest molecule. Hence, it can be concluded that the inclusion complex modulates either the structure, e.g. its height, or the elastic properties of the calixarene polymers.

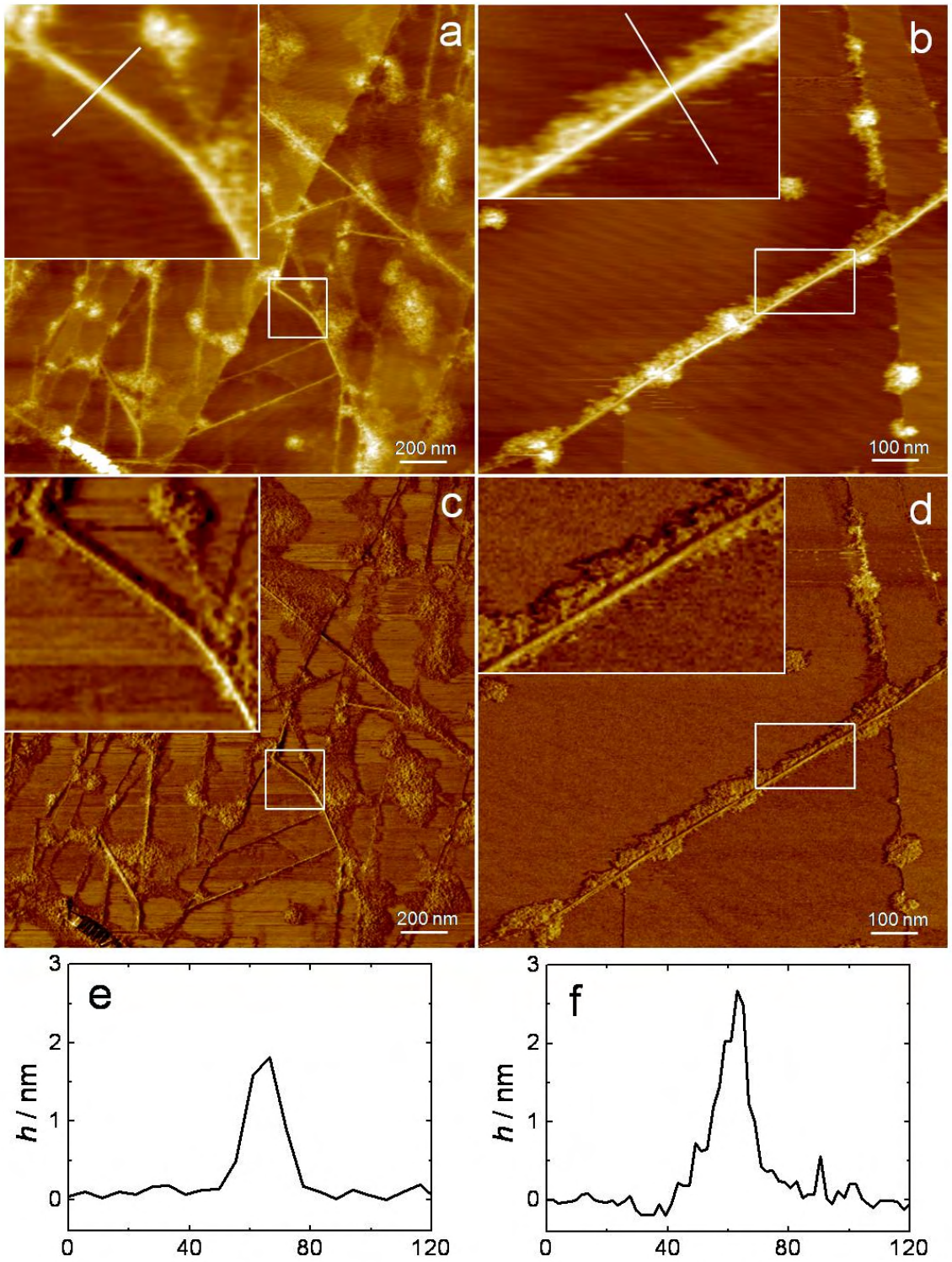


**Figure 34: (a, b)** AFM height and **(c, d)** phase images of the bis-calixarene on HOPG prepared by spin-coating of solutions *c* = 0.01 mg/ml. **a)** $CHCl_3$, **b)** $CHCl_3$ + 5% p-difluorobenzene, **c)** $CHCl_3$, **d)** $CHCl_3$ + 5% p-difluorobenzene, **e)** cross-section along the line shown in a), **f)** cross section along the line shown in b).

The AFM images infer that the highly ordered polymers adopt a rather stiff conformation displaying straight structures over several micrometers. The reasons for this arrangement lie in either the polymeric structure or the underlying graphite lattice directing the adsorption of the polymer. The latter reasoning is supported by the 60 and 120 ° angles sometimes observed for the adsorbed straight polymers.

The analysis of the AFM images indicate that the band structure is the preferred superstructure (figure 33 a). This statement can be reasoned as follows: from the height analysis it can be concluded that the superstructure adopts a rather flat conformation exhibiting a height of 1.8–2.5 nm, depending on the guest molecule. The minimal width of the polymer strands, as extracted from high-resolution phase imaging, was found to be between merely 7 and 8 nm. This value is an upper limit due to the finite size of the tip. Assuming preservation of the volume which would imply either a greater height (approximately 8 nm) or, in the case of severe flattening of the structure on the surface, a substantially greater width, the occurrence of a helical superstructure on the surface can be safely ruled out. Such a structure would require for both, height and width, a minimum dimension of about 8 nm.

These results show that the usual self-assembly of tetra-urea calix[4]arenes is not hindered by the spacer. Moreover, by adopting the rigid spacer, noncovalently bridged calixarene-polymers are accumulated and could be visualized by AFM. A distal arrangement within the dimeric capsules seems likely, and may be further favored by bulky substituents at the two adjacent urea functions. In the future, interactions between additional functional groups could be used to favor, for instance, a helical over a stretched arrangement of adjacent dimeric capsules along the polymeric chain.

## 5.3 Single-molecule force spectroscopy: Theroretical considerations

Protein folding and unfolding *in vitro* is usually observed via spectroscopic measurements of structural transitions, induced by heat or chemical denaturants like urea.[124] However, large changes in temperature or the presence of chemical denaturants are artificial denaturation techniques that strongly differ from protein unfolding processes in living cells. A smart way to enforce unfolding of proteins in a natural manner is force spectroscopy, since mechanical work and mechanical stretching occur in living cells as well. In addition, force spectroscopy provides insight into the energy landscape of a single-molecule with the advantage of a defined reaction coordinate by imposing the folding direction along the trajectory of the AFM cantilever.[125]

Single-molecule force spectroscopy experiments facilitate the examination of intramolecular transitions under non-equilibrium conditions and are therefore not directly comparable to classical, ensemble averaged calorimetry experiments, which enable an investigation of binding or folding energies under equilibrium conditions. In general, real life biochemical interactions occur inherently under non-equilibrium conditions.

This section deals with the theoretical background of single-molecule force spectroscopy, which is required to understand the experimental results, the mathematical modeling, and simulations.

***Polymer models.*** Proteins or synthetic long-chain macromolecules in solution exhibit a large number of conformations resulting in a compact structure due to a maximized entropy in the non-stressed condition. When the molecule is stretched, a counterforce evolves due to enthalpic (changes of bond angles and lengths) and entropic (confinement of the configuration possibilities) reasons. Independently of the microscopic mechanism, the force of a molecule that is stretched in the $x$ direction under isothermal conditions can be expressed as follows:[126]

$$F = \left(\frac{\partial A}{\partial x}\right)_T = \left(\frac{\partial U}{\partial x}\right)_T - T\left(\frac{\partial S}{\partial x}\right)_T \approx -T\left(\frac{\partial S}{\partial x}\right)_T \tag{11}$$

[124] Fong *et al.* (1996); Jacob *et al.* (2004); Plaxco *et al.* (1997)
[125] Carrion-Vazquez *et al.* (1999)
[126] Treloar (1975)

(12) $$F = -kT \left(\frac{\partial ln Z_r}{\partial x}\right)_T$$

When the free Helmholtz energy $A$ is expressed by the internal energy $U$ and entropy $S$, the first term represents the enthalpic contribution and the second term corresponds to the entropic contribution to the counterforce $F$. With respect to statistical thermodynamics, the counterforce can be expressed by the configurational partition function $Z_r$ for a clamped chain.

If the elongation of the molecule is smaller than the contour length $L$,[127] the reduction in entropy contributes mainly to the counterforce. In this case, the derivative term of the internal energy can be neglected and the force is proportional to the temperature.

To describe the force distance behavior of molecules analytically, mathematical models from statistical mechanics have to be fitted to the experimental data. From a wide number of available fit functions two models have to be pointed out:

***Freely jointed chain model (FJC).*** In Flory's freely jointed chain model the molecule is divided in $n$ rigid elements with the same length $l_k$, which is known as the Kuhn length.[128] The rigid segments are connected end to end in a flexible manner without any long-range interactions. For a large number of stiff elements, as under typical experimental conditions, the following expression can be obtained:

(13) $$F(x) = \frac{k_B T}{l_K} \mathcal{L}^{-1}\left(\frac{x}{L}\right),\ \mathcal{L} = \coth\left(\frac{F l_K}{k_B T}\right) - \frac{k_B T}{F l_K}$$

with: $\mathcal{L}^{-1}$ , the inverse Langevin function.

The FJC model conceives only the entropic contribution to the counterforce and can be extended approximately by an additional enthalpic term for large elongations ($x \sim L$). The model is often used to describe the mechanical properties of oligonucleotides or polysaccharides.[129]

[127] The contour length $L$ of a polymer chain is its length at maximum physically possible extension.
[128] Flory (1969)
[129] Marszalek *et al.* (1998)

***Wormlike chain model (WLC).*** In the model of Kratky and Porod, the molecule is described as a homogeneous, non-segmented chain with a steady curvature.[130] In the classic model two parameters describe the properties of the chain: the contour length $L$ and the persistence length $l_p$. The official IUPAC description of the persistence length reads: "The persistence length equals the average projection of the end-to-end vector on the tangent to the chain contour at a chain end in the limit of infinite chain length."[131] At low forces the persistence length is one half of the Kuhn length. Typical values for the persistence length of macromolecules of different composition range from $l_P \sim 0.4$ nm for globular proteins or polypeptides to $l_P \sim 50$ nm for rather stiff DNA-molecules.

The standard WLC model describes the effects of stretching long-chain molecules only accurately to a force level of about 50 pN. Beyond that force an additional parameter $\Phi$, which expresses the specific stiffness of the molecule, has to be implemented. $\Phi$ is independent of the contour length and can be derived from the spring constant of the entire chain: $k = \Phi/L$; thus, the specific stiffness features the unit of a force. Depending on the properties of the molecules under investigation, typical values for $\phi$ are between 4 nN and 28 nN.[132]

$$F(x) = \frac{k_B T}{l_P}\left[\frac{1}{4}\left(1 - \frac{x}{L} + \frac{\boldsymbol{F}}{\boldsymbol{\Phi}}\right)^{-2} + \left(\frac{x}{L}\right) - \left(\frac{\boldsymbol{F}}{\boldsymbol{\Phi}}\right) - \frac{1}{4}\right] \tag{14}$$

Here, the elastic extension of the "non-elastic" WLC model is emphasized. Until today, various attempts have been made to improve and verify the WLC fitting procedures of experimental data.[133] The (elastic) WLC model is nowadays one of the most frequently applied polymer models to perceive the mechanical properties of proteins, DNA, and synthetic polymers by force distance experiments. It was used in this work as well as a fitting procedure to extract the mechanical characteristics of the molecules investigated.

[130] Kratky and Porod (1949)
[131] IUPAC Compendium of Chemical Terminology, 2nd edition (1997)
[132] Hugel *et al.* (2001); Netz (2001)
[133] Bouchiat *et al.* (1999); Marko and Siggia (1995)

***Force dependency of single molecule thermodynamics and kinetics.***[134] As stated in the first law of thermodynamics the change of the internal energy $\mathrm{d}U$ of a clamped molecule is the sum of its dispensed thermal energy $\mathrm{d}Q$ and reversible work $\mathrm{d}W_{\mathrm{rev}}$. The mechanical work of the cantilever and the pressure volume work correspond to $\mathrm{d}W_{\mathrm{rev}}$.

$$\mathrm{d}U = \mathrm{d}Q + \mathrm{d}W_{rev} = (T\mathrm{d}S) + (-P\mathrm{d}V + F\mathrm{d}x) \tag{15}$$

Equation (15) can be transformed via Legendre transformation into the Gibbs free enthalpy $G$ ($G = H - TS$; $H = U + pV$).

$$\mathrm{d}G = -S\mathrm{d}T + V\mathrm{d}p + F\mathrm{d}x \tag{16}$$

At constant temperature and pressure the required work for stretching a molecule by a length of $\Delta x$ is identical with the change of the Gibbs free energy $\Delta G$, if no intramolecular transition occurs (no spontaneous increase in length during stretching) and if the process of investigation is reversible:

$$\Delta G = \int_{x_0}^{x_0+\mathrm{d}x} F\mathrm{d}x \tag{17}$$

Thus, if the stretching process is reversible $\left(\int_{x_0}^{x_0+\mathrm{d}x} F\mathrm{d}x = F\int_{x_0}^{x_0+\mathrm{d}x}\mathrm{d}x\right)$, the difference in free energy by stretching a molecule can be obtained by integrating a force distance curve. In the case of stretching a two state molecule with the folded state $A$, the unfolded state $B$, and the distance $\Delta x_{A\to B}$ between the two states, the change in energy is composed of:[135]

$$\Delta G_{A\to B}(F) = -F\Delta x_{A\to B} + \Delta G_{A\to B}^{irrev}(F) + c \tag{18}$$

With: The reversible work $F\Delta x_{\mathrm{A\to B}}$.
The irreversible contribution $\Delta G_{A\to B}^{irrev}$ is conform with the difference of the stretching work of the molecule in state $A$ and $B$ corresponding to equation (17).

$$\Delta G_{A\to B}^{irrev} = \int_{x_A}^{x_B} F\mathrm{d}x - \int_{x_B}^{x_A} F\mathrm{d}x \tag{19}$$

[134] Tinoco Jr and Bustamante (2002)
[135] Schwaiger (2005)

Due to the constraint $\Delta G_{A\to B}\,(F=0) = \Delta G^0_{A\to B}$ the constant $c$ results in $c = \Delta G^0_{A\to B}$, equation (18) results in:

$$\Delta G_{A\to B}(F) = -F\Delta \mathrm{x}_{\mathrm{A}\to\mathrm{B}}(F) + \Delta G^{irrev}_{A\to B}(F) + \Delta G^0_{A\to B} \tag{20}$$

The external force $F$ tilts the energy potential and thus reduces the energy barrier as illustrated in figure 35.

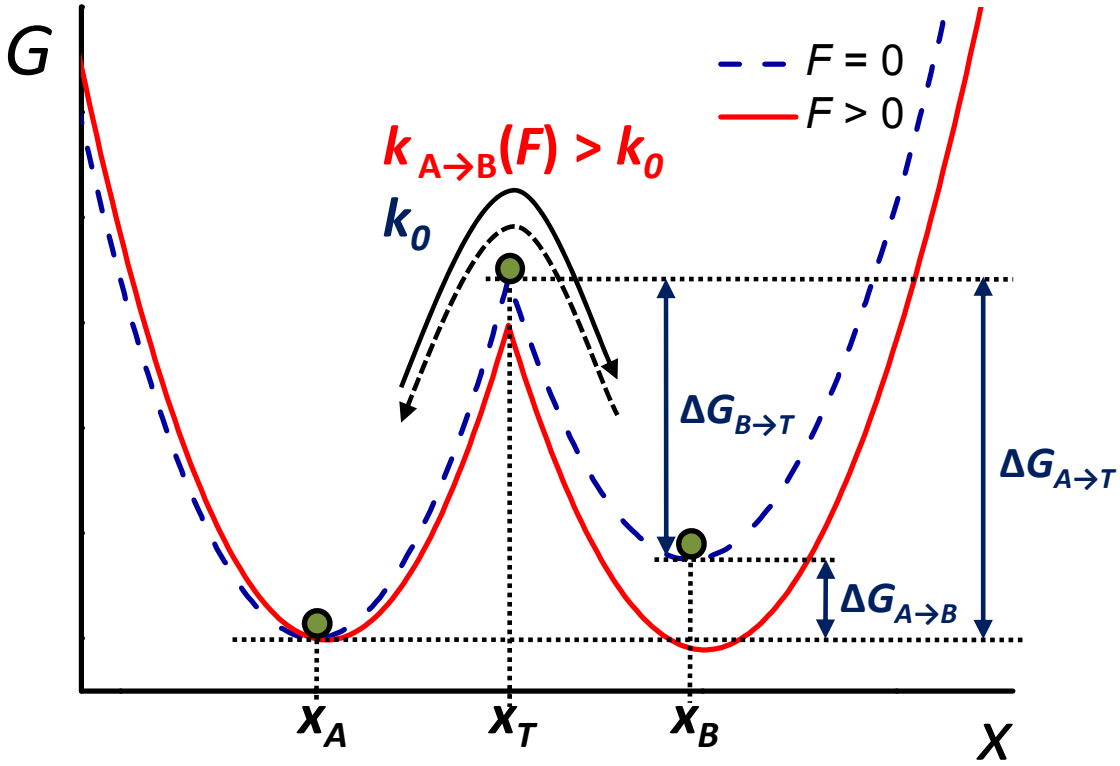


**Figure 35:** A two state potential with (red line) and without (dashed blue line) external load. The applied force $F$ decreases the barrier height $\Delta G_{A\to T}$ by $Fx$. The reaction coordinate $X$ corresponds approximately to the elongation of the stretched molecule.

To calculate the rate constant $k^0_{\mathrm{A}\to\mathrm{B}}$ for crossing the transition barrier in a first approximation the Arrhenius equation is used.

$$k^0_{A\to B} = \nu_0 \exp(-\Delta G^0_{A\to T}/k_B T),\; k^0_{B\to A} = \nu_0 \exp(-\Delta G^0_{B\to T}\,/\,k_B T) \tag{21}$$

With the energy barrier of the transition state ($\Delta G^0_{A\to T}$) and the frequency of a bond ($\nu_0$) (the reciprocal of a diffusive relaxation time). By attempting equation (20) a force dependency of the transition rate can be obtained approximately.

$$k_{A\to B}(F) = \nu_0 \exp\left(-\left(\Delta G^0_{A\to T} - F(x_T(F) - x_A(F)) + \Delta G^{irrev}_{A\to T}(F)\right)/\,k_B T\right) \tag{22}$$

This approach to obtain force-dependent transition rates was first used by Bell.[136] The simple, linear reduction of the free enthalpy of the transition state by the external force is valid for following approximations:

$x_T(F) - x_{A,B}(F) \approx x_T(F=0) - x_{A,B}(F=0) = \Delta x^0_{A,B\to T}$ and $\Delta G^{irrev}_{A\to B} \approx 0$.

Thus, experiments exhibiting small elongations and small pulling speeds can be treated in this manner, leading to the following expressions:

$$k_{A\longrightarrow B}(F) = \nu_0 \exp\left(-\left(\Delta G^0_{A\to T} - \frac{F\Delta x_{A\to T}(F)}{k_B T}\right)\right) = k^0_{A\longrightarrow B}\exp\left(\frac{F\Delta x_{A\to T}}{k_B T}\right) \quad (23)$$

$$k_{B\longrightarrow A}(F) = \nu_0 \exp\left(-\left(\Delta G^0_{B\to T} - \frac{F\Delta x_{\mathrm{B\to T}}(F)}{k_B T}\right)\right) = k^0_{B\longrightarrow A}\exp\left(\frac{F\Delta x_{B\to T}}{k_B T}\right) \quad (24)$$

In this approach, the pre-factors ($k^0$) are the transition rates of the unloaded molecules in equation (21). With external load, the transition rates increase exponentially with the applied force.

***Application of stochastic models in force spectroscopy.*** In single molecule force distance experiments intramolecular unfolding or rupture processes are enforced by a mechanical load. The applied load changes the barrier height ($\Delta G^0_{A\to T}$) of the transition and the balance between the bound and unbound states. With increasing pulling force the activation barrier is decreasing until the barrier is low enough to be crossed by thermal fluctuations. Thus, the kinetics and mean forces of association and dissociation depend on the loading rate ($\mathrm{d}F/\mathrm{d}t$).

Typically, unfolding and refolding of proteins show a hysteresis, confirming that the unfolding process occurs far from equilibrium.[137] Thus, the statements from the previous section can only be used as approximations. Bell's formula, later improved by Evans,[138] predicts an increase of the mean rupture (or unfolding) force proportionally to the logarithm of the loading rate ($\kappa_s \cdot \nu$).

A more reliable approach to extract kinetic information from pulling experiments was made by Hummer and Szabo by applying the Kramers' theory of diffusive barrier crossing to a simple free-energy surface. They obtained analytical expressions

[136] Bell (1978)
[137] If trace and retrace force curves match exactly, equilibrium is observed.
[138] Evans and Ritchie (1997)

for the rupture-force probability distribution by introducing a microscopic model that includes thermal fluctuations of the cantilever, which affect the transition process at intermediate pulling speeds. For loading rates, which are typical for most AFM experiments they found a non-linear relation to the average rupture force $\langle F \rangle$ at: $\langle F \rangle \sim (\ln \kappa_s \cdot \nu)^{1/2}$, assuming cusp − like potentials. [139]

However, for high forces/loading rates, thermal fluctuations can be neglected. Dudko *et al.* assumed a different shape of the potential in this force regime than Hummer *et al.* and found $\langle F \rangle \sim (\ln \kappa_s \cdot \nu)^{2/3}$, by applying Kramers' theory as well.[140]

For a better comparison between the different concepts to describe transitions under external load, all three approaches can be written in a general, unified form:[141]

(25)
$$k_{A\to B}(F) = k^0 \left(1 - \left({}^{\nu F \Delta x_{\mathrm{A\to T}}}\!/_{\Delta G_{A\to T}}\right)\right)^{1/(\nu-1)} \exp\left(\Delta G^0_{A\to T}/k_B T - \left[1 - \left({}^{(1-\nu F x_{\mathrm{T}})}\!/_{\Delta G_{A\to T}}\right)\right]\right)$$

The shape of the potential is determined by $\nu = 2/3$ and $1/2$ for linear-cubic and cusp free-energy surfaces and thereby influences the relation between the transition rate and pulling velocities. For $\nu = 1$, and $\Delta G^0_{A\to T} \to \infty$ independent of $\nu$, the expression reduces to Bell's (phenomenological) approach.

In this work, intermediate loading rates were used, thus, Hummer's and Szabo's approach is the relevant concept for the description of the loading rate dependent force distance experiments. Hence, their conception is explained in more detail on the following pages.

[139] Hummer and Szabo (2001); Hummer and Szabo (2003)
[140] Dudko *et al.* (2003)
[141] Dudko *et al.* (2006)

***Microscopic model for intermediate loading rates.*** [142] In this concept, a harmonic potential barrier with the effective force constant $\tilde{\kappa} = \tilde{\kappa}_s + \tilde{\kappa}_m$ is assumed ($\tilde{\kappa}_s$: combined force constant consisting of the cantilever spring constant and the properties of the molecular linker; $\tilde{\kappa}_m$: molecular spring constant of the bonds). The spring constants in this section are scaled by $k_B T$, $\left(\tilde{\kappa} = {}^{\kappa}/_{k_B T}\ ;\ \kappa\left[{}^{\mathrm{N}}/_{\mathrm{m}}\right]\right)$. In a first approximation, it is supposed that once the barrier is crossed by thermal fluctuations no backward transition is possible. To extract the rate constant from force distance experiments, Kramers' theory of diffusive barrier crossing in the absence of external force is applied. With this theory, following relation between the free energy barrier ($\Delta G_{A\to T}$) and the intrinsic rate constant ($k_0$) can be obtained by considering Brownian motion with a diffusion coefficient $D$ and a harmonic potential wall:

$$(26)\quad k_0[x_T;\ \tilde{\kappa}_m] \approx (2\pi)^{\left(-\frac{1}{2}\right)} D\tilde{\kappa}_m^{(3/2)} \Delta x_{A\to T} \exp\left(-\beta \Delta G^0_{A\to T}\right), \beta \Delta G^0_{A\to T} = \frac{\tilde{\kappa}_m (\Delta x_{A\to T})^2}{2}$$

with: $\beta = (k_B T)^{-1}$

If the pulling velocity $v$ is sufficiently slow that the activation energy is still large, when the system ruptures, following general expression for the survival probability $S$ in the presence of a time-dependent barrier at $(x_{A\to T} - \overline{x}(t))$ can be made:

$$(27)\quad S(t) = \exp\left\{-\int_0^t k_0[x_T - \bar{x}(t');\ \tilde{\kappa}]dt' \right\},\ \bar{x}(t) = \frac{v\tilde{\kappa}_S}{D\tilde{\kappa}^2}\left(D\tilde{\kappa}t + e^{-D\tilde{\kappa}t} - 1\right)$$

Here, the intrinsic rate constant ($k_0$) for a transition barrier is dependent on the time-dependent, fluctuating position $x$ and the effective spring constant $\tilde{\kappa}$. Applying Kramers' theory leads to:

$$(28)\qquad S(t) = \exp\left\{-\frac{k_0 \exp\left[-\tilde{\kappa}_s (x_T)^2/2\right]}{\tilde{\kappa}_s v x_T (\tilde{\kappa}_m/\tilde{\kappa})^{3/2}}\left[\exp(\tilde{\kappa}_s v \Delta x_{A\to T} t - (\tilde{\kappa}_s v t)^2/2\tilde{\kappa}) - 1\right]\right\}$$

The probability distribution $p(F)$ of rupture forces $F\beta = -\tilde{\kappa}_S(x_T - vt^*)$ can be readily obtained from $\left[p(F)\mathrm{d}F = -\dot{S}(t^*)\mathrm{d}t^*\right]$.

Equation (28) and the lifetime ($t^*$) dependent expression for the rupture force lead to:

[142] Hummer and Szabo (2003)

$$p(F) = (\tilde{\kappa}_s v)^{-1}\left[-\dot{S}(t^*)\right]_{t^*=(\beta F+\tilde{\kappa}_s x_T)/\tilde{\kappa}_s v} \tag{29}$$

Relevant parameters such as $k_0$, $x_T$, and $\Delta G_{A\to B}$ can be obtained from the analysis of rupture force histograms, using relations (26) and (29).

Another rather robust way to analyze the experimental data is the expression for average rupture forces $\langle F\rangle$ dependent on the pulling velocity.

$$\langle F\rangle\beta = \tilde{\kappa}_m x_T - \left[2\tilde{\kappa}\ln\frac{k_0 e^{\gamma+\tilde{\kappa}_m (x_T)^2/2}}{\tilde{\kappa}_s v x_T (\tilde{\kappa}_m/\tilde{\kappa})^{3/2}}\right]^{1/2} \tag{30}$$

where $\gamma = 0.5772$ is the Euler-Mascheroni constant.

Thus, by equation (30) the kinetic information can be extracted by plotting the experimental data (the mean rupture forces) versus the loading rate ($\kappa_s v$).

Figure 36 shows the average rupture force as a function of pulling velocity obtained from simulation.

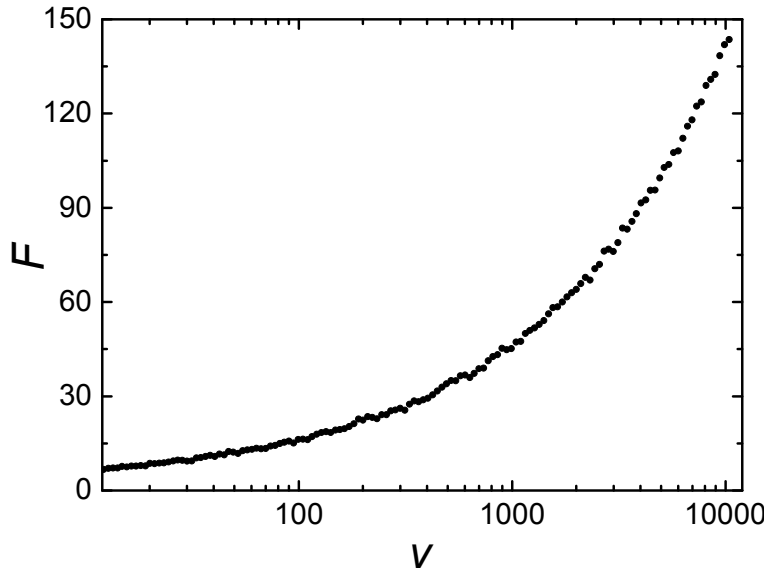


**Figure 36:** Rupture force as a function of pulling velocity obtained from simulation, based on the microscopic model of Hummer and Szabo. Parameters settings: $\tilde{\kappa}_s = 1$; $\tilde{\kappa}_m = 10$; $D = 1$; $\beta = 1$, and $x_T = 1$.

As shown here, the logarithmic dependency of the rupture force on the loading rate as predicted by the Evans model, based on Bells approach, is only valid in a very limited range ($v < 100$) and hardly reliable. Therefore, Hummer's and Szabo's concept is used to obtain kinetic and thermodynamic information from the experimental data. However, in this concept no rebinding is taken into account, what is at certain loading rates a discrepancy to the comprehension of the performed experiments. Hence, this model has to be extended.

***Model for concurrent bond rupture and formation.*** Li and Leckband used a probability theory, including an ensemble of bonds, to describe unbinding by external load and rebinding based on Brownian fluctuations.[143] They presumed a simple two-step reaction mechanism defined by the bound state *A*, the transition state *T*, and the free state *B* (as already shown in figure 35, p. 72): $A \rightleftharpoons T \rightleftharpoons B$.

In the regime of the bound state ($x \leq x_T$), following expression for the combined molecular, intrinsic energy and spring potential is expressed as:

$$G(x, z_P) = \frac{1}{2}\kappa_m x^2 + \frac{1}{2}\kappa_S (z_P - x)^2 \quad ; x \leq x_T \tag{31}$$

with: separation distance $z_P = v \cdot t$

After transition ($x > x_T$), the potential is determined by the more flexible unbound molecule, expressed by the molecular spring constant $k_{m2} = \frac{k_m {x_T}^2 - 2\Delta G_{A\to B}}{(x_T - x_B)^2}$.

$$G(x, z_P) = \frac{1}{2}k_{m2}(x_B - x)^2 + \frac{1}{2}k_S (z_P - x)^2 + \Delta G_{A\to B} \quad ; x_T < x < x_B \tag{32}$$

In order to obtain the rate constants for breaking and rebinding, an expression for the mean first passage time (MFPT) of the transition and the partition functions of state *A* and *B* have to be calculated as follows:

$$Z_A = \int_{-\infty}^{x_T} exp\left[\frac{\frac{1}{2}k_m x^2 + \frac{1}{2}k_S (z_P - x)^2}{k_B T}\right] \mathrm{d}x \,; \; x < x_T \tag{33}$$

$$Z_B = \int_{x_T}^{\infty} exp\left[\frac{-\left(\frac{1}{2}k_{m2}(x_B - x)^2 + \frac{1}{2}k_S (z_P - x)^2 + \Delta G_{A\to B}\right)}{k_B T}\right] \mathrm{d}x \,; \; x_T < x < x_B \tag{34}$$

For the MFPT, the following simplified expressions can be derived from Kramers' theory, when assuming a high cusped-shaped barrier ($G \gg k_B T$):

$$\tau_A(z_P) = \frac{\widetilde{\gamma}}{k_m + k_S}\sqrt{\pi}\sqrt{\frac{k_B T}{\Delta G_{A\to T}(z_P)}}\exp\left[\frac{\Delta G_{A\to T}(z_P)}{k_B T}\right] \tag{35}$$

[143] Li and Leckband (2006)

(36) $$\tau_B(z_P) = \frac{\tilde{\gamma}}{k_{m2}+k_S}\sqrt{\pi}\sqrt{\frac{k_BT}{\Delta G_{B\to T}(z_P)}}\exp\left[\frac{\Delta G_{B\to T}(z_P)}{k_BT}\right]$$

with: drag coefficient $\tilde{\gamma}$.

Consequently, rate constants for breaking ($k_{\mathrm{off}}$) and rebinding ($k_{\mathrm{on}}$) are given as:

(37) $$k_{off}(z_P) = \left(\tau_A(z_P) + \tau_B(z_P)\frac{Z_{A(z_P)}}{Z_{B(z_P)}}\right)^{-1}$$

(38) $$k_{on}(z_P) = \left(\tau_B(z_P) + \tau_A(z_P)\frac{Z_{B(z_P)}}{Z_{A(z_P)}}\right)^{-1}$$

To calculate the bond survival probability $S$, following differential equation has to be solved, for each velocity $v$, since $z_P = v{\cdot}t$ and $S = \dot{-}k_{off}{\cdot}\mathrm{S} + k_{on}(1-S)$

(39) $$\frac{\mathrm{d}}{\mathrm{d}(z_P)}\mathrm{S}(z_P) = \frac{-k_{off}(z_P)}{v}{\cdot}\mathrm{S}(z_P) + \frac{k_{on}(z_P)}{v}\left(1-S(z_P)\right)$$

with the boundary condition $S(0) = 1$.

Hence, the probability density function and the corresponding force can be calculated as a function of the compensated separation distance [$F(z_P) = k_{\mathrm{S}}\cdot(z_P - x_{\mathrm{T}})$], leading to force distribution histograms, which are comparable to the experimental results:

(40) $$\left[p(z_P) = -\frac{\mathrm{d}}{\mathrm{d}(z_P)}S(z_P)\right]$$

***Monte Carlo (MC) simulations.*** Another approach to obtain thermodynamic parameters of the transition is the Monte Carlo simulation.[144] This stochastic simulation provides information about the energy profile by adjusting its intrinsic parameters from the two-well potential ($k_{\mathrm{m}}$, $k_{\mathrm{m2}}$, $D$ and $x_{\mathrm{T}}$) for different loading rates in order to achieve simulation results that match with the experimental data.

The simulation algorithm of bond dissociation and association under external load is based on a superposition of intrinsic bond force, external pulling force and Brownian force along the separation (or reaction) coordinate. Kramers' one dimensional

[144] For a basic introduction of Monte Carlo simulations, see:
Faiß (2007); Janke (2004); Lüthgens (2005)

diffusion model is used to define the state of the bond and the relative position along the separation coordinate is given by the overdamped Langevin equation:

$$\tilde{\gamma} \cdot \dot{x} = -\partial_x G(x,t) + \xi(t) \tag{41}$$

with: drag coefficient $\tilde{\gamma}$; bond force $-\partial_x G(x,t)$; Brownian random force $\xi(t)$ with a force average of zero and a deviation of $2 \cdot \tilde{\gamma} k_B T$.

By employing the second order stochastic Runge-Kutta method,[145] the Langevin equation can be described approximately as finite difference equations that are used as Monte Carlo simulation steps.[146]

$$x_2(\Delta t) = x_1 + \frac{D}{2k_B T}\left(-\frac{\partial}{\partial_x}G(x_1) - \frac{\partial}{\partial_x}G\left(x_1 + \frac{D}{kT}\left(-\frac{\partial}{\partial_x}G(x_1)\right)\Delta t + \xi(t)\right)\Delta t\right) + \xi(t) \tag{42}$$

with: simulation time step $\Delta t = t_1 - t_2$ (in the range of nanoseconds); diffusion coefficient $D = k_B T/\tilde{\gamma}$.

The input parameters ($k_m$, $k_{m2}$, $D$, and $x_T$) of a two-well potential are estimated as empirical values from evaluation of Molecular Dynamics simulations and miscellaneous experimental analysis. By optimizing these simulation parameters, the obtained force distributions can be brought in accordance with the experimental force distance data. To further validate the accuracy of the theoretical model, the obtained parameters can be used as input for the numerical calculations as presented before. Results of these calculations should match the experimental data as well.

Importantly, in this simulation, different bonds cannot interact with each other, thus, only a zipper-like mechanism of multiple bond transitions is considered. Qualitative conclusions about the comprehensive rupture mechanism of several bonds have to be made by MD simulations.

[145] Branka and Heyes (1998); The Runge-Kutta algorithm is a true second order method that is more robust than the conventional Ermak algorithm allowing larger time steps.

[146] Programming of the Monte Carlo algorithm was performed by Prof. Dr. A. Janshoff.

*Basics about Molecular Dynamics (MD) simulations.* Apprehending the experimental information in detail requires precise knowledge of the mechanism of the involved interactions like hydrogen bonds, van der Waals forces and covalent bonds. MD simulations facilitate the understanding of the interplay of these complex processes in an overall concept. This is of great importance to establish mathematical models that enable the prediction of sophisticated folding processes of proteins or elaborated intramolecular transitions of macromolecules.

The force field simulations of stretching and relaxation of a single bis-loop tetraurea calix[4]arene-catenanes were performed by Dr. Thorsten Metzroth with use of GROMACS 3.2 program package.[147]

Here, only a brief, general description of MD simulation is given; the explanation of the performed simulations is described in chapter 5.4.

The exact depiction of complex systems by solving numerically the Schrödinger equation is not possible so far due to the enormous computing expenditure. Thus, approximations like the Born-Oppenheimer approximation have to be made. There, only the slow movement of the nuclei and not the rapid mobility of electrons are taken into account. Furthermore, the molecule is considered as a system consisting of point masses, which are connected via ideal springs and move inside a classical force field, consisting of Coulomb and van der Waals forces. The movement of all atoms is calculated by numerical integration of Newton´s equations of motion, at a constant temperature with a defined cut-off radius for the long-range interactions. Due to the rapid fluctuations of the atoms, the small time steps of the simulation ($10^{-15}$ – $10^{-16}$ s) lead to immense computational efforts. Hence, usually the total simulation time for complex systems lies in the nanosecond range, depending on the computer resources and the amount of involved atoms. With respect to “real” force distance experiments, carried out by AFM, the loading rate in the MD simulations is several orders of magnitude higher. Thus, rupture forces cannot be compared due to force-driven shifts in the energy landscape; however, qualitative conclusions about the comprehensive rupture mechanism, like a zipper-like or concerted fracture behavior of the involved interactions, can be made by MD simulations.

[147] Group of Prof. Dr. J. Gauß, Institute of Physical Chemistry, Johannes-Gutenberg University of Mainz.

## 5.4 Experimental results & discussion: Single-molecule force spectroscopy on bis-loop tetra-urea calix[4]arene-catenanes

In this chapter, experiments are presented, in which single, long-chain molecules are stretched with different loading rates to scrutinize the concerted unfolding and refolding mechanism of intramolecular hydrogen bonds in entangled bis-loop tetra-urea calix[4]arene-catenanes.

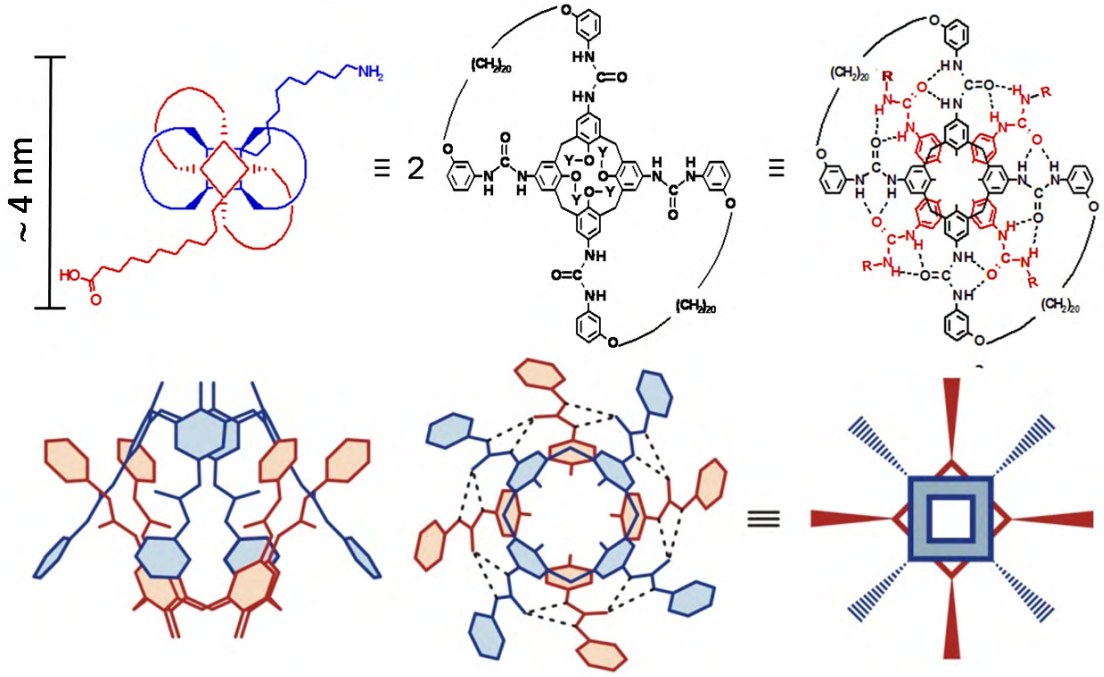


**Figure 37:** Schematic drawings of a single nanocapsule consisting of two intramolecular entangled bis-loop tetra-urea calix[4]arenes. The capsule is kept in a tight conformation by 16 hydrogen bridges that are formed between the monomers.

As depicted in figure 37, one "nanocapsule" consists of two calixarene monomers, which are connected via 16 hydrogen bonds. The hydrogen bridges are formed by four urea groups at the upper ring of each calixarene monomer; between two monomers eight hydrogen bonds can be considered as strong (N…O distance 0.286 nm) and eight as weak (N…O distance 0.329 nm).[148] Together with the spacers, each bimolecular capsule exhibits a length of about 4 nm in the initial state and approximately 6 nm in the elongated state after the rupture of intramolecular hydrogen bonds, as demonstrated by MD simulations later in this chapter.

[148] Vysotsky *et al.* (2003)

The nanocapsules are oligomerized via covalent coupling between the amino and carboxyl groups, which are located at the terminus of each spacer, resulting in long-chain molecules with 4 – 6 connected capsules on average.

In contrast to adhesion experiments, which exhibit a maximal force in the nano Newton regime (chapter 4.3), the force level of investigation in single-molecule experiments ranges usually between 10 and 150 pN.[149] An illustrative explanation of the conducted force distance experiments is given in the following figure and is described more precisely in section 2.3.

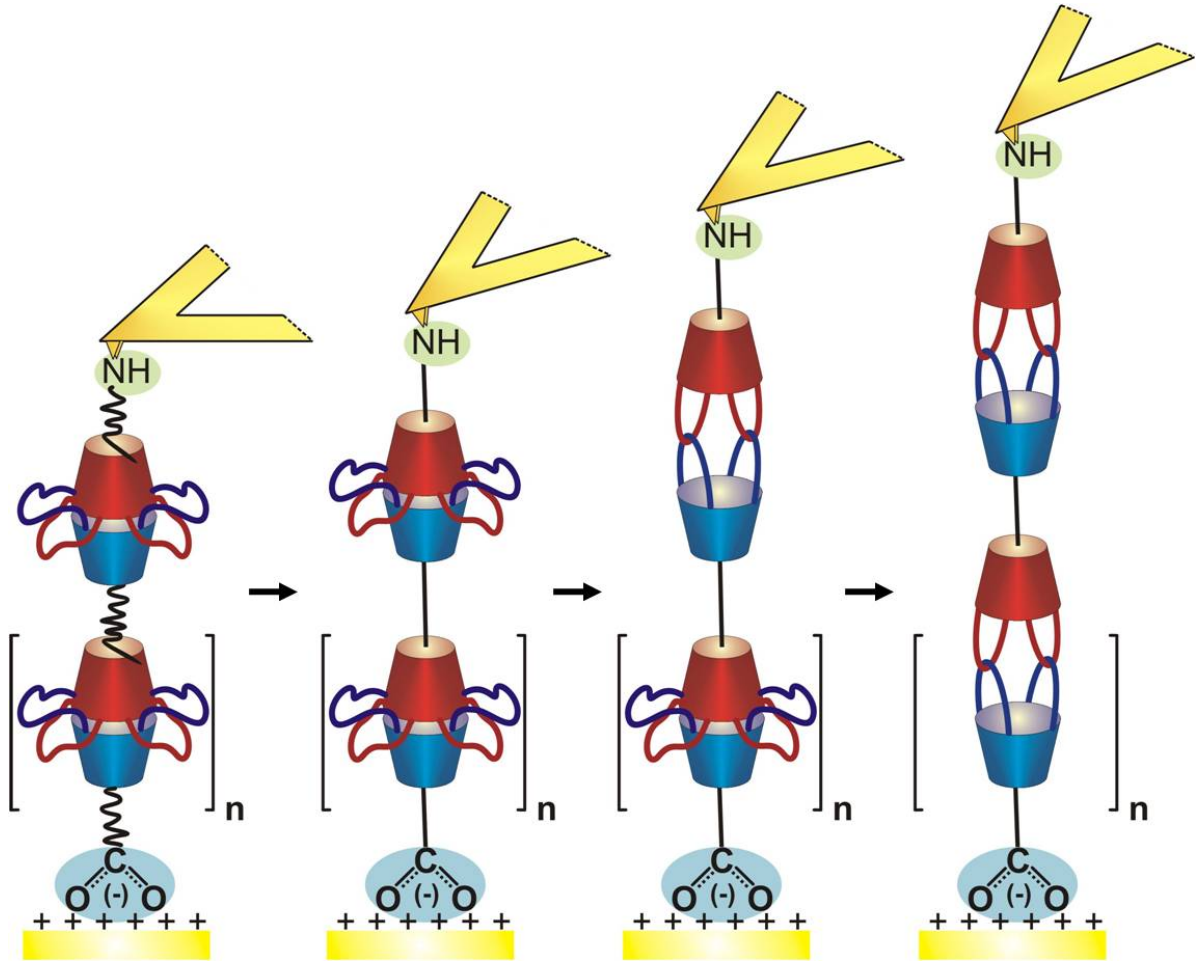


**Figure 38:** Schematic drawing of the single-molecule stretching experiment. The molecule is attached to the ($AUT^+$) functionalized, positively charged gold substrate via the dissociated negatively charged terminal carboxyl group. By gently touching the surface with the functionalized tip, a molecule is picked up via covalent coupling between the terminal amino group and the succinimidyl ester groups of the functionalized cantilevers. With increasing force, the molecule is continuously stretched in a WLC-like manner until intramolecular rupture of the hydrogen bridges occurs, leading to a sudden extension of about 1 – 2 nm per capsule. By careful execution of the experiment, the elongated molecule remains in contact to the tip and substrate and can be retracted to investigate the rejoining processes of the capsules.

[149] Weisel *et al.* (2003)

***General features of force distance curves with calixarene-catenanes.*** Stretching experiments with oligomerized calixarene-catenanes exhibit a characteristic sawtooth pattern in which the individual events are separated by 1 – 2 nm. Figure 39 shows two typical stretching curves at different loading rates and the corresponding elastic WLC fits to the data with a persistence length of about 0.4 nm. The difference in the contour length $\Delta L$ expresses the exact length extension between two events, which can be attributed to the elongation of a single capsule.

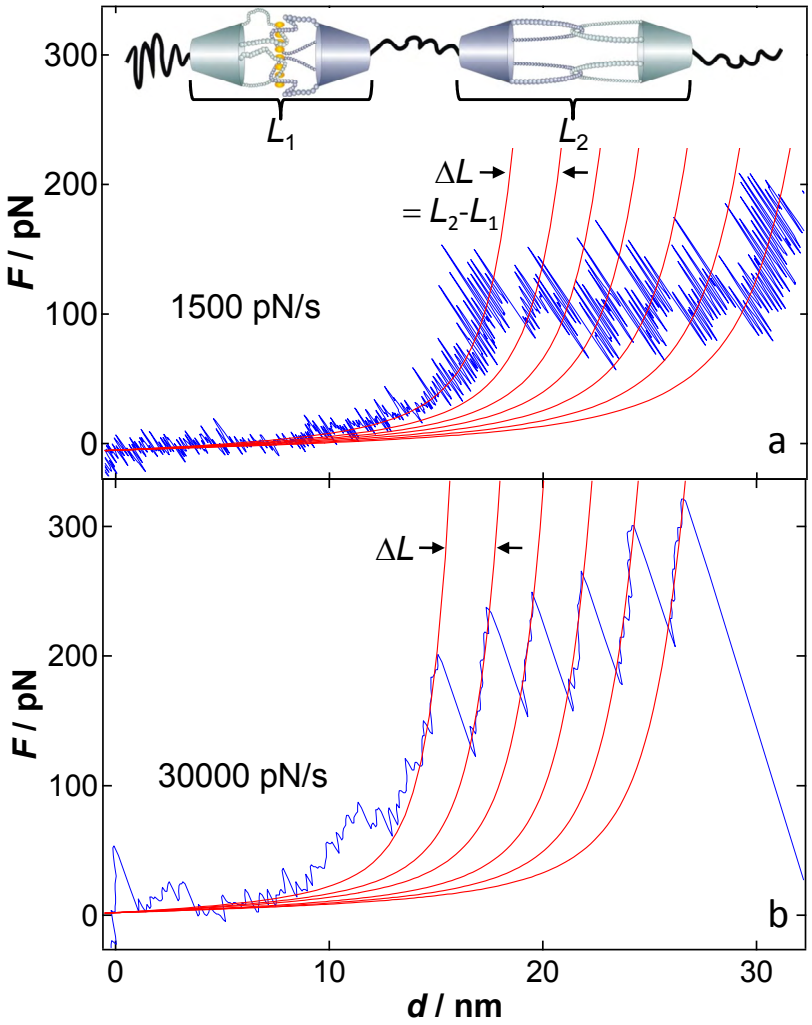


**Figure 39:** Stretching and subsequent rupturing of an individual oligo calixarene-catenane at **a)** 1500 pN/s and **b)** 30000 pN/s. The red lines are wormlike chain (WLC) fits to the data with a persistence length $l_p$ of ~ 0.4 nm.[150] The changes in the contour length $\Delta L$, as obtained from the fitting procedure, are of about 2 nm. These abrupt extensions are associated with the elongation of single capsules after breakage of the intramolecular hydrogen bonds, as illustrated in the upper part of a). The yellow parts inside the tight capsule resemble intact hydrogen bridges.
Due to the higher data sampling at lower pulling velocities, the noise level at 1500 pN/s (velocity: 50 nm/s, low-pass filter setting: 1 kHz) is higher than at 30000 pN/s (velocity: 1000 nm/s, low-pass filter setting: 3 kHz).

[150] The elastic WLC fits include following parameters:
**a)** 1500 pN/s: $l_p$: 0.37 nm; $\Phi$: 14 nN; $L$: 20.5, 23, 25, 27, 29.5, 32.2, 34.8 nm; $T$: 293 K
**b)** 30000 pN/s: $l_p$: 0.37-0.4 nm; $\Phi$: 14 nN; $L$: 16.8, 19.3, 21.5, 23.8, 26, 28.4 nm; $T$: 293 K

The sawtooth pattern of the extension curves is consistent with the idea of an independent breaking of individual capsules. During a pulling experiment the tension inside a long-chain molecule is the same throughout its length. An abrupt extension of the chain, e.g. caused by a sudden opening of one of its nanocapsules, leads to a rapid drop in the tension that is detected by the cantilever.

The stochastic nature of discrete extension events of a clamped molecule reveals individual elongations of single capsules since the probability of capsule opening depends on the number $n$ of available tight capsules and decreases after elongation of each capsule. Thus, the next rupture event occurs evidently after the tension has increased again.

In a force distance curve, the number of capsules is directly linked to the sawtooth pattern, e.g. in figure 39 a) six capsules and in (b) five capsules are stretched. This is in good agreement with the estimated number of capsules calculated from the longest contour length, $L \sim 35$ nm in (a) and 28.5 nm in (b), divided by the theoretical length of an elongated capsule of about 6 nm.

Interestingly, as shown in the difference between 1500 pN/s (a) and 30000 pN/s (b), the observed forces of the rupturing events rise with increasing loading rate. This phenomenon is discussed in greater detail below.

***Reversibility and fishing experiments.*** Due to the mechanical lock, provided by two entangled loops, the opening of the nanocapsules is in principle a reversible process. Thus, reformation of hydrogen bridges in conjunction with rejoining of the capsules into a tighter conformation is possible and can be observed in the retracting curves. An example of clearly visible rejoining events is shown figure 40.

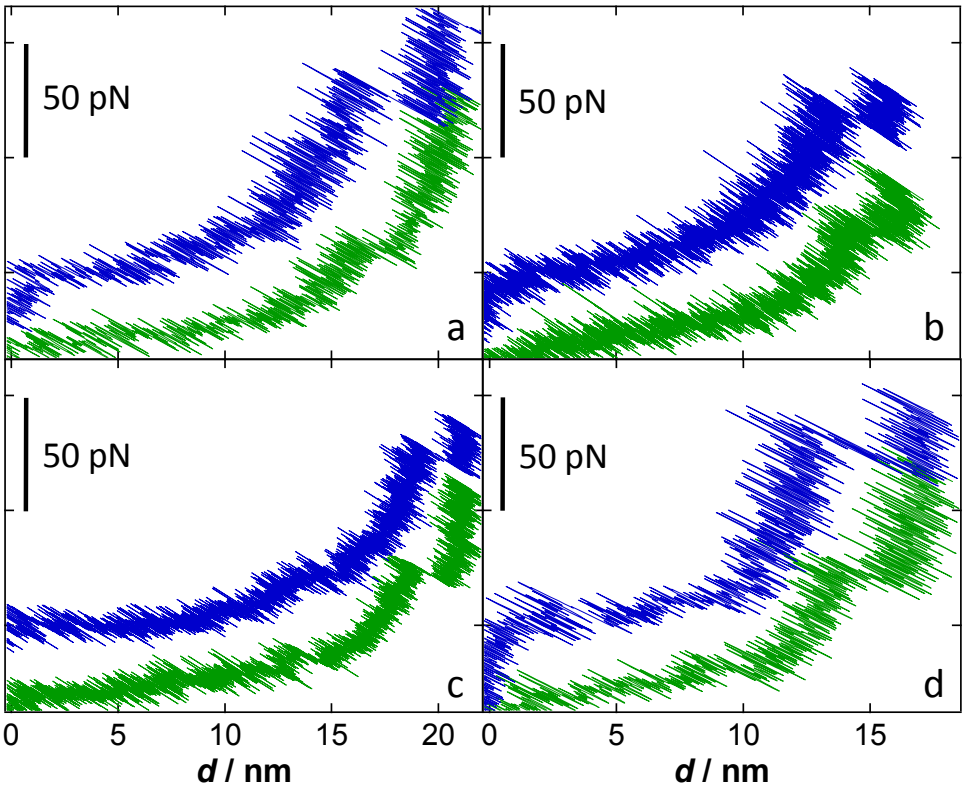


**Figure 40:** A composition of force distance curves that exhibit distinct events in the retracting curve (green). These events are assigned to recombination events of the capsules. In **a) – c)** the measurements were conducted at 60 pN/s and in **d)** at 300 pN/s. For a better visualization, an offset of 30 pN was set between trace (blue) and retrace (green).

A substantial hysteresis between pulling and relaxation is observable and is increasing at higher loading rates. Hence, unmistakably detectable rejoining events are only found at lower pulling velocities. However, the rebinding events are usually less pronounced and display a less obvious sawtooth appearance.

When stretching a molecule, it frequently separates from either the tip or the substrate, which prevents an investigation of rejoining events of the capsules. Only by carefully performing the experiment, the elongated molecule remains in contact with tip and substrate and can be retracted to scrutinize the rejoining processes of the capsules. Continuous stretching and relaxing cycles of a clamped single-molecule are referred to as fishing experiments.

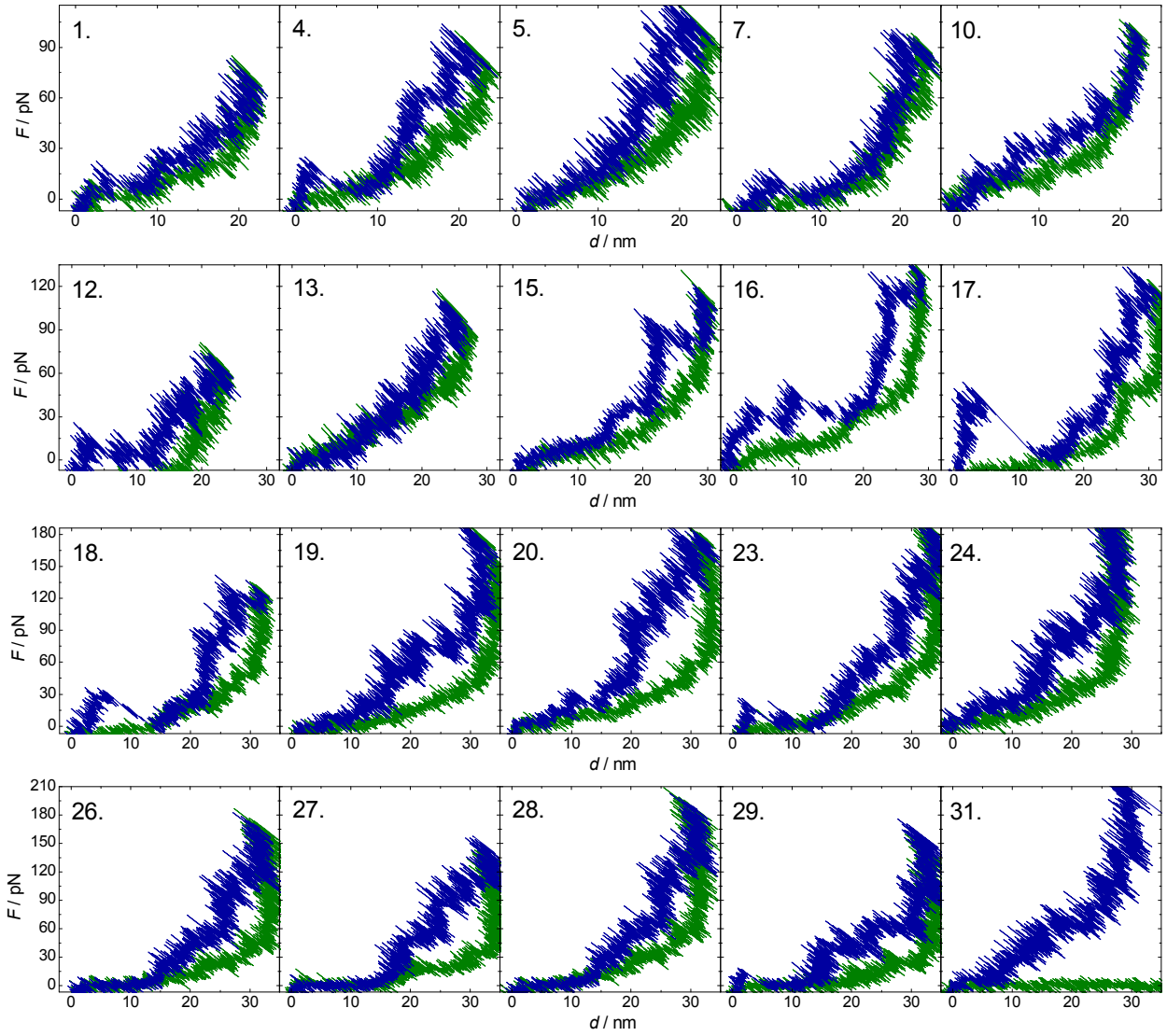


**Figure 41:** A sequence of stretch (blue traces) and relax (green traces) measurements of an oligomerized calixarene catenane at a loading rate of 300 pN/s. The distance was slowly increased between each cycle, leading to higher forces. In cycle 31 the molecule broke off (not all 31 cycles are shown).

Figure 41 displays a successful example of a fishing experiment, in which the maximal stretching distance is increased gradually between the individual force curves until the molecule breaks off in cycle 31. Stretching events within a distance of about 10 nm from the surface were considered as non-specific adhesion phenomena and were neglected in the further evaluation of the data.

In contrast to the unfolding of most linked protein domains such as titin, ankyrin, spectrin or fibronectin, [151] the rupture events show no reduction of unfolding capsules in the subsequent stretching cycle which acknowledges the perception of a fully reversible process on the experimental timescale due to the entangled structure.

[151] Lee *et al.* (2006); Oberdörfer *et al.* (2000); Rief *et al.* (1997); Rief *et al.* (1999)

Even while pulling on the molecule, rejoining of already ruptured capsules to intact tight capsules can take place similarly to what has been described by Schlierf and Rief for protein folding from and unfolding into an intermediate state.[152] Hence, before retraction of the strained capsules, rejoining of the dimers occurs which is identifiable by a pronounced force plateau in the extension curves (figure 41, e. g. cycle 4 and 26 – 28). Such a plateau exhibits a less obvious sawtooth appearance as also found by Bustamante and co-workers for ribozyme unfolding.[153] However, a substantial hysteresis between extension and relaxation of the oligomer indicates that the system is still not in equilibrium at a loading rate of 300 pN/s.

Precise information about the energy landscape of the 16 hydrogen bonds in a dimer requires velocity dependent measurements in conjunction with MD simulations and stochastic calculations as shown below (pp. 88ff. and pp. 94ff.).

[152] Schlierf and Rief (2005)
[153] Onoa *et al.* (2003)

***Analysis of the force distance curves.*** A comprehensive quantitative analysis of rupture and rejoining events of experiments with calixarene-catenanes was carried out by identifying the force and extension of each rupture event, as well as the rejoining forces. Due to the less pronounced rebinding events, a quantitative determination of the contraction length of individual capsules was difficult and, therefore, not evaluated.

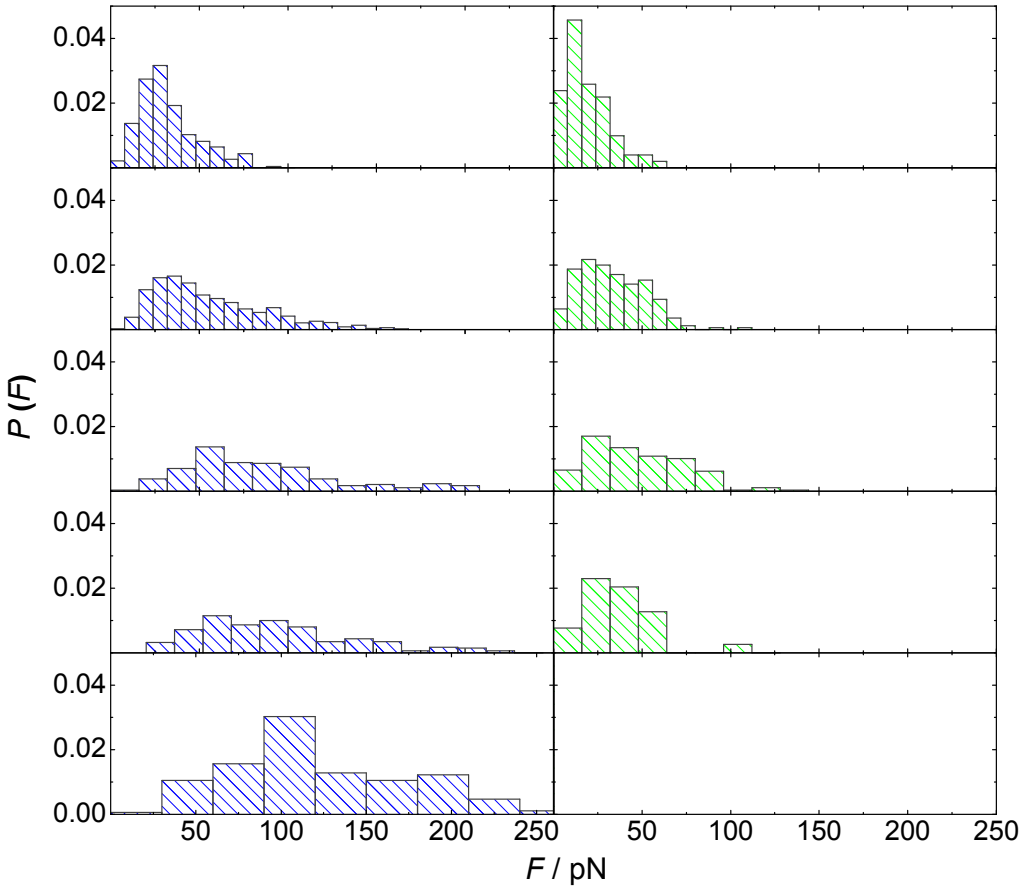


**Figure 42:** Rupture force (blue, left) and rejoining force (green, right) histograms collected at different loading rates. **a)** breaking: n = 295, rejoining: n = 69 (n denotes the number of events found in the cycle), **b)** breaking: n = 1110, rejoining: n = 219, **c)** breaking: n = 710, rejoining: n = 182, **d)** breaking: n = 223, rejoining: n = 26, **e)** breaking: n = 172, no rejoining events found. For a better comparison, events with extensions longer than 1 nm were counted as multiples of 1 nm.

As shown in figure 42, the average rupture forces $<F_{rup}>$ at higher rates increase and the normalized rupture force histograms broaden significantly. The distributions of rejoining forces as a function of loading rate exhibit a decreasing mean value $<F_{rejoin}>$ with an increase in width as the loading rate rises. At loading rates larger than 6000 pN/s rejoining is no longer observed confirming that the pulling process became entirely irreversible.

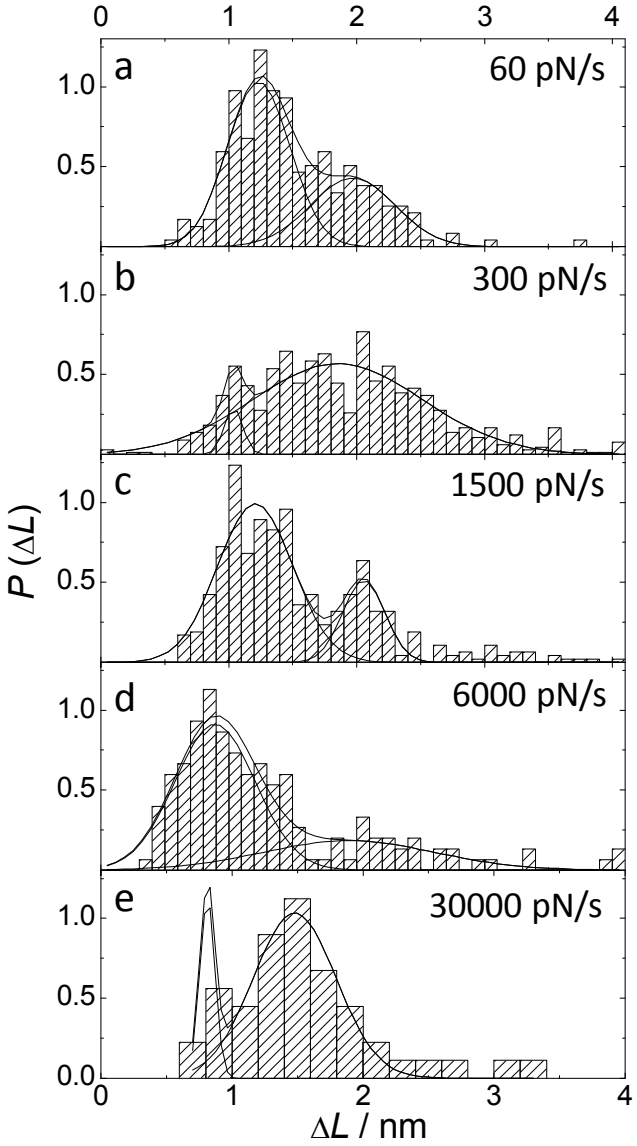


**Figure 43:** Histograms of the extensions per rupture event obtained from stretching curves at different loading rates. Fitting two Gaussian functions to the corresponding histograms provide following mean separations and widths: **a)** 60 pN/s; n = 236, $\Delta L_1$ = (1.2 ± 0.49) nm, $\Delta L_2$ = (1.97 ± 0.66) nm **b)** 300 pN/s; n = 662, $\Delta L_1$ = (1.03 ± 0.14) nm, $\Delta L_2$ = (1.85 ± 1.32) nm **c)** 1500 pN/s; n = 482, $\Delta L_1$ = (1.2 ± 0.58) nm, $\Delta L_2$ = (2.05 ± 0.33) nm **d)** 6000pN/s; n = 157, $\Delta L_1$ = (0.9 ± 0.63) nm, $\Delta L_2$ = (1.9 ± 1.33) nm **e)** 30000 pN/s; n = 46, $\Delta L_1$ = (0.81 ± 0.13) nm, $\Delta L_2$ = (1.47 ± 0.63) nm.

Figure 43 shows the length distribution of rupture events as a function of the loading rate. A bimodal distribution is apparent, especially at lower loading rates, where a lot of data could be acquired due to better measurement conditions. The maxima of the histograms are located at around 1 and 2 nm. These characteristics of the distribution indicate the presence of a stable intermediate state in the rupturing mechanism of the intramolecular hydrogen bridges. The appearance of an intermediate state in the rupturing mechanism is also observed in molecular dynamics

simulations and is examined by numerical calculations and Monte Carlo simulations in the discussion section of this chapter.

Due to different lengths of rupture events, the detected rupture forces are weighted by steps of 1 nm. Hence, an event with an extension of 2 nm is counted twice to generate the histograms in figure 42. By the use of this method, a possible misinterpretation of rupture events, which are difficult to evaluate, does not affect the analysis. However, without a weighting of the rupture events, no substantial change in the shape of distribution and average rupture forces is observable.

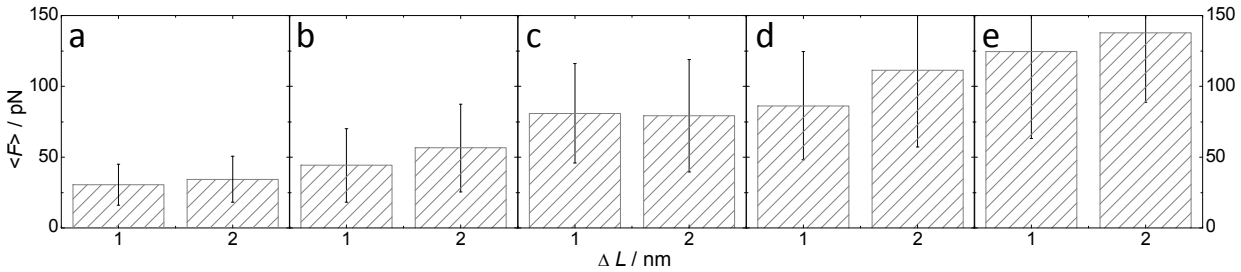


**Figure 44:** Average rupture forces of events with a discrete length extension of 1 (± 0.4) or 2 (± 0.4) nm and a contour length of < 23 nm.
**a)** 60 pN/s; 1 nm: 30.5 pN; 2 nm: 34.4 pN, **b)** 300 pN/s; 1 nm: 44.2 pN; 2 nm: 46.5 pN **c)** 1500 pN/s; 1 nm: 80.9 pN; 2 nm: 79.3 pN, **d)** 6000pN/s; 1 nm: 86.2 pN; 2 nm: 111.3 pN, **e)** 30000 pN/s; 1 nm: 124.4 pN; 2 nm: 137.8 pN.

To determine a correlation between length extension and rupture force, all events are classified into two length categories of either 1 (± 0.4) or 2 (± 0.4) nm. As shown in figure 44, events with a capsule elongation of 2 nm exhibit slightly higher average rupture forces. Thus, a correlation between the plateau length and rupture force seems to be apparent, but has to be affirmed substantially by simulations and theory.

***Impact of the solvent on force distance experiments.*** The force distance experiments were conducted in mesitylene (1,3,5-trimethylbenzene) solution. Mesitylene displays a high solubility of calixarenes and a high boiling point, which is required for stable single molecule experiments.

The dimeric calixarene capsules exhibit a cavity with a size suitable for the inclusion of solvent molecules. As hydrogen bridges inside the capsules can be influenced by the dielectric permittivity of the guest molecules, it is important to test if impurities of the solvent may affect the experimental result. Toluene can be considered as the most likely contamination of mesitylene. In addition, toluene is the preferred cavitant, since the molecule is smaller. Thus, control experiments were conducted with 5 vol% toluene as additive. Figure 45 shows rupture force distributions of performed experiments in pure mesitylene (a) and with 5 vol% toluene as additive (b). The shape of the histograms and average rupture forces (pure mesitylene: $84.1 \pm 43.2$ pN; toluene additive: $85.4 \pm 49.7$ pN) show no disparities. This was expected, because mesitylene and toluene exhibit the same dielectric constant (both: $\varepsilon_r = 2.4$ at room temperature).

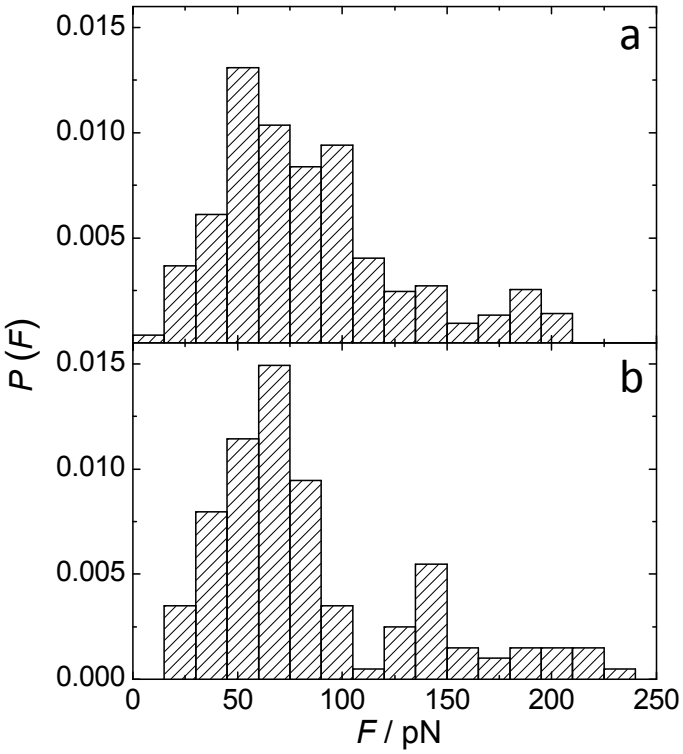


**Figure 45:** Rupture force histograms (loading rate 1500 pN/s). **a)** obtained in pure mesitylene, **b)** mesitylene with toluene (5 vol%) as additive.

***Effect of the linker / contour length on the observed phenomena.*** The elastic response of a molecular system is directly coupled to the mechanical properties and length of the spacer between cantilever and the bond or molecular transition under investigation. Evans and Ritchie studied in a theoretical approach the effect of a soft molecular linkage on the strength of a weak connecting bond.[154] Based on theoretical considerations, Friedsam *et al.* used Monte Carlo simulations to illustrate the effect of a soft spacer on rupture force histograms.[155] By assuming polymer spacers with a length distribution, the rupture force histograms were broadened significantly.

Thormann *et al.* evaluated the effect of either a bovine serum albumin (BSA) linker or poly(ethylene)glycol (PEG) spacer on the well-known biotin-streptavidin bond.[156] In the case of the BSA linker, they found a linear increase of the pulling force with the time, indicating a soft response of the BSA that leads to a broadening in the distribution of the rupture forces. By using the soft polymer PEG as linker, they found a reduction in average unbinding forces in comparison to calculations without a soft spacer. Due to the soft linker, the force ramp inclines towards lower forces, compared to a linear force ramp. Hence, the molecular system spends more time at low forces, leading to a higher probability of bond rupture at low forces.

In general, two categories of linkers can be found. In case of a system with linear compliance, two linear springs are connected in series. This results in a combined force constant $\kappa_s$, consisting of the cantilever spring constant $\tilde{\kappa}_c$ and the properties of the molecular linker $\kappa_{linker}$.

$$\kappa_S = \left(\frac{1}{\kappa_C} + \frac{1}{\kappa_{linker}}\right)^{-1} \tag{31}$$

If the molecules are rather stiff ($\kappa_{linker} \gg \kappa_C$), the obtained results in rupture forces can be considered approximately as independent of the molecule length and elastic properties, hence, the spring constant of the cantilever dominates the force ramp of the experiment.

In case of a system with nonlinear compliance, polymer models, e.g. the WLC model, have to be used to describe the elasticity properties of the molecular chain.

[154] Evans and Ritchie (1999)
[155] Friedsam *et al.* (2003)
[156] Thormann *et al.* (2006)

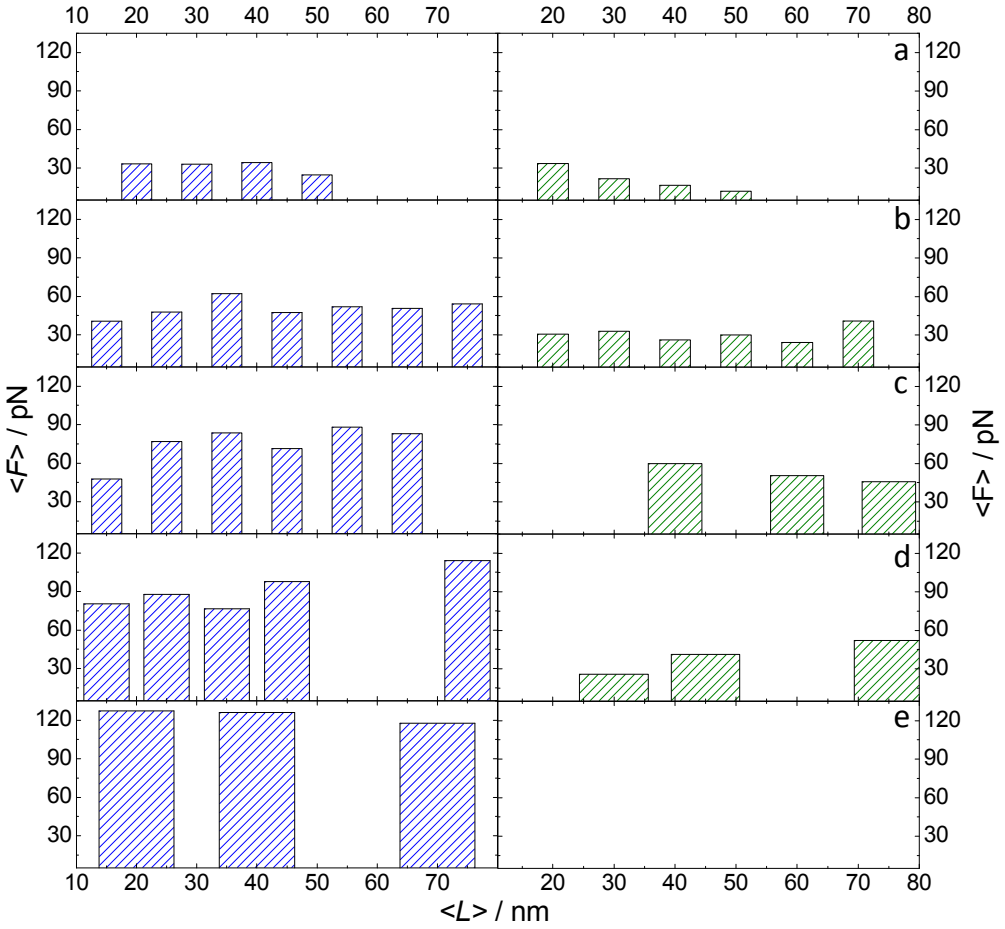


**Figure 46:** Average forces (rupture: blue, rejoining: green) as a function of contour length intervals at different loading rates. In case of low data points, a wider range of the contour length interval was used. **a)** 60 pN/s; **b)** 300 pN/s; **c)** 1500 pN/s; **d)** 6000pN/s; **e)** 30000 pN/s.

In the single molecule force distance experiments the influence of the linker was observed by segmenting the results dependent on the contour lengths. As shown in figure 46, no correlation between contour length and average forces was found experimentally, which may be attributed to the considerably small length of the decylene ($-C_{10}H_{20}-$) spacers that leads in conjunction with the inelastic capsules to rather stiff oligomers. In addition, the linker molecules exhibited a distinct length without any deviations as occurring frequently with long polymer spacers (e.g. PEG).

Nevertheless, in order to minimize broadening of the distribution of experimental data, only molecules in a contour length interval from 10 – 30 nm were selected for detailed analysis and comparison with theoretical calculations and simulations.

*Discussion and comparison with theory.* The profound understanding of breakage and rebinding of hydrogen bridges under external load remains a key issue in simulation, prediction and emulation of complex biological structures and their functions. Here, substantial contribution to increase the fundamental knowledge of hydrogen bonding was achieved by force spectroscopy of a supramolecular structure, with well defined intramolecular hydrogen bonds.

In order to extract relevant parameters from the energy landscape of a hydrogen bond by dynamic force spectroscopy, it is mandatory to formulate a theoretical model that serves as fundament for a correct interpretation of the experimental data, as well as basis for simulations and stochastic calculations. Theories based on diffusive barrier crossing with a fluctuating cantilever assume either a one-well potential, when no rebinding is taken into account, or a two-well potential when rebinding is included.[157] Based on these theoretical approaches, Monte Carlo simulations were performed and the input parameters were adapted to the experimental data to correctly describe the transition process.[158] The obtained parameters were used as presettings in stochastic calculations. Results of the calculations were compared with the experimental data as benchmark of the reliability of the theoretical model.

Figure 47 shows the combined results of force distance experiments (blue bars), Monte Carlo simulations (red dots) and stochastic calculations (black line) for loading rates with 60 pN/s (upper part) and 30 000 pN/s (lower part). The simulations are in good accordance with the experimental data; in addition, the stochastic calculations, based on the parameter settings from the Monte Carlo simulations, support the integrity of the obtained parameters. However, the skewness of the experimentally obtained force histograms are opposite from what is expected from theory.[159] This has been attributed largely to a distribution of transition rates due to chemical bond heterogeneity.[160] As reasons for bond heterogeneity, orientational variations of the stretched molecules relative to the direction of the applied load and fluctuations of the local molecular environment, mainly solvent molecules, can be accounted for.

[157] Hummer and Szabo (2003); Li and Leckband (2006)
[158] Programming of the Monte Carlo algorithm was performed by Prof. Dr. A. Janshoff.
[159] Dudko *et al.* (2003); Dudko *et al.* (2006); Evans and Ritchie (1997); Hummer and Szabo (2003)
[160] Raible *et al.* (2006); Raible and Reimann (2006)

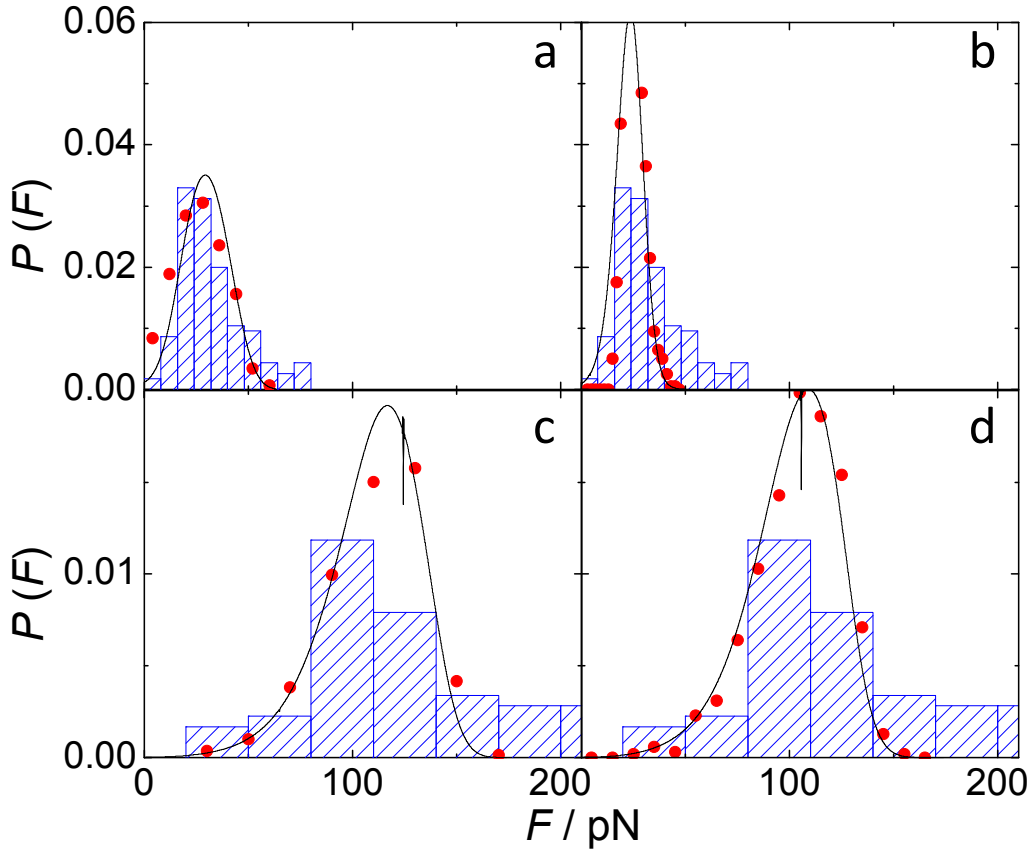


**Figure 47:** Probability distributions ($n$ = 1000) of bond rupture under external load of experimental data (blue bars), stochastic calculations (black line) and results of Monte Carlo simulations (red dots). **(a/b)** Loading rate: 60 pN/s, $\kappa_S$ = 0.006 N/m, time step $\Delta t$ = 15 ns. **(c/d)** 30 000 pN/s, $\kappa_S$ = 0.03 N/m, $\Delta t$ = 0.1 ns,. Simulations and calculations based either on a one-well potential **(a/c)**, or on a two-state potential **(b/d)**, allowing rebinding due to thermal fluctuations. For the simulations and stochastic calculations following parameter settings were used: $D$ = 2000 nm$^2$/s; **a)** $x_T$ = 0.28 nm, $\kappa_{m1}$ = 1.55 N/m, $\Delta G_{A\to T}$ = 13.7 kT. **b)** $x_T$ = 0.275 nm, $\kappa_{m1}$ = 1.1 N/m, $\kappa_{m2}$= 0.07 N/m, $\Delta G_{A\to T}$ = 10.9 kT. **c)** $x_T$ = 0.31 nm, $\kappa_{m1}$= 1.2 N/m, $\Delta G_{A\to T}$ = 12.1 kT. **d)** $x_T$ = 0.3 nm, $\kappa_{m1}$ = 1.1 N/m, $\kappa_{m2}$ = 0.04 N/m, $\Delta G_{A\to T}$ = 12.2 kT.

The parameters obtained from simulations and calculations based on a one-well cusp-like potential, which does not take rebinding processes into account (left side), differ from the parameters of the two-well potential (right side). This disparity is conform with the aspect of rebinding due to fluctuations, even while pulling the molecule, as observed in the experiments in form of pronounced force plateaus. Thus, a two-well potential reflects the experiments better. In figure 48, a MC-simulated force curve is shown. The simulation is based on a two-well potential, thus, rebinding while stretching is possible and clearly observable in the simulated curve. While in simulations based on a one-well potential the rupture force reflects the first crossing of the barrier, two-well potential simulations detect the last crossing into the unbound state as rupture force. Thus, when using the same parameters, two-

well simulations yield in higher rupture forces than one-well simulations as shown in figure 49.

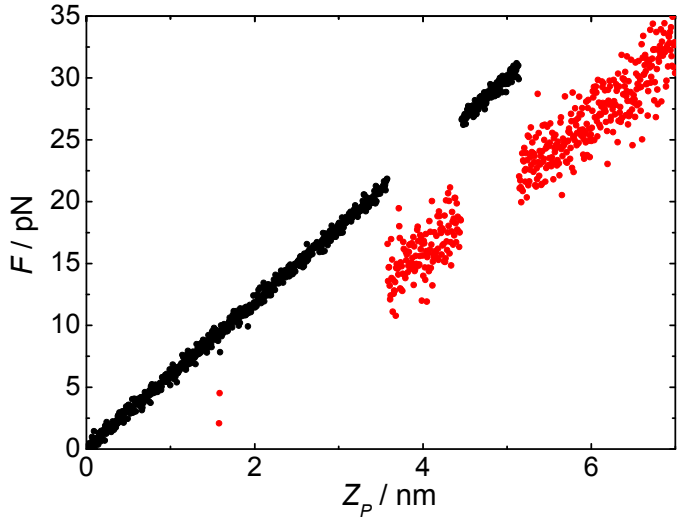


**Figure 48:** Example of a MC-simulated force curve, based on a two-well potential at 60 pN/s. Red dots indicate a crossing of the transition barrier. As rupture force 29 pN was automatically detected.
Following parameters were used: $\Delta t$ = 15 ns, $\kappa_S$ = 0.006 N/m, $D$ = 2000 nm$^2$/s, $x_T$ = 0.29 nm, $\kappa_{m1}$ = 1.1 N/m, $\kappa_{m2}$= 0.05 N/m.

The impact of the rebinding process due to thermal fluctuations of the cantilever is especially important at small loading rates as demonstrated exemplarily in figure 49.

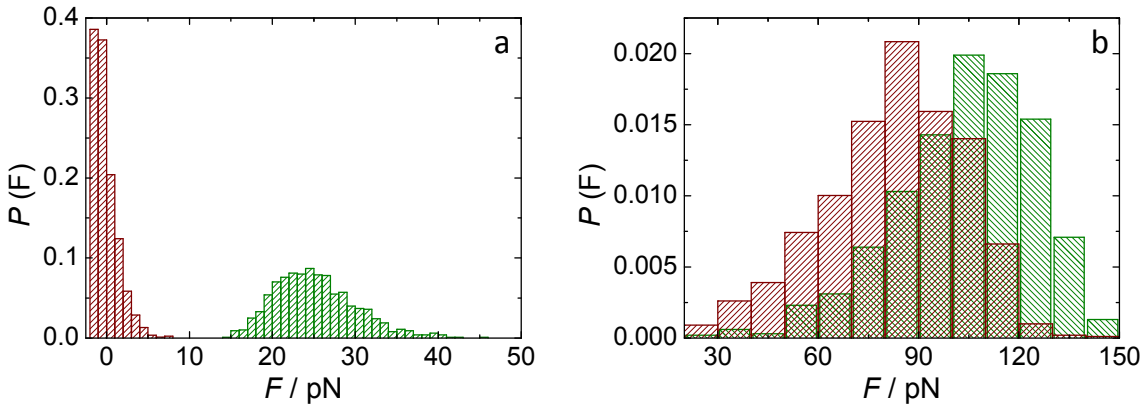


**Figure 49:** Probability distributions ($n$ = 1000) of simulations of bond rupture based either on a one-well potential (red bars), or on a two-state potential (green bars) with the same parameter settings.
**a)** 60 pN/s, $\kappa_S$ = 0.006 N/m, $\Delta t$ = 15 ns; $x_T$ = 0.275, $\kappa_{m1}$= 1.1 N/m, $\kappa_{m2}$ = 0.05 N/m.
**b)** 30 000 pN/s, $\kappa_S$ = 0.03 N/m, $\Delta t$ = 0.1 ns; $x_T$ = 0.3, $\kappa_{m1}$ = 1.1 N/m, $\kappa_{m2}$ = 0.05 N/m.

At 30000 pN/s the simulated probability distributions of one-well and two-well potentials overlap with each other, whereas at 60 pN/s no overlapping occurs, confirming the decreasing significance of rebinding during stretching with higher loading rates. In addition, an increasing width of the distribution at higher loading rates is clearly observable, e.g. the simulated two-well rupture forces exhibit a RMS devia-

tion of ±5 pN at 60 pN/s, respectively ±21 pN at 30 000 pN/s. This broadening at higher loading rates is also observed in the experiments as shown in figure 47 (blue bars).

In the experimentally obtained rupture force histograms, a bimodal substructure was observed at some loading rates: e.g. at 1500 pN/s two force maxima are clearly observable which could only be adequately achieved in the simulations with two different parameter settings for the first and second maximum (figure 50), indicating the presence of an intermediate state or two categories of hydrogen bonds.

Further evidence of a more sophisticated rupturing mechanism of the 16 hydrogen bonds is given by the obvious bimodal structure in the histograms of the extensions in length per rupture event (figure 43, p. 89).

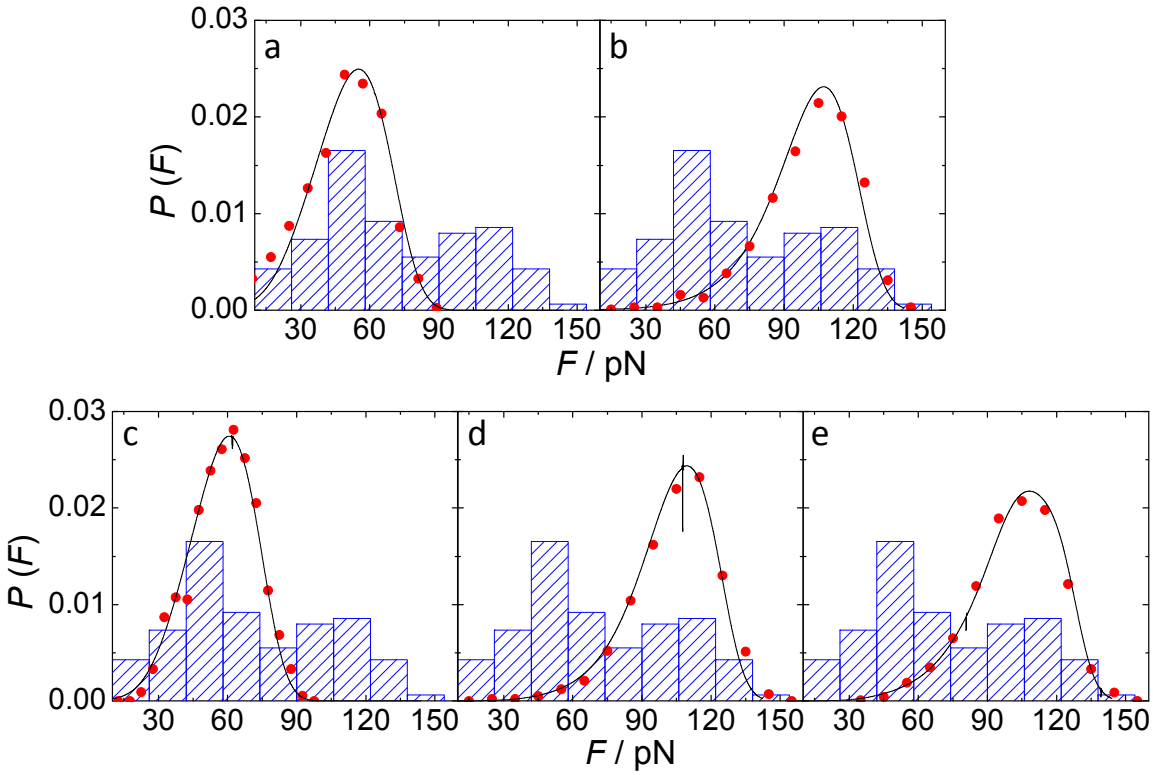


**Figure 50:** Probability distributions ($n$ = 1000) of bond rupture under external load of experimental data (blue bars), stochastic calculations (black line), and results of Monte Carlo simulations (red dots) at a loading rate of 1500 pN/s, $\kappa_S$ = 0.03 N/m. Simulations and calculations based either on a one-well potential **(a/b)**,[161] or on a two-state potential **(c-e)**, allowing rebinding due to thermal fluctuations.[162] The simulations and stochastic calculations were adjusted either to the first **(a/c)** or second maximum **(b, d, e)**. Following parameter settings were used: $D$ = 2000 nm$^2$/s, $\Delta t$ = 1 ns. **a)** $x_T$ = 0.3 nm, $\kappa_{m1}$ = 1.21 N/m, $\Delta G_{A\to T}$ = 12.6 kT. **b)** $x_T$ = 0.365 nm, $\kappa_{m1}$ = 1.1 N/m, $\kappa_{m2}$ = 0.048 N/m, $\Delta G_{A\to T}$ = 17.7 kT. **c)** $x_T$ = 0.3 nm, $\kappa_{m1}$ = 1.1 N/m, $\kappa_{m2}$ = 0.05 N/m, $\Delta G_{A\to T}$ = 12.2 kT. **d)** $x_T$ = 0.35 nm, $\kappa_{m1}$ = 1.1 N/m, $\kappa_{m2}$ = 0.04 N/m, $\Delta G_{A\to T}$ = 16.6 kT. **e)** $x_T$ = 0.3 nm,$\kappa_{m1}$ = 1.4 N/m, $\kappa_{m2}$ = 0.02 N/m, $\Delta G_{A\to T}$ = 15.6 kT.

[161] Hummer and Szabo (2003)
[162] Li and Leckband (2006)

To support the interpretation of the experimental results, MD simulations of the molecule under external load were performed and compared qualitatively with the experiments.[163] The MD simulations of the force distance experiments were performed with time steps of 0.0001 ps and a total simulation time of 2 – 2.5 ns, thermally equilibrated at 300 K or 460 K. As shown in the experimental section, solvent molecules (mesitylene) had no effect on the experiment. Thus, they were not considered in the simulation.

Figure 51 shows a single pulling trajectory obtained from MD simulation, which displays two distinct length jumps. The first sudden contour length increase could safely be attributed to hydrogen bond breakage as the jump of the reaction coordinate exceeds by far the typical threshold for H-bonds (0.3 nm), while the second, smaller step was assigned to a barrier that originates from a sterically locked conformation. Notably, this barrier was visible in more than 76 % of all simulations.

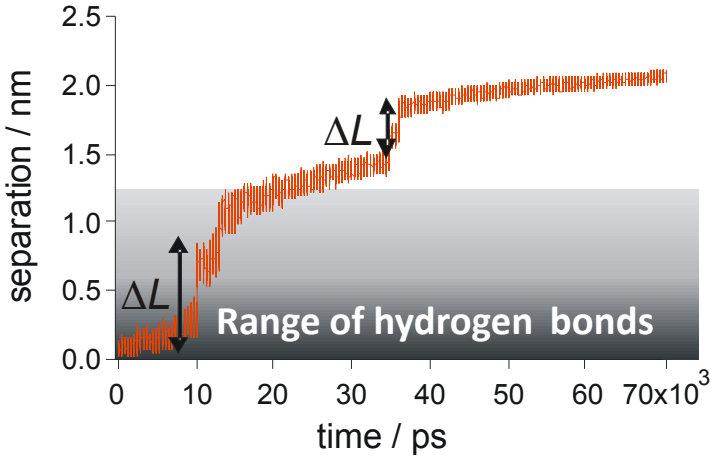


**Figure 51:** Separation of two calixarene monomers as a function of time obtained from a single MD simulation.

Figure 52 compiles the results of the sudden contour-length increase $\Delta L$ upon pulling as obtained from 80 trajectories. Both, the experimental histogram (figure 52 a) and the one obtained from MD simulations (figure 52 b) show two distinct jumps in contour length at roughly 1 and 2 nm indicative of a reasonable stable intermediate state.

[163] MD simulations were performed by Dr. T. Metzroth, group of Prof. Dr. J. Gauß, Institute of Physical Chemistry, Johannes-Gutenberg University of Mainz, using the GROMACS 3.2 program package.

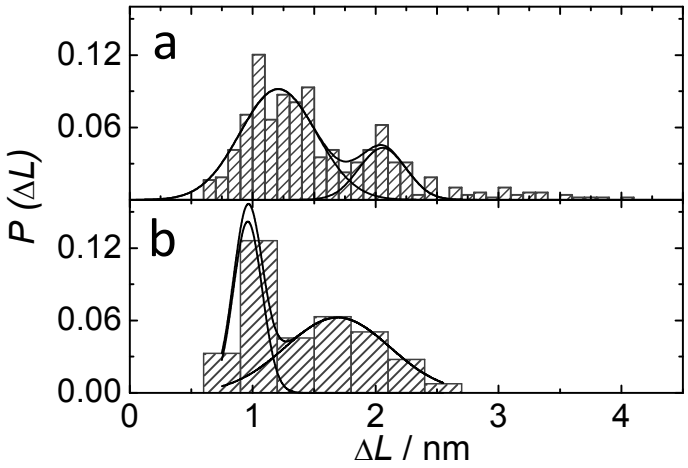


**Figure 52:** Histograms of dimer separation $\Delta L$ from **a)** force distance experiments at 1500 pN/s and **b)** MD simulations. Fitting of two Gaussian functions to the corresponding histograms $P(L)$ provide mean separations $\Delta L$ at (1.2 ± 0.01) nm and (2.05 ± 0.02) nm for experimental force curves and (0.9 ± 0.14) nm and (1.7 ± 0.05) nm for MD simulations.

To prove that the intermediate exhibits an experimentally observable stability, prolonged simulations (> 10 ns) at elevated temperature (460 K) and fixed force were performed and revealed a consistent intermediate state as well.

Figure 53 shows typical conformations of the strained dimers captured by MD simulations at various times with the intermediate state located in the centre of figure 53 at 1 ns.

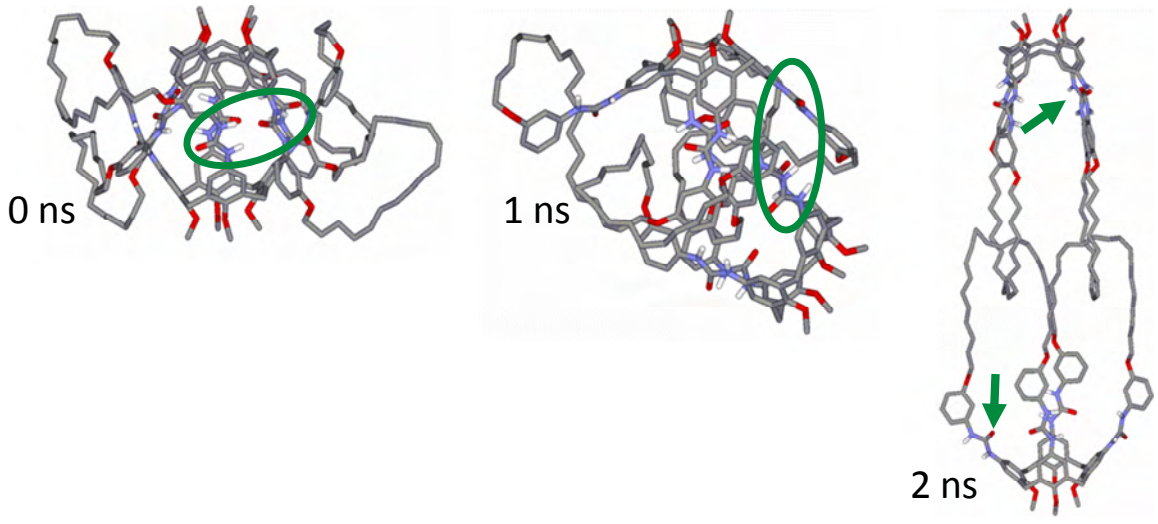


**Figure 53:** Snapshots of the calixarene-catenanes under harmonic load at various times with the intermediate state kinetically trapped, shown at 1 ns. The green circles and arrows emphasize hydrogen bonding exemplarily between urea functions (white: H-atoms, red: O-atoms).

The unequivocal assignment of an intermediate state in a mechanical single molecule experiment is rare and difficult.[164] Although some studies reported on the occurrence of a nonlinear relationship of the rupture force and the logarithm of the loading rate and attributed this deviation from Bell's phenomenological approach[165] to the presence of a second or third inner barrier,[166] only few reports are available where more or less stable intermediate states were captured by force spectroscopy.[167] A nonlinear relationship between $<F_{rup}>$ and ln ($dF/dt$) does not necessarily imply the presence of additional energy barriers but could be rather a consequence of an intrinsic feature of diffusive barrier crossing with a fluctuating cantilever as explained in the theory section (figure 36).

Another important conclusion of the MD simulations is the identification of a successively, zipper-like bond breakage of the 16 hydrogen bonds of a dimeric capsule. This non-concerted rupturing behavior was already expected from the relatively low yield forces of the experiments. Thus, the conception of eight strong and eight weak hydrogen bonds, instead of an intermediate state of each individual hydrogen bond, is ruled out.

Corresponding to the extraction of relevant parameters from the energy landscape, an intermediate state in the hydrogen bonding mechanism demands the concept of a three-well potential whose implementation in stochastic calculations leads to an exceeding complexity in the formulation and solution of the differential equations to calculate the probability distribution of such a rupture mechanism. An example of successful fitting the bimodal probability distribution of the experimental data with a three-well simulation is shown in figure 54.

[164] Marszalek *et al.* (1999); Onoa *et al.* (2003); Schlierf and Rief (2005); Williams *et al.* (2003)
[165] Bell (1978); Evans and Ritchie (1997)
[166] Merkel *et al.* (1999)
[167] Schlierf and Rief (2005); Williams *et al.* (2003)

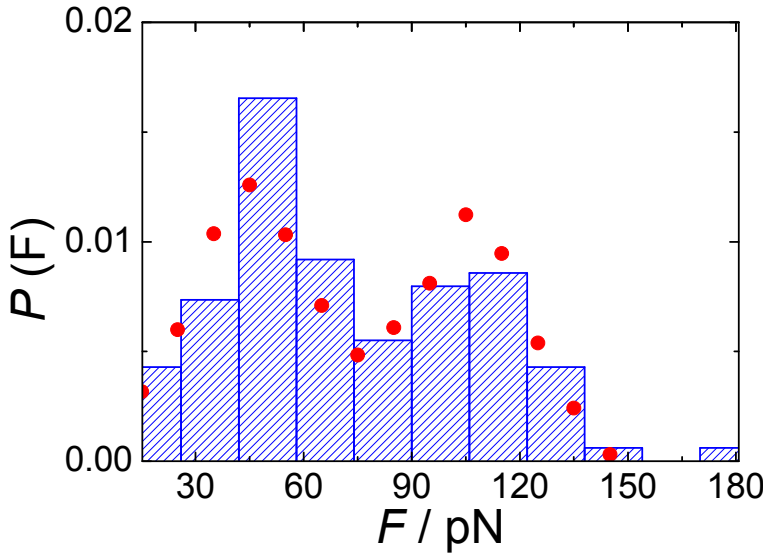


**Figure 54:** Probability distributions of bond rupture under external load of experimental data (blue bars) and Monte Carlo simulations (red dots), based on a three-well potential, at a loading rate of 1500 pN/s, $\kappa_S$ = 0.03 N/m. Following parameter settings were used: $D$ = 2000 nm$^2$/s, MC simulations n = 1000, $\Delta t$ = 5 ns, $x_I$ = 0.55 nm, $x_B$ = 1.25 nm, $x_{T1}$ = 0.31 nm, $x_{T2}$ = 0.86 nm, $\kappa_{m1}$ = 1.1 N/m, $\kappa_{m2}$ = 1.404 N/m, $\kappa_{m3}$ = 0.833 N/m, $G_{A\rightarrow T1}$ = 13.1 kT, $\Delta G_{I\rightarrow T2}$ = 22.0 kT.

This example, at a loading rate of 1500 pN/s, clearly demonstrates the successful adaptation of a three-well potential to the experimental data, indicating an intermediate state in the rupture mechanism of hydrogen bond breakage.

Optimization of parameters yielded in approximate locations for the first barrier ($\Delta G_{A\rightarrow T1}$ = 13.1 kT) at $x_{T1}$ = 0.31 nm and the second one ($\Delta G_{I\rightarrow T2}$ = 22.0 kT) at $x_{T2}$ = 0.86 nm in good accordance with results from MD simulations.

To illustrate the effect of an applied force ramp ($F = \kappa_S \cdot vt$) on the shape of a three-well energy potential, figure 55 envisions the potential without load in red and a tilted potential due to applied load in blue, based on the considerations as stated in chapter 5.3. The mechanical lock provided by the two entangled loops forces the potential, i.e. the position of the transition state with respect to the bound and unbound states, into a higher symmetry.[168] As a consequence, opening of the nanocapsules is reversible.

[168] Rief *et al.* (1998)

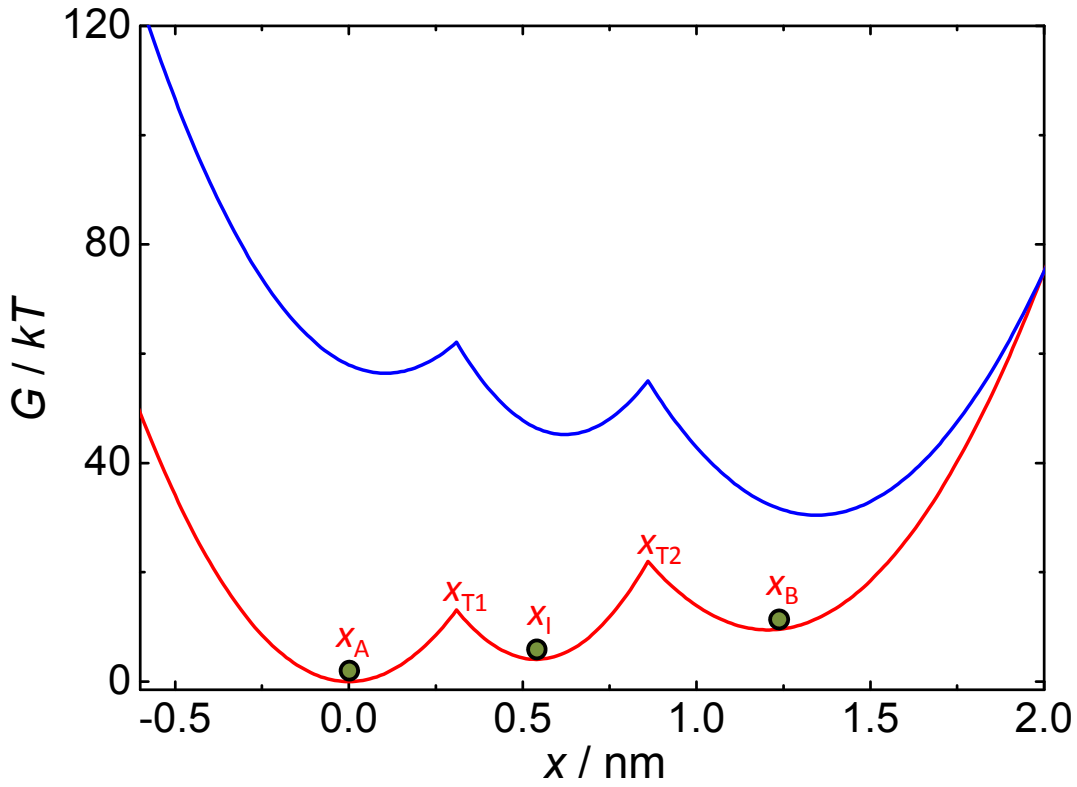


**Figure 55:** Calculated three-well potentials at an applied force of 0 nN (red line) and elevated force of 0.12 nN (blue line) with the parameter settings from the MC simulations of figure 54: $x_{\mathrm{I}}$ = 0.55 nm, $x_{\mathrm{B}}$ = 1.25 nm, $x_{\mathrm{T1}}$ = 0.31 nm, $x_{\mathrm{T2}}$ = 0.86 nm, $\kappa_{m1}$ = 1.1 N/m, $\kappa_{m2}$ = 1.404 N/m, $\kappa_{m3}$ = 0.833 N/m, $\Delta G_{\mathrm{A}\rightarrow\mathrm{T1}}$ = 13.1 kT, $\Delta G_{\mathrm{I}\rightarrow\mathrm{T2}}$ = 22.0 kT.

In principle, the final state $x_{\mathrm{B}}$ can be reached via two pathways, either directly from $x_{\mathrm{A}}$ to $x_{\mathrm{B}}$ with transition rate $k_{\mathrm{AB}}$ or the molecule arrests at the kinetic barrier at $x_{T2}$, giving rise to a stable intermediate $x_{\mathrm{I}}$. It should be noted that two distinct maxima are not clearly revealed at all loading rates probably due to the occurrence of distributed transition rates as pointed out by Raible *et al.* (figure 42, p. 88).[169] However, a similar behavior is expected from the occurrence of an intermediate state emphasized by the fact that the rejoining force histograms also display a pronounced broadness which cannot be explained in terms of distributed transition rates alone but is rather an indication of the presence of intermediate states. Hence, the inverted skewness of the experimentally obtained histograms can be attributed to a second maximum at higher forces that is intermingled with the first one and changes the overall shape of the histogram. Figure 56 shows that slight changes in the parameter settings of the three-well simulations result in merged maxima of the rupture force probability distributions.

[169] Raible *et al.* (2006)

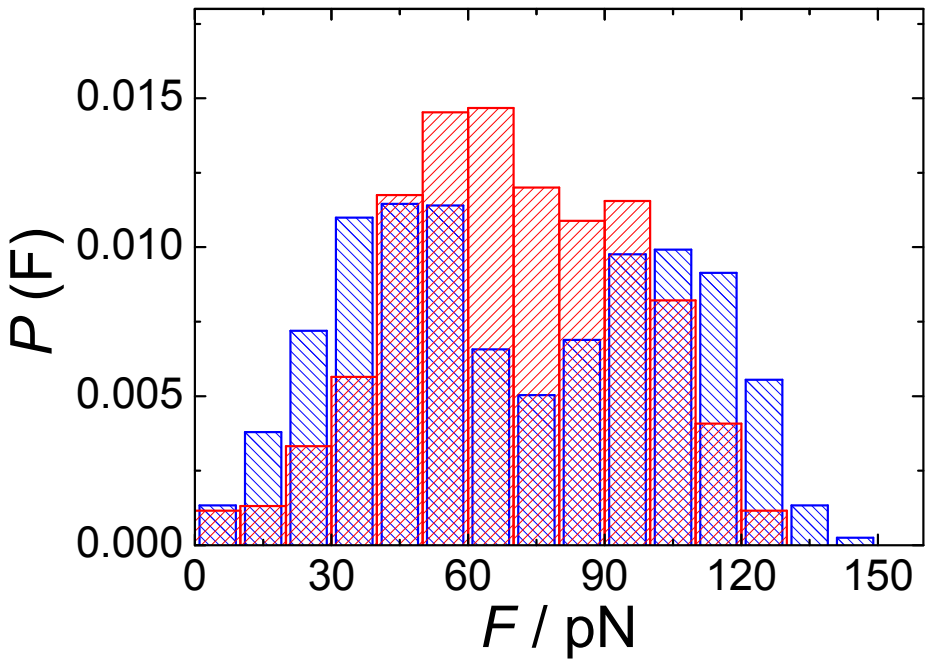


**Figure 56:** Monte Carlo simulations of bond rupture probability distributions, based on a three-well potential, at a loading rate of 1500 pN/s, $\kappa_S$ = 0.03 N/m,. Except $\kappa_{m2}$ (blue: 1.548 N/m, red 1.476 N/m) and $\kappa_{m3}$ (blue: 0.627 N/m, red 0.664 N/m) all parameters are equal. However, the red histogram hardly exhibits a bimodal structure. Following parameter settings were used for both simulations: $\Delta t$ = 1 ns, $D$ = 2000 nm$^2$/s, MC simulations $n$ = 1000, $x_{\mathrm{I}}$ = 0.55, $x_{\mathrm{B}}$ = 1.25, $x_{\mathrm{T1}}$ = 0.31 nm, $x_{\mathrm{T2}}$ = 0.84 nm, $\kappa_{m1}$ = 1.1 N/m.

The more familiar and robust way to analyze force spectroscopy data is displayed in figure 57. Here, the mean rupture and rejoining forces obtained from the histograms are plotted as a function of loading rate on a semi logarithmic scale. Close to the equilibrium, $<F_{\mathrm{rup}}>$ and $<F_{\mathrm{rejoin}}>$ converge towards the identical value independent of the loading rate resulting in nonlinear functions of $\ln(\mathrm{d}F/\mathrm{d}t)$. Since the wide range of loading rates was realized using two different cantilever spring constants (0.006 N/m and 0.03 N/m) the curves are not continuous.

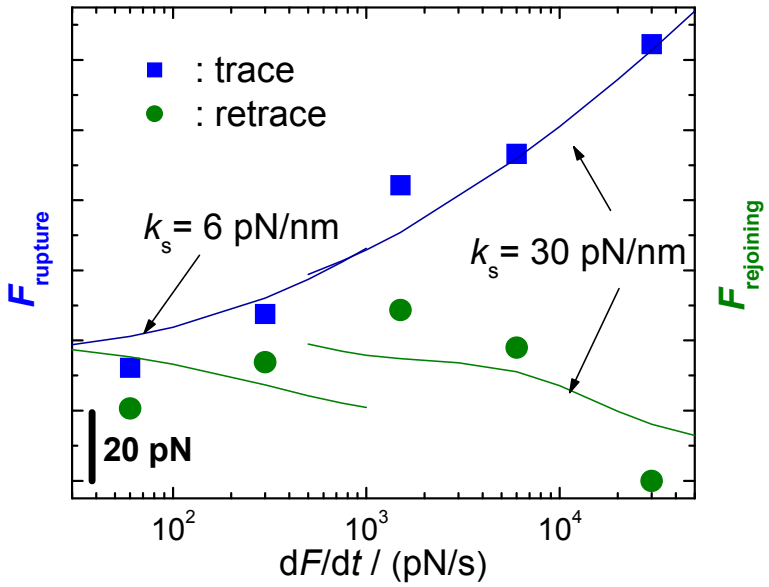


**Figure 57:** Mean rupture (■) and rejoining forces (●) computed from the histograms displayed in figure 42 (p. 88), together with the stochastic modeling. [170] The blue lines represent the mean rupture force, while the green lines are the mean rejoining forces. Since two different cantilevers with force constants of 0.006 N/m and 0.03 N/m have been used, the computed curves are not continuous. Only molecules with a contour length smaller than 22 nm were selected in these histograms to reduce the influence of a soft linker. Following parameters were obtained: $x_I$ = 0.8 nm, $x_B$ = 1.4, $x_{T1}$ = 0.3 nm, $x_{T2}$ = 1.1 nm, $k_{m1}$ = $10^3$ pN/nm, $k_{m2}$ = $10^4$ pN/nm, $k_{m3}$ = $10^2$ pN/nm.

In conclusion, entangled nanocapsules are the ideal tuneable model system for investigating the strength of hydrogen bonds on a single molecule level with adjustable reversibility imposed by loops serving as distance limiting suspensors.

Based on the Molecular Dynamics and Monte Carlo simulations, in conjunction with stochastic calculations, a three-well potential of the individual hydrogen bonds is proposed. and the relevant parameters were successfully extracted from the experimental data.

[170] Stochastic modeling was conducted by Prof. Dr. G. Diezemann, Prof. Dr. J. Gauß, Institute of Physical Chemistry, Johannes-Gutenberg University of Mainz.

# 6 SUMMARY

The objective of this work was to create, verify, and scrutinize suitable model systems for the investigation of fundamental biophysical mechanisms ranging from adhesion, established by multiple protein-protein interactions, down to the analysis of reversible intramolecular rupture and rebinding of single hydrogen bonds in artificial macromolecules.

In the first project, the interaction between the plasma membrane and the actin cytoskeleton was quantified by a novel biohybrid model system. Of particular interest was the activation mechanism of ezrin, a molecular linker which, in its dormant form, is not capable of binding actin filaments. Besides quartz crystal microbalance (QCM), epifluorescence microscopy, and ellipsometry, atomic force microscopy (AFM) was the main technique employed, because it enabled the visualization and characterization of the model system and subsequently the realization of force spectroscopy experiments with piconewton resolution.

At first, the adsorption of ezrin was investigated on solid-supported membranes, doped with either the natural anchor lipid $PIP_2$ or the synthetic anchor lipid DOGS Ni-NTA via a His tag at the N-terminal domain of ezrin. A highly specific and cooperative adsorption behavior of ezrin on $PIP_2$-membranes was explored by AFM and QCM. Dependent on the ratio of uniformly distributed $PIP_2$ in the membrane, different amounts of surface coverage of adsorbed ezrin were successfully quantified, displaying an almost complete protein coverage at $PIP_2$ concentrations of 3 mol% and larger.

To imitate the cytoskeleton, a cantilever equipped with a colloidal probe was covered with gold, subsequently functionalized with a positively charged self-assembly layer ($AUT^+$) and finally coated with actin filaments. The F-actin coverage was validated by epifluorescence microscopy and revealed that the yield of successfully functionalized probes was substantially larger if colloidal probes instead of commercial AFM tips were used.

Finally, force distance experiments with F-actin functionalized probes on ezrin-covered membranes were conducted to measure quantitatively the maximal adhesion forces and the work of adhesion at the ezrin–F-actin interface. The work of adhesion was substantially larger when ezrin was bound to the solid-supported mem-

brane via $PIP_2$ than with ezrin linked to the membrane via the artificial lipid DOGS Ni-NTA. This finding was confirmed qualitatively by epifluorescence microscopy employing fluorescently labelled F-actin. Thus, an activation of ezrin as a consequence of binding solely to $PIP_2$ can be concluded. Additional cofactors may emphasize, stimulate or stabilize the activation but are not essentially required for triggering ezrin's transformation into an active conformation.

In the second project, single molecule force spectroscopy was performed on a novel, entirely artificial molecule architecture of oligomerized bis-loop tetra-urea calix[4]arene-catenanes. These macromolecules were specifically designed for AFM force distance experiments to mimic the unfolding and refolding processes of more complex structures, e.g. proteins. Focus of this investigation was on the rupture and rejoining mechanism of intramolecular hydrogen bridges that were rendered reversible by mechanically locking the unbound state due to entangled intramolecular loops of dimeric capsules.

Hence, the extension and reformation of individual capsules, containing 16 intramolecular hydrogen bridges, was examined by force distance experiments with different pulling speeds (loading rates). The experimental results were used in combination with Molecular Dynamics (MD) simulations to establish and verify theoretical models of the mechanism of hydrogen bond rupture. Based on theories of diffusive barrier crossing driven by an external load, Monte Carlo simulations as well as stochastic modeling were successfully used to determine all relevant kinetic parameters of the energy potential from the experimental data.

At first, a one-well cusp-like potential was assumed as theoretical model, without taking rebinding into account, which turned out to be inadequate due to thermal fluctuations of the cantilever that enabled rebinding even while the molecule was stretched. Thus, a two-well potential, which included the possibility of rebinding during the stretching process, better reflected the experimental data.

However, the experimentally obtained rupture force histograms featured a bimodal substructure at some loading rates, indicating the presence of an intermediate state. A bimodal structure was also perceived in the histograms of the extensions in length per rupture event. This gave further evidence of a more sophisticated rupturing mechanism of the 16 hydrogen bonds per capsule. By means of MD simulations a second transition barrier was distinguished, originating from a sterically locked

conformation. In addition, MD simulations indicated a zipper-like rupture mechanism of the 16 hydrogen bonds, confirming the rather low rupture forces of the experiments.

The existence of an intermediate state in the hydrogen bonding mechanism required the concept of a three-well potential, which was included in the Monte Carlo simulations, leading to a successful adaption of the simulations to the rupture force distribution in order to obtain relevant parameters of the energy potential.

In summary, it can be stated that atomic force microscopy is an invaluable tool to scrutinize relevant processes in nature, such as investigating activation mechanisms in proteins, as shown by analysis of the interaction between F-actin and ezrin, as well as exploring fundamental properties of single hydrogen bonds that are of paramount interest for the complete understanding of complex supramolecular structures.

J. Alcaraz *et al.* (2002) Correction of microrheological measurements of soft samples with atomic force microscopy for the hydrodynamic drag on the cantilever. *Langmuir* 18: 716-721.

I. Alfonso and V. Gotor (2004) Biocatalytic and biomimetic aminolysis reactions: useful tools for selective transformations on polyfunctional substrates. *Chem. Soc. Rev.* 33: 201-209.

E. Auvinen, N. Kivi and A. Vaheri (2007) Regulation of ezrin localization by Rac1 and PIPK in human epithelial cells. *Exp. Cell Res.* 313: 824-833.

G. Bao and S. Suresh (2003) Cell and molecular mechanics of biological materials. *Nature Materials* 2: 715-725.

C. Barret *et al.* (2000) Mutagenesis of the phosphatidylinositol 4,5-bisphosphate ($PIP_2$) binding site in the $NH_2$-terminal domain of ezrin correlates with its altered cellular distribution. *J. Cell Biol.* 151: 1067-1080.

T. H. Bayburt, J. W. Carlson and S. G. Sligar (2000) Single molecule height measurements on a membrane protein in nanometer-scale phospholipid bilayer disks. *Langmuir* 16: 5993-5997.

G. I. Bell (1978) Models for the specific adhesion of cells to cells. *Science* 200: 618-627.

M. Benoit, T. Holstein and H. E. Gaub (1997) Lateral forces in AFM imaging and immobilization of cells and organelles. *European Biophysics Journal* 26: 283-290.

M. Berryman, R. Gary and A. Bretscher (1995) Ezrin oligomers are major cytoskeletal components of placental microvilli: a proposal for their involvement in cortical morphogenesis. *J. Cell Biol.* 131: 1231-1242.

G. Binnig, C. F. Quate and C. Gerber (1986) Atomic Force Microscope. *Phys. Rev. Lett.* 56: 930.

G. Binnig and H. Rohrer (1987) Scanning tunneling microscopy - from birth to adolescence. *Review of Modern Physics* 59: 615.

G. Blin *et al.* (2008) Quantitative analysis of the binding of ezrin to large unilamellar vesicles containing phosphatidylinositol(4,5)- bisphosphate. *Biophys. J.* 94: 1021-1033.

V. Böhmer (1995) Calixarenes, macrocycles with (almost) unlimited possibilities. *Angew. Chem. Int. Ed.* 34: 713-745.

C. Bouchiat *et al.* (1999) Estimating the persistence length of a worm-like chain molecule from force-extension measurements. *Biophys. J.* 76: 409-413.

A. C. Branka and D. M. Heyes (1998) Algorithms for Brownian dynamics simulation. *Physical Review E* 58: 2611.

A. Bretscher (1983) Purification of an 80,000-dalton protein that is a component of the isolated microvillus cytoskeleton, and its localization in nonmuscle cells. *J. Cell Biol.* 97: 425-432.

A. Bretscher, K. Edwards and R. G. Fehon (2002) ERM proteins and merlin: integrators at the cell cortex. *Nat. Rev. Mol. Cell Biol.* 3: 586-599.

A. Bretscher, R. Gary and M. Berryman (1995) Soluble ezrin purified from placenta exists as stable monomers and elongated dimers with masked C-terminal ezrin-radixin-moesin association domains. *Biochemistry* 34: 16830-16837.

M. S. Brody, C. A. Schalley, D. M. Rudkevich and J. Rebek (1999) Synthesis and characterization of a unimolecular capsule. *Angew. Chem. Int. Ed.* 38: 1640-1644.

N. A. Burnham *et al.* (1997) How does a tip tap? *Nanotechnology* 8: 67-75.

H.-J. Butt, B. Cappella and M. Kappl (2005) Force measurements with the atomic force microscope: Technique, interpretation and applications. *Surface Science Reports* 59: 1-152.

H. J. Butt and M. Jaschke (1995) Calculation of thermal noise in atomic force microscopy. *Nanotechnology* 6: 1-7.

B. Cappella and G. Dietler (1999) Force-distance curves by atomic force microscopy. *Surface Science Reports* 34: 1-104.

M. Carrion-Vazquez *et al.* (1999) Mechanical and chemical unfolding of a single protein: A comparison. *Proceedings of the National Academy of Sciences* 96: 3694-3699.

D. N. Chambers and A. Bretscher (2005) Ezrin mutatns affecting dimerization and activation. *Biochemistry* 44: 3926-3932.

Y.-T. Cheng and D. E. Rodak (2005) Is the lotus leaf superhydrophobic? *Applied Physics Letters* 86: 144101-3.

J. P. Cleveland, S. Manne, D. Bocek and P. K. Hansma (1993) A nondestructive method for determining the spring constant of cantilevers for scanning force microscopy. *Review of Scientific Instruments* 64: 403-405.

D. Collin *et al.* (2005) Verification of the Crooks fluctuation theorem and recovery of RNA folding free energies. *Nature* 437: 231-234.

J. A. Cooper *et al.* (1983) Kinetic evidence for a monomer activation step in actin polymerization. *Biochemistry* 22: 2193-2202.

R. G. Cox and H. Brenner (1967) The slow motion of a sphere through a viscous fluid towards a plane surface. *Chemical Engineering Science* 22: 1753-1777.

G. E. Crooks (1999) Entropy production fluctuation theorem and the nonequilibrium work relation for free energy differences. *Physical Review E* 60: 2721.

A. F. Danil de Namor (1993) Thermodynamics of supramolecular systems: Recent developments. *Pure and Applied Chemistry* 65: 193-202.

J. T. Davis and G. P. Spada (2007) Supramolecular architectures generated by self-assembly of guanosine derivatives. *ChemInform* 38.

G. Denisov *et al.* (1998) Binding of basic peptides to membranes produces lateral domains enriched in the acidic lipids phosphatidylserine and phosphatidylinositol 4,5-bisphosphate: an electrostatic model and experimental results. *Biophys. J.* 74: 731-744.

H. Dietz and M. Rief (2004) Exploring the energy landscape of GFP by single-molecule mechanical experiments. *Proceedings of the National Academy of Sciences* 101: 16192-16197.

Y. Doi *et al.* (1999) Normal development of mice and unimpaired cell adhesion/cell motility/actin-based cytoskeleton without compensatory up-regulation of ezrin or radixin in moesin gene knockout. *J. Biol. Chem.* 274: 2315-2321.

M. J. Doktycz and M. L. Simpson (2007) Nano-enabled synthetic biology. *Mol Syst Biol* 3.

W. A. Ducker, T. J. Senden and R. M. Pashley (1991) Direct measurement of colloidal forces using an atomic force microscope. *Nature* 353: 239-241.

O. K. Dudko, A. E. Filippov, J. Klafter and M. Urbakh (2003) Beyond the conventional description of dynamic force spectroscopy of adhesion bonds. *Proceedings of the National Academy of Sciences* 100: 11378-11381.

O. K. Dudko, G. Hummer and A. Szabo (2006) Intrinsic rates and activation free energies from single-molecule pulling experiments. *Physical Review Letters* 96: 108101-4.

R. Eckel *et al.* (2005) Supramolecular chemistry at the single molecule level. *Angew. Chem. Int. Ed.* 44: 484-488.

E. Evans and F. Ludwig (2000) Dynamic strengths of molecular anchoring and material cohesion in fluid biomembranes. *Journal of Physics: Condensed Matter* 12: A315-A320.

E. Evans and K. Ritchie (1997) Dynamic strength of molecular adhesion bonds. *Biophys. J.* 72: 1541-1555.

E. Evans and K. Ritchie (1999) Strength of a weak bond connecting flexible polymer chains. *Biophys. J.* 76: 2439-2447.

S. Faiß (2007) Untersuchung der lateralen Organisation und Phasenumwandlung von festkörperunterstützten Lipidmembranen, PhD thesis

S. Faiss *et al.* (2008) Phase transition of individually addressable microstructured membranes visualized by
imaging ellipsometry. *J. Phys. Chem. B* (in press).

J. M. Fernandez and H. Li (2004) Force-clamp spectroscopy monitors the folding trajectory of a single protein. *Science* 303: 1674-1678.

B. T. Fievet *et al.* (2004) Phosphoinositide binding and phosphorylation act sequentially in the activation mechanism of ezrin. *J. Cell Biol.* 164: 653-659.

P. J. Flory (1969) Statistical mechanics of chain molecules. Interscience Publishers, New York.

S. Fong *et al.* (1996) Structure and stability of an immunoglobulin superfamily domain from twitchin, a muscle protein of the nematode caenorhabditis elegans. *Journal of Molecular Biology* 264: 624-639.

C. Friedsam, A. K. Wehle, F. Kuhner and H. E. Gaub (2003) Dynamic single-molecule force spectroscopy: bond rupture analysis with variable spacer length. *Journal of Physics: Condensed Matter* 15: S1709-S1723.

A. Gambhir *et al.* (2004) Electrostatic sequestration of $PIP_2$ on phospholipid membranes by basic/aromatic regions of proteins. *Biophys J.* 86: 2188–2207.

R. Garcia and R. Perez (2002) Dynamic atomic force microscopy methods. *Surface Science Reports* 47: 197-301.

R. Gary and A. Bretscher (1995) Ezrin self-association involves binding of an N-terminal domain to a normally masked C-terminal domain that includes the F-actin binding site. *Mol. Biol. Cell* 6: 1061-1075.

P. Gascard *et al.* (1991) Asymmetric distribution of phosphoinositides and phosphatidic acid in the human erythrocyte membrane. *Biochimica et Biophysica Acta (BBA) - Biomembranes* 1069: 27-36.

A. Gautreau, D. Louvard and M. Arpin (2000) Morphogenic effects of ezrin require a phosphorylation-induced transition from oligomers to monomers at the plasma membrane. *J. Cell. Biol.* 150: 193-204.

F. Giessibl, J. (2005) AFM's path to atomic resolution. *Materials Today* 8: 32-41.

F. Gittes, B. Mickey, J. Nettleton and J. Howard (1993) Flexural rigidity of microtubules and actin filaments measured from thermal fluctuations in shape. *J. Cell Biol.* 120: 923-934.

C. D. Gutsche (1989) Calixarenes. The Royal Society of Chemistry.

K. Hamada *et al.* (2000) Structural basis of the membrane-targeting and unmasking mechanisms of the radixin FERM domain. *EMBO J.* 19: 4449–4462.

J. M. Haugh, F. Codazzi, M. Teruel and T. Meyer (2000) Spatial sensing in fibroblasts mediated by 3' phosphoinositides. *J. Cell Biol.* 151: 1269-1280.

K. Hayashi, S. Yonemura, T. Matsui and S. Tsukita (1999) Immunofluorescence detection of ezrin/radixin/moesin (ERM) proteins with their carboxyl-terminal threonine phosphorylated in cultured cells and tissues. *J. Cell. Sci.* 112: 1149-1158.

S. Hembacher, F. J. Giessibl and J. Mannhart (2004) Force microscopy with light-atom probes. *Science* 305: 380-383.

A. Herrig (2007) Wechselwirkung von Ezrin mit $PIP_2$ -haltigen artifiziellen Membransystemen und mit F-Aktin, PhD thesis

A. Herrig *et al.* (2006) Cooperative adsorption of ezrin on $PIP_2$-containing membranes. *Biochemistry* 45: 13025-13034.

H. Holscher and U. D. Schwarz (2006) Q-controlled amplitude modulation atomic force microscopy in liquids: an analysis. *Applied Physics Letters* 89: 073117.

L. Huang, T. Y. Wong, R. C. Lin and H. Furthmayr (1999) Replacement of threonine 558, a critical site of phosphorylation of moesin in vivo, with aspartate, activates F-actin binding of moesin. Regulation of conformational changes *J. Biol. Chem.* 274: 12803-12810.

T. Hugel *et al.* (2001) Elasticity of single polyelectrolyte chains and their desorption from solid supports studied by AF; based single molecule force spectroscopy. *Macromolecules* 34: 1039-1047.

T. Hugel *et al.* (2001) Elasticity of Single Polyelectrolyte Chains and Their Desorption from Solid Supports Studied by AFM Based Single Molecule Force Spectroscopy. *Macromolecules* 34: 1039-1047.

S. C. Hughes and R. G. Fehon (2007) Understanding ERM proteins - the awesome power of genetics finally brought to bear. *Current Opinion in Cell Biology* 19: 51-56.

G. Hummer and A. Szabo (2001) From the Cover: Free energy reconstruction from nonequilibrium single-molecule pulling experiments. *Proceedings of the National Academy of Sciences* 98: 3658-3661.

G. Hummer and A. Szabo (2003) Kinetics from nonequilibrium single-molecule pulling experiments. *Biophys. J.* 85: 5-15.

J. L. Hutter and J. Bechhoefer (1993) Calibration of atomic-force microscope tips. *Review of Scientific Instruments* 64: 1868-1873.

J. Israelachvili and G. Adams (1977) Measurement of forces between two mica surfaces in aqueous electrolyte solutions in the range 0-100 nm. *J. Chem. Soc., Faraday Trans. I.* 74: 975-1000.

J. Jacob *et al.* (2004) Early collapse is not an obligate step in protein folding. *Journal of Molecular Biology* 338: 369-382.

M. Janke (2004) Molekulare Kontrolle der Adsorption, Adhäsion und Deformation von Liposomen auf funktionalisierten Oberflächen. *Diploma thesis*.

P. A. Janmey and U. Lindberg (2004) Cytoskeletal regulation: rich in lipids. *Nat. Rev. Mol. Cell Biol.* 5: 658-666.

H. Janovjak, J. Struckmeier and D. J. Müller (2004) Hydrodynamic effects in fast AFM single-molecule force measurements. *Europ. Biophys. J.* 34: 91-96.

A. Janshoff, M. Neitzert, Y. Oberdoerfer and H. Fuchs (2000) Force Spectroscopy of Molecular Systems - Single Molecule Spectroscopy of Polymers and Biomolecules. *Angew. Chem. Int. Ed.* 39: 3346-3374.

A. Janshoff, M. Neitzert, Y. Oberdoerfer and H. Fuchs (2000) Force spectroscopy of molecular systems - single molecule spectroscopy of polymers and biomolecules. *Angew. Chem. Int. Ed.* 39: 3346-3374.

A. Janshoff, M. Neitzert, Y. Oberdörfer and H. Fuchs (2000) Force Spectroscopy of Molecular Systems - Single Molecule Spectroscopy of Polymers and Biomolecules. *Angewandte Chemie* 39: 3212-3237.

C. Jarzynski (1997) Nonequilibrium equality for free energy differences. *Physical Review Letters* 78: 2690.

S. K. Kaliappan and B. Cappella (2005) Temperature dependent elastic-plastic behaviour of polystyrene studied using AFM force-distance curves. *Polymer* 46: 11416-11423.

D. Karevski (2006) Steps toward the foundations of statistical mechanics: in and out of equilibrium. *Condensed Matter Physics* 9: 219–236.

M. Koltzscher, C. Neumann, S. Konig and V. Gerke (2003) $Ca^{2+}$-dependent binding and activation of dormant ezrin by dimeric S100P. *Mol. Biol. Cell* 14: 2372-2384.

H. A. Kramers (1940) Brownian motion in a field of force and the diffusion model of chemical reactions. *Physica* 7: 284-304.

O. Kratky and G. Porod (1949) Röntgenuntersuchung gelöster Fadenmoleküle. *Recl. Trav. Chim. Pays-Bas* 68: 1106 –1123.

D. Krüger, B. Anczykowski and H. Fuchs (1997) Physical properties of dynamic force microscopies in contact and noncontact operation. *Annalen der Physik* 509: 341-363.

C. Kruse (2007) Physik in der Zelle. *Physik Journal*: 27.

M. Kumar *et al.* (2007) From the Cover: Highly permeable polymeric membranes based on the incorporation of the functional water channel protein Aquaporin Z. *Proceedings of the National Academy of Sciences* 104: 20719-20724.

G. Lee *et al.* (2006) Nanospring behaviour of ankyrin repeats. *Nature* 440: 246-249.

C. LeGrimellec *et al.* (1998) Imaging of the surface of living cells by low-force contact-mode atomic force microscopy. *Biophys J.* 75: 695-703.

E. Leifson (1951) Staining, shape, and arrangement of bacterial flagella. *J. Bacteriol.* 62: 377-389.

F. Li and D. Leckband (2006) Dynamic strength of molecularly bonded surfaces. *The Journal of Chemical Physics* 125: 194702-9.

L. Li, H. H.-L. Huang, C. L. Badilla and J. M. Fernandez (2005) Mechanical unfolding intermediates observed by single-molecule force spectroscopy in a fibronectin type III module. *Journal of Molecular Biology* 345: 817-826.

A. P. Liu and D. A. Fletcher (2006) Actin polymerization serves as a membrane domain switch in model lipid bilayers. *Biophys. J.* 91: 4064-4070.

X. Liu and G. H. Pollack (2002) Mechanics of F-Actin characterized with microfabricated cantilevers. *Biophys. J.* 83: 2705-2715.

R. Ludwig (2005) Calixarenes for biochemical recognition and separation. *Microchimica Acta* 152: 1-19.

E. Lüthgens (2005) Modellierung der Oberflächenreaktionen von Vesikeln und Proteinen mit Hilfe dynamischer Monte Carlo-Simulationen, PhD thesis

A. Maali *et al.* (2005) Hydrodynamics of oscillating atomic force microscopy cantilevers in viscous fluids. *Journal of Applied Physics* 97: 074907-6.

L. R. MacGillivray and J. L. Atwood (1997) A chiral spherical molecular assembly held together by 60 hydrogen bonds. *Nature* 389: 469-472.

B. Maier, D. Bensimon and V. Croquette (2000) Replication by a single DNA polymerase of a stretched single-stranded DNA. *Proceedings of the National Academy of Sciences* 97: 12002-12007.

P. Mangeat, C. Roy and M. Martin (1999) ERM proteins in cell adhesion and membrane dynamics. *Trends in Cell Biology* 9: 187-192.

M. Manosas, D. Collin and F. Ritort (2006) Force-dependent fragility in RNA hairpins. *Physical Review Letters* 96: 218301-4.

J. F. Marko and E. D. Siggia (1995) Stretching DNA. *Macromolecules* 28: 8759-8770.

P. E. Marszalek *et al.* (1999) Mechanical unfolding intermediates in titin modules. *Nature* 402: 100-103.

P. E. Marszalek, A. F. Oberhauser, Y.-P. Pang and J. M. Fernandez (1998) Polysaccharide elasticity governed by chair-boat transitions of the glucopyranose ring. *Nature* 396: 661-664.

T. Matsui *et al.* (1998) Rho-kinase phosphorylates COOH-terminal threonines of ezrin/radixin/moesin (ERM) proteins and regulates their head-to-tail association. *J. Cell. Biol.* 140: 647-657.

T. Matsui, S. Yonemura and S. Tsukita (1999) Activation of ERM proteins in vivo by Rho involves phosphatidyl-inositol-4-phosphate 5 kinase and not ROCK kinases. *Curre. Biol.* 9: 1259-1262.

S. McLaughlin, J. Wang, A. Gambhir and D. Murray (2002) $PIP_2$ and proteins: interactions, organization, and information flow. *Annu. Rev. Bioph. Biom.* 31: 151-175.

F. M. Menger (2002) Supramolecular chemistry and self-assembly special feature: supramolecular chemistry and self-assembly. *Proceedings of the National Academy of Sciences* 99: 4818-4822.

M. Menke, V. Gerke and C. Steinem (2005) Phosphatidylserine membrane domain clustering induced by annexin A2/S100A10 heterotetramer. *Biochemistry* 44: 15296-15303.

R. Merkel *et al.* (1999) Energy landscapes of receptor-ligand bonds explored with dynamic force spectroscopy. *Nature* 397: 50-53.

M. Mickler *et al.* (2007) Revealing the bifurcation in the unfolding pathways of GFP by using single-molecule experiments and simulations. *Proceedings of the National Academy of Sciences* 104: 20268-20273.

R. A. Milligan, M. Whittaker and D. Safer (1990) Molecular structure of F-actin and location of surface binding sites. *Nature* 348: 217-221.

A. P. Minton (2000) Effects of excluded surface area and adsorbate clustering on surface adsorption of proteins: I. Equilibrium models. *Biophysical Chemistry* 86: 239-247.

A. P. Minton (2001) Effects of excluded surface area and adsorbate clustering on surface adsorption of proteins. *Biophys. J.* 80: 1641-1648.

D. J. Müller and A. Engel (1997) The height of biomolecules measured with the atomic force microscope depends on electrostatic interactions. *Biophysical Journal* 73: 1633-1644.

D. J. Müller *et al.* (1999) Electrostatically balanced subnanometer imaging of biological specimens by atomic force microscope. *Biophysical Journal* 76: 1101-1111.

F. Nakamura *et al.* (1996) Phosphorylation of T-558 of moesin detected by site-specific antibodies in RAW264.7 macrophages. *Biochem. Biophys. Research Comm.* 226: 650-656.

R. R. Netz (2001) Strongly stretched semiflexible extensible polyelectrolytes and DNA. *Macromolecules* 34: 7522-7529.

J.-M. Neuhaus, M. Wanger, T. Keiser and A. Wegner (1983) Treadmilling of actin. *Journal of Muscle Research and Cell Motility* 4: 507-527.

V. Niggli (2005) Regulation of protein activities by phosphoinositide phosphates *Annu Rev Cell Dev Biol.* 21: 57-79.

V. Niggli, C. Andreoli, C. Roy and P. Mangeat (1995) Identification of a phosphatidylinositol-4,5-bisphosphate-binding domain in the N-terminal region of ezrin. *FEBS Letters* 376: 172-176.

H. Noji, R. Yasuda, M. Yoshida and K. Kinosita (1997) Direct observation of the rotation of F1-ATPase. *Nature* 386: 299-302.

Y. Oberdörfer, H. Fuchs and A. Janshoff (2000) Conformational analysis of native fibronectin by means of force spectroscopy. *Langmuir* 16: 9955-9958.

A. F. Oberhauser, P. E. Marszalek, H. P. Erickson and J. M. Fernandez (1998) The molecular elasticity of the extracellular matrix protein tenascin. *Nature* 393: 181-185.

B. Onoa *et al.* (2003) Identifying kinetic barriers to mechanical unfolding of the T. thermophila ribozyme. *Science* 299: 1892-1895.

A. Ott, M. Magnasco, A. Simon and A. Libchaber (1993) Measurement of the persistence length of polymerized actin using fluorescence microscopy. *Physical Review E* 48: R1642-R1645.

J. I. Paredes, A. Martinez-Alonso and J. M. D. Tascon (2000) Adhesion artefacts in atomic force microscopy imaging. *Journal of Microscopy* 200: 109-113.

R. M. Pashley (1981) DLVO and hydration forces between mica surfaces in Li, Na, K and Cs electrolyte solutions: a correlation of double-layer and hydration forces with surface cation exchange properties *J. Colloid Interface Sci.* 83: 531-546.

K. W. Plaxco, C. Spitzfaden, I. D. Campbell and C. M. Dobson (1997) A comparison of the folding kinetics and thermodynamics of two homologous fibronectin type III modules. *Journal of Molecular Biology* 270: 763-770.

G. Podoprygorina, M. Janke, A. Janshoff and V. Böhmer (2008) Self-assembled polymers based on bis-tetra-urea calix[4]arenes connected via the wide rim. *Supramolecular Chemistry* 20: 59-69.

C. Polesello and F. Payre (2004) Small is beautiful: what flies tell us about ERM protein function in development. *Trends in Cell Biology* 14: 294-302.

T. D. Pollard, L. Blanchoin and R. D. Mullins (2000) Molecular mechanisms controlling actin filament dynamics in nonmuscle cells. *Annual Review of Biophysics and Biomolecular Structure* 29: 545-576.

K. E. Prehoda, J. A. Scott, R. D. Mullins and W. A. Lim (2000) Integration of multiple signals through cooperative regulation of the N-WASP-Arp2/3 complex. *Science* 290: 801-806.

B. W. Purse, A. Gissot and J. Rebek (2005) A deep cavitand provides a structured environment for the Menschutkin reaction. *J. Am. Chem. Soc.* 127: 11222-11223.

M. Radmacher *et al.* (1996) Measuring the viscoelastic properties of human platelets with the atomic force microscope. *Biophysical Journal* 70: 556–567.

M. Raible *et al.* (2006) Theoretical analysis of single-molecule force spectroscopy experiments: heterogeneity of chemical bonds. *Biophys. J.* 90: 3851-3864.

M. Raible and P. Reimann (2006) Single-molecule force spectroscopy: Heterogeneity of chemical bonds. *Europhysics Letters*: 628.

D. J. Rainer, F.-O. Alfredo, S. Paul and E. Klaus (2001) Detailed analysis of forces influencing lateral resolution for Q-control and tapping mode. *Applied Physics Letters* 79: 135-137.

T. V. Ratto *et al.* (2006) Nonlinearly additive forces in multivalent ligand binding to a single protein revealed with force spectroscopy. *Langmuir* 22: 1749-1757.

D. Raucher *et al.* (2000) Phosphatidylinositol 4,5 bisphosphated functions as a second messenger that regulates cytoskeleton-plasma membrane adhesion. *Cell* 100: 221-228.

E. Reisler and E. H. Egelman (2007) Actin structure and function: what we still do not understand. *J. Biol. Chem.* 282: 36133-36137.

C. Reynaud *et al.* (2000) Quantitative determination of Young's modulus on a biphase polymer system using atomic force microscopy. *Surface and Interface Analysis* 30: 185-189.

R. P. Richter, R. Berat and A. R. Brisson (2006) Formation of solid-supported lipid bilayers: an integrated view. *Langmuir* 22: 3497-3505.

R. P. Richter and A. R. Brisson (2005) Following the formation of supported lipid bilayers on mica: a Study combining AFM, QCM-D, and Ellipsometry. *Biophysical Journal* 88: 3422-33.

M. Rief *et al.* (1997) Reversible unfolding of individual titin immunoglobulin domains by AFM. *Science* 276: 1109-1112.

M. Rief, F. J.M. and H. E. Gaub (1998) Elastically coupled two-level systems as a model for biopolymer extensibility. *Phys. Rev. Lett.* 81: 4765-4767.

M. Rief, J. Pascual, M. Saraste and H. E. Gaub (1999) Single molecule force spectroscopy of spectrin repeats: low unfolding forces in helix bundles. *Journal of Molecular Biology* 286: 553-561.

T. Rodriguez, R. and R. Garcia (2003) Theory of Q control in atomic force microscopy. *Applied Physics Letters* 82: 4821-4823.

Y. Rudzevich, K. Fischer, M. Schmidt and V. Bohmer (2005) Fourfold tetraurea calix[4]arenes-potential cores for the formation of self-assembled dendrimers. *Organic & Biomolecular Chemistry* 3: 3916-3925.

E. Sackmann (2004) Mikromechanik der Zelle. *Physik Journal* 3: 35-42.

M. Schlierf and M. Rief (2005) Temperature softening of a protein in single-molecule experiments. *J. Mol. Biol.* 354: 497-503.

I. Schwaiger (2005) Kraftspektroskopische Untersuchung einzelner Zytoskelett-Proteine, PhD thesis

I. Schwaiger, C. Sattler, D. R. Hostetter and M. Rief (2002) The myosin coiled-coil is a truly elastic protein structure. *Nature Materials* 1: 232-235.

M. Silverman and M. Simon (1974) Flagellar rotation and the mechanism of bacterial motility. *Nature* 249: 73-74.

P. C. Simons *et al.* (1998) C-terminal threonine phosphorylation activates ERM proteins to link the cell's cortical lipid bilayer to the cytoskeleton. *Biochem. Biophys. Research Comm.* 253: 561-565.

M. L. Simpson (2006) Cell-free synthetic biology: a bottom-up approach to discovery by design. *Mol Syst Biol* 2.

W. J. Smith *et al.* (2003) Structure of the active N-terminal domain of ezrin. Conformational and mobility changes identify keystone interactions. *J. Biol. Chem.* 278: 4949-4956.

P. W. Snyder *et al.* (2007) A stochastic, cantilever approach to the evaluation of solution phase thermodynamic quantities. *Proceedings of the National Academy of Sciences* 104: 2579-2584.

K. Takeuchi *et al.* (1994) Perturbation of cell adhesion and microvilli formation by antisense oligonucleotides to ERM family members. *J. Cell Biol.* 125: 1371-1384.

A. Tamura *et al.* (2005) Achlorhydria by ezrin knockdown: defects in the formation/expansion of apical canaliculi in gastric parietal cells. *J. Cell Biol.* 169: 21-28.

Q. Tang, S.-Q. Shi and L. Zhou (2004) Nanofabrication with atomic force microscopy. *Journal of Nanoscience and Nanotechnology* 4: 948-963.

P. Thallapally, K. , G. Lloyd, O. , J. Atwood, L. and L. Barbour, J. (2005) Diffusion of Water in a Nonporous Hydrophobic Crystal. *Angewandte Chemie International Edition* 44: 3848-3851.

E. Thormann, P. L. Hansen, A. C. Simonsen and O. G. Mouritsen (2006) Dynamic force spectroscopy on soft molecular systems: Improved analysis of unbinding spectra with varying linker compliance. *Colloids and Surfaces B: Biointerfaces* 53: 149-156.

I. Tinoco Jr and C. Bustamante (2002) The effect of force on thermodynamics and kinetics of single molecule reactions. *Biophysical Chemistry* 101-102: 513-533.

L. R. G. Treloar (1975) The physics of rubber elasticity. Oxford University Press, Oxford.

S. Tsukita and S. Yonemura (1999) Cortical actin organization: lessons from ERM (ezrin/radixin/moesin) proteins. *J. Biol. Chem.* 274: 34507-34510.

O. Turunen, T. Wahlstrom and A. Vaheri (1994) Ezrin has a COOH-terminal actin-binding site that is conserved in the ezrin protein family. *J. Cell. Biol.* 126: 1445-1453.

S. J. T. Van Noort *et al.* (1997) Height anomalies in tapping mode atomic force microscopy in air caused by adhesion. *Ultramicroscopy* 69: 117-127.

M. B. Viani *et al.* (1999) Fast imaging and fast force spectroscopy of single biopolymers with a new atomic force microscope designed for small cantilevers. *Review of Scientific Instruments* 70: 4300-4303.

M. S. Vickers and P. D. Beer (2007) Anion templated assembly of mechanically interlocked structures. *ChemInform* 38.

O. I. Vinogradova (1995) Drainage of a thin liquid film confined between hydrophobic surfaces. *Langmuir* 11: 2213-2220.

M. O. Vysotsky, M. Bolte, I. Thondorf and V. Boehmer (2003) New molecular topologies by fourfold metathesis reactions within a hydrogen-bonded calix[4]arene dimer. *Chem. Eur. J.* 9: 3375-3382.

P. Wagner, M. Hegner, H.-J. Guentherodt and G. Semenza (1995) Formation and in situ modification of monolayers chemisorbed on ultraflat template-stripped gold surfaces. *Langmuir* 11: 3867-3875.

J. Wang, A. Arbuzova, G. Hangyas-Mihalyne and S. McLaughlin (2001) The effector domain of myristoylated alanine-rich C kinase substrate binds strongly to phosphatidylinositol 4,5-bisphosphate. *J. Biol. Chem.* 276: 5012-5019.

A. Wegner and J. Engel (1975) Kinetics of the cooperative association of actin to actin filament. *Biophysical Chemistry* 3: 215-225.

J. W. Weisel, H. Shuman and R. I. Litvinov (2003) Protein-protein unbinding induced by force: single-molecule studies. *Current Opinion in Structural Biology* 13: 227-235.

M. A. Welte *et al.* (1998) Developmental regulation of vesicle transport in drosophila embryos: forces and kinetics. *Cell* 92: 547-557.

A. P. Wiita, S. R. K. Ainavarapu, H. H. Huang and J. M. Fernandez (2006) From the Cover: Force-dependent chemical kinetics of disulfide bond reduction observed with single-molecule techniques. *Proceedings of the National Academy of Sciences* 103: 7222-7227.

P. M. Williams *et al.* (2003) Hidden complexity in the mechanical properties of titin. *Nature* 422: 446-449.

G. J. L. Wuite *et al.* (2000) Single-molecule studies of the effect of template tension on T7 DNA polymerase activity. *Nature* 404: 103-106.

T. Yanagida, M. Nakase, K. Nishiyama and F. Oosawa (1984) Direct observation of motion of single F-actin filaments in the presence of myosin. *Nature* 307: 58-60.

R. Zadmard and T. Schrader (2006) DNA recognition with large calixarene dimers. *Angewandte Chemie International Edition* 45: 2703-2706.

A. Zahowski (1993) Phospholipids in animal eukaryotic membranes: transverse asymmetry and movement. *Biochem. J.* 294: 1-14.

L. Zhu, Y. Liu and J. G. Forte (2005) Ezrin oligomers are the membrane-bound dormant form in gastric parietal cells. *Am J Physiol Cell Physiol* 288: C1242-1254.

S. Zou, H. G. Schönherr and J. Vancso (2005) Stretching and rupturing individual supramolecular polymer chains by AFM. *Angewandte Chemie International Edition* 117: 978-981.

# Danksagung

Diese Arbeit entstand überwiegend im Keller des Instituts für Physikalische Chemie der Universität Mainz. Gerade deshalb war die Unterstützung einer Vielzahl von Personen besonders wichtig, die auf ganz unterschiedliche Art und Weise Ihren Beitrag zum Gelingen dieser Arbeit leisteten. Insgesamt hat mir die Zeit bei den „Jansiaten“ sehr viel Spaß gemacht, mich sicherlich in vielerlei Hinsicht geprägt und persönlich weiterentwickelt. Deshalb möchte ich mich bei meinen Mitstreitern, Kooperationspartnern und natürlich meinem „Projekt“-Leiter herzlich bedanken, im Einzelnen bei:

[redacted]

[redacted]

[redacted]

[redacted]

[redacted]

[redacted]

[redacted]

[redacted]

[redacted].

[redacted]

# Veröffentlichungen

M. Janke, Y. Rudzevich, O. Molokanova, T. Metzroth, I. Mey, G. Diezemann, P. Marszalek, J. Gauß, V. Böhmer, A. Janshoff, *Mechanically locked nanocapsules under force enable reversible hydrogen bond breakage.* Science. Manuscript submitted.

M. Janke, A. Herrig, J. Austermann, V. Gerke, C. Steinem, A. Janshoff*, Actin Binding of Ezrin is Activated by Specific Recognition of $PIP_2$- Functionalized Lipid Bilayers.* Biochemistry. Accepted. Published on the web.

G. Podoprygorina, M. Janke, A. Janshoff, V. Böhmer, *Self-Assembled Polymers Based on Bis-Tetra-Urea Calix[4]arenes Connected via the Wide Rim*. Supramolecular Chemistry, 2008, **20** (1-2), 59-69.

H. Müller, M. Janke, R. Zentel, A Janshoff, *Control of $CaCO_3$ Crystallization by Demixing of Monolayers*. Langmuir, 2006*,* **22**, 11034-11040.

A. Herrig, M. Janke, J. Austermann, V. Gerke, A. Janshoff, C. Steinem, *Cooperative Adsorption of Ezrin on $PIP_2$-Containing Membranes*. Biochemistry, 2006*,* **45**, 13025-13034.

[redacted]